Soliton dynamics in the Gross–Pitaevskii equation: splitting, collisions and interferometry

HELM, JOHN,LLOYD

Soliton dynamics in the Gross–Pitaevskii equation: splitting, collisions and interferometry

John Lloyd Helm

Abstract

Bose–Einstein condensates with attractive interactions have stable 1D solutions in the form of bright solitary-waves. These solitary waves behave, in the absence of external potentials, like macroscopic quantum particles. This opens up a wide array of applications for the testing of quantum mechanical behaviours and precision measurement. Here we investigate these applications with particular focus on the interactions of bright solitary-waves with narrow potential barriers.

We first study bright solitons in the Gross–Pitaevskii equation as they are split on Gaussian and δ-function barriers, and then on Gaussian barriers in a low energy system. We present analytic and numerical results determining the general region in which a soliton may not be split on a finite width potential barrier. Furthermore, we test the sensitivity of the system to quantum fluctuations.

We then study fast-moving bright solitons colliding at a narrow Gaussian potential barrier. In the limiting case of a δ-function barrier, we show analytically that the relative norms of the outgoing waves depends sinusoidally on the relative phase of the incoming waves, and determine whether the outgoing waves are bright solitons. We use numerical simulations to show that outside the high velocity limit nonlinear effects introduce a skew to the phase-dependence.

Finally, we use these results to analyse the process of soliton interferometry. We develop analyses of both toroidal and harmonic trapping geometries for Mach–Zehnder interferometry, and then two implementations of a toroidal Sagnac interferometer, also giving the analytical determination of the Sagnac phase in such systems. These results are again verified numerically. In the Mach–Zehnder case, we again probe the systems sensitivity to quantum fluctuations.

Soliton dynamics in the Gross–Pitaevskii equation: splitting, collisions and interferometry

John Lloyd Helm

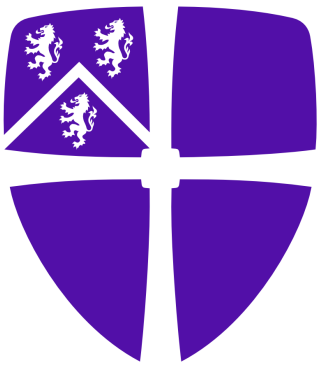

Thesis submitted in accordance with the
requirements for the degree of Doctor of Philosophy

Department of Physics
University of Durham
March 2014

Contents

List of Figures

Declaration

I confirm that no part of the material offered has previously been submitted by myself for a degree in this or any other University. Where material has been generated through joint work, the work of others has been indicated.

John Lloyd Helm
March 2014

Acknowledgements

This thesis is the pinnacle of my education thus far, and the process of its creation has taught me nothing more important than the value of good friends and hard work.

AtMol's Ph.D. class of 2010 have proved very good friends to me indeed, and so I would like to start by thanking them all for proving that success was possible, and failing success there was always cake. I'd thank them all individually if only I had the space. Outside of my immediate cohort I would like to thank David Szwer, Tommy Ogden, Kate Whittaker, Peter Mason and David Holdaway. It is people like these that make AtMol the fantastic environment that it is. I would also like to thank some of the more gregarious members of staff: Matt Jones, Ifan Hughes and Charles Adams, who all gave us much to discuss over coffe.

First among those who helped with the hard work, I thank Tom Billam for patiently teaching me as much as he could. Christoph Weiss picked up where Tom left off, and is an academic whose shrewd judgement served me incredibly well, and so I thank him most sincerely. In making my wild ideas somewhat more grounded, Anna Marchant was an invaluable resource, and so I thank her too.

Above all, Simon Gardiner gave me a fantastic opportunity when he offered me the Ph.D. position in Durham. I could not have hoped for a more approachable, understanding and knowledgeable supervisor, and so he will always have my gratitude. Simon Cornish has also played a large role in my Ph.D. His drive and insight have helped to make the whole process a little more meaningful. My mathematical supervisor, Paul Sutcliffe, provided wise council on a number of occasions, and so I thank him too. I would also like to mention Nick Proukakis, Carlo Barenghi and Anthony Youd of the Newcastle branch, who made me the mathematician I am today.

Outside of Physics; Dan Stow and Georgia Rakusen kept me sane, and I owe them much. Of the Haligonians I'd like to thank Cheryl, Steve, Faye, Lauren and Paul. Also Stu and Charlie, who know what they did.

Finally, I would have been lost entirely without the love and support of my sister, my mother and her partner Stuart, my father, and Jean, who we miss every day.

For my mother, my father and my sister.

Introduction

Key concepts

The Gross-Pitaevskii equation

The work presented in this thesis is, in essence, an attempt to determine the dynamics of a somewhat complicated equation (or small group of similar equations), to which there is no exact solution. This group of equations are variations on the Gross–Pitaevskii equation (GPE) [1], which has the form

$$i\hbar\frac{\partial\psi(\mathbf{r},t)}{\partial t} = \left[-\frac{\hbar^2}{2m}\nabla^2 + U_{\text{ext}}(\mathbf{r}) + gN|\psi(\mathbf{r},t)|^2\right]\psi(\mathbf{r},t). \tag{1}$$

This equation is common in atomic physics, and in this thesis we will primarily discuss it in the context of the Bose–Einstein condensate (BEC) [1–3] but it should be noted that the GPE can arise in a number of different forms, including optical systems with a Kerr type nonlinearity [4, 5]. The creation of the BEC in 1995 [6, 7] brought quantum phenomena to length scales of new orders of magnitude and so the zero temperature, ideal limit of these systems (the GPE) is now a popular area of study.

The fully 3D nature of the GPE, coupled with the presence of external potentials (U_{ext}) means that while it is well understood, the GPE is difficult to solve. This difficulty is primarily a result of the nonlinearity (quantified by the particle number N, and g which is dependent on the inter-particle s-wave scattering scattering length) and so we must resort to non-linear methods of solution in order to continue.

Bright solitary matter-waves

Bright solitary matter-waves are solitonlike dynamical excitations observed in atomic Bose-Einstein condensates (BECs) with attractive inter-atomic interactions [8–11]. They are solitonlike in the sense that they propagate without dispersing [12], emerge largely unscathed from collisions with other bright solitary matter-waves and with external potentials [13, 14], and have center-of-mass trajectories which are well-described by effective particle models [15–17]. They derive these solitonlike properties from their analogousness to the bright soliton solutions of the focusing non-

linear Schrödinger equation (NLSE),

$$iu_t + \frac{u_{xx}}{2} + u\,|u|^2 = 0 \tag{2}$$

to which the mean-field description of an atomic BEC reduces in a homogeneous, quasi-one-dimensional (quasi-1D) limit. These bright soliton solutions of the 1D focusing NLSE have been extensively explored in nonlinear optics, both in the context of solitons in optical fibers [18–22] and as stable structures existing in arrays of coupled waveguides [23, 24] which are described by a discretized NLSE. Although the quasi-1D limit is experimentally challenging for attractive condensates [25], bright solitary matter-wave dynamics remain highly solitonlike outside this limit [10, 14]. Consequently, bright solitary matter-waves present an intriguing candidate system for future interferometric devices [9, 14, 26–30].

Matter-wave interferometry

The macroscopic quantum systems that are bright matter-waves in BECs give us the ability to take advantage of large-scale wave-like phenomena in an atomic medium. A primary mechanism which exploits these concepts is atom interferometry [31–33]. Previously these interferometric systems have been primarily linear, but as more stable BEC experiments become increasingly common and versatile [34] it is becoming clear that there is real scope for the creation of a bright solitary matter-wave interferometer [35].

A key component of such a system is a mechanism to coherently split and recombine bright solitary matter-waves: the collision of a bright solitary wave with a narrow potential barrier is one way to create such a beamsplitter. Within a quasi-1D, mean-field description of an atomic BEC, collisions of single solitary matter-waves with potential barriers and wells have been extensively studied [36–41], and sufficiently fast collisions with potential barriers have been shown to lead to the desired beamsplitting effect [40, 41].

When, in nonlinear optics, the soliton exists in an inhomogeneous array of discrete waveguides, the soliton can be reflected, split or captured at the position of the inhomogeneity [42–44]. This is equivalent, in the continuum limit of an infinite number of waveguides, to splitting a soliton in the GPE at a δ-function [42] — a phenomenon which has been called the “optical axe” [22].

Recently, a number of investigations have considered an interferometer using a nar-

row potential barrier as a beamsplitter for harmonically trapped solitary waves [30, 45], based on the particular configurations of recent experiments [34, 46]. In particular this work demonstrated that such a potential barrier can also be used to recombine solitary waves, by arranging for them to collide at the location of the barrier. In such collisions, the relative norms of the two outgoing solitary waves was shown to be governed by the phase difference Δ between the incoming ones. In the mean-field description the relative norms of the outgoing waves exhibit enhanced sensitivity to small variations in the phase Δ; however, a simulation of the same system including quantum noise, via the truncated Wigner method [47], showed increased number fluctuations that ultimately negated this enhancement [30].

Thesis outline

The thrust of the work presented in this thesis is a comprehensive discussion of how bright solitary matter waves in BECs can be used to perform interferometry. With this goal in mind, the contents are essentially a collation and restructuring of three works produced by the author. These works are

[48] J. L. Helm, T. P. Billam, and S. A. Gardiner, *Bright matter-wave soliton collisions at narrow barriers* Phys. Rev. A **85**, 053621 (2012).

[49] J. L. Helm, S. J. Rooney, Christoph Weiss and S. A. Gardiner, *Splitting bright matter-wave solitons on narrow potential barriers: Quantum to classical transition and applications to interferometry* Phys. Rev. A **89**, 033610 (2014).

[50] J. L. Helm, S. L. Cornish and S. A. Gardiner, *Bright soliton Sagnac interferometry* (in preparation).

Thesis structure

Chapters 1 and 2: Bose-Einstein condensates and Solitons

Chapter 1 provides an introduction to the fundamental concepts of BECs, along with some simple derivations of their more interesting properties. This chapter also points out, as a guide to further study, where some of the more advanced theoretical frameworks describing BECs might be found. The key content of Chapter 1 is the careful derivation of the GPE, and its reduction to the quasi-1D GPE.

Chapter 2 provides information about soliton solutions to the non-linear Schrödinger equation (to which the GPE reduces in the correct limits). We outline some of the more advanced methods of its solution, and use them to provide basic results about the behaviour of these solutions.

Chapters 3 to 5: The components of soliton matter-wave interferometry

Chapter 3 outlines how bright solitary matter-waves can be coherently split by narrow potential barriers. This is a fundamental requirement if we are to consider a soliton interferometer. First comes a comparison between δ-function and Gaussian barriers, in order to compare more physical systems to analytical results. This work determines restrictions on the barrier's width and define how narrow the barrier must be in a given energy regime. The second part of this chapter discusses how we quantify the energetic regime of the system and determine whether or not the soliton may be split as we require in this regime. This question is considered in the context of both the harmonically trapped and untrapped cases. Finally we discuss how the effects of the low energy regime combine with quantum fluctuations of the centre of mass position and momentum and delimit a lower bound on the kinetic energy, below which soliton splitting becomes highly non-classical. This analysis is conducted in the harmonically trapped geometry. This chapter is comprised of results from the first halves of Refs. [48] and [49]

Chapter 4 provides an analysis of soliton collisions at narrow barriers. This is the second requirement of soliton interferometry; that coherent matter-waves be interfered with one another. We present an analytical proof based on a δ-function barrier, and then numerically analyse the system for a Gaussian barrier, determining how the soliton's kinetic energy affects the outcome of the collisional process. This chapter is taken from the second half of Ref. [49]

Chapter 5 outlines two different geometries which may be employed to conduct Mach–Zehnder interferometry. The first is conducted in the absence of axial trapping potentials and follows from established analytical results. The second requires axial harmonic confinement and must be analysed numerically. Finally, we present Monte Carlo simulations of the harmonically trapped system in order to characterise the effect of quantum fluctuations in the low energy regime. The content of this chapter was published in the second half of Ref. [49].

Chapter 1: Bose-Einstein condensates and the Gross-Pitaevskii equation

1.1 The race to absolute zero

1.1.1 Cooling gases in the early 20th Century

The 19th century thermodynamical assertion of absolute zero and the Kelvin scale [51] posed an intriguing question to physicists of the era. What would the removal of thermal disorder reveal about the nature of matter? This began the race to absolute zero. Labs across Europe were set up with the goal of liquefying all known gasses. Aided by the development of new cooling techniques, oxygen was liquefied at 90K, nitrogen at 77K, and hydrogen at 20K. This last was achieved by James Dewar in London around 1896. The final challenge to Dewar and his Leiden based rival Kamerlingh Onnes was the liquefaction of helium, which had only recently been identified as an element.

It was not until 1908 that this was achieved by Kamerlingh Onnes, with the condensation of liquid helium occurring at 4K. For this work he was awarded the Nobel Prize in 1913. After this new low in the race to zero, in 1924 Kamerlingh Onnes also observed that helium appeared to undergo a second phase transition at 2.2K, at which point was a discontinuous peak in the density (the λ point). While interesting, this behaviour was secondary to frictionless flow observed by Kapitza [52] (who was awarded a Nobel prize) and by Allen and Misener [53] (who, controversially, were not) in 1938. This superfluid flow allowed the helium to, among other things, climb out of open containers, pass through microscopic holes and flow against the gradient of entropy through a superleak. This concept of superfluidity, and the concepts of superconductivity developed by Kamerlingh Onnes in 1911, were beyond the understanding of the classical theories of the time, being fundamentally quantum mechanical in nature.

The next development in the understanding of the low temperature world would rely on the work of an Indian mathematical physicist, Satyendra Nath Bose. Bose's original work [54] considered the particle statistics associated with indistinguishable, non-interacting particles in the form of photons. Considering the implications

of Bose's analysis in the context of non-interacting massive particles with integer-spin (as would be required for bosonic interchangeability by Pauli [55]), Einstein posited a process whereby at low energy the particles would macroscopically occupy a single, lowest-energy state of the system [2, 3]. This was the inception of the BEC and would be linked with superfluid helium shortly after Kapitza, Allen and Misener's experiments [52, 53] by London [56] and Tizsa [57].

1.1.2 Experimental realisations of the BEC

Just as the Dewar and other experimental methods developed in the late 19th century facilitated the liquefaction of all known gasses, developments in laser cooling in the late 20th century [58] would allow the next leg on the race to absolute zero, and the understanding of matter at such degrees of thermal order, to begin.

The first atomic BEC was finally realised in 1995. Wieman and Cornell condensed ^{87}Rb [7], while Ketterle was able to condense ^{23}Na [6]. These achievements were awarded Nobel prizes in 2001. As in the late 19th century there was a flurry of activity, now focused on the condensation of any stable isotope which lends itself to the methods of laser cooling. This so far includes [59]: isotopes of other alkali metals — ^{7}Li [60], ^{39}K [61], ^{41}K [62], ^{85}Rb [63], ^{133}Cs [64] — various other elemental isotopes — ^{1}H [65], ^{40}Ca [66], ^{84}Sr [67, 68], ^{86}Sr [69], ^{88}Sr [70], ^{168}Er [71] — four different isotopes of Ytterbium (two of which were condensed together) — ^{170}Yb [72], ^{176}Yb [73], ^{174}Yb and ^{168}Yb [74] — a metastable (lowest triplet) state of Helium — ^{4}He [75, 76] — and two elements which displayed long-range dipolar interactions —^{164}Dy [77], ^{52}Cr [78].

These condensates could all be classified in terms of the strength of their interactions. As such, a key feature of current investigations into BECs is the Feshbach Resonance. These resonances are a feature of the internal structure of dimeric molecules, and allow the interactions of the condensed atoms to be tuned to some desirable state through the application of external magnetic fields [79, 80]. This allows the s-wave scattering length a_s to take a continuous and wide range of values, both positive and negative, allowing for the creation of strongly or weakly attractive or repulsive condensates. This is extremely useful in that, among other things, it allows experimentalists to avoid excessive density, satisfying the dilution criterion $n^{1/3}a_s \ll 1$. For instance, condensates of alkali metals typically contain $10^3 - 10^7$ atoms, and have number densities in the $10^{11} - 10^{15}\text{cm}^{-3}$. This dilution both prevents three body loss events, which would deplete the condensate, and allows for a

contact potential approximation of the interactions, which will be invaluable in the development of the theoretical framework for the dynamics of the BEC [81, 82].

It is interesting that this requirement of a dilute, weakly interacting gas precludes the quantitative description of helium II as a true BEC. While superfluidity is a fundamental characteristic of the BEC the first observed instance of such superfluidity was in a system with such strong interactions that the condensed fraction is only of the order of 10% [83, 84]. The standard model used to fully describe superfluid helium is the two-fluid model, where one fluid is inviscid and the other viscous.

1.2 Degenerate Bose gases

1.2.1 Bose–Einstein statistics

We will now outline some of the characteristics of condensates in dilute atomic vapours. In this section we will outline the derivation of the Bose–Einstein distribution, following the formalism outlined in Ref. [85]. Further details are available in other standard textbooks on quantum mechanics and Bose–Einstein condensates [81, 86]. We first consider the properties of a statistical ensemble describing a gas in thermodynamic equilibrium [87]. The system is comprised of discrete single-particle states with energy E_n, degeneracy d_n and occupation N_n. We now work under the assumption that each degenerate state within a given energy level can be occupied an arbitrary number of times by indistinguishable particles; a degenerate Bose gas. As such, the number of possible configurations in a given energy level is

$$Q_n = \frac{(N_n + d_n - 1)!}{N_n!(d_n - 1!)}; \tag{1.1}$$

and the total number of ways the entire system may be configured (Q) is the product of the configurations of all energies

$$Q(N_1, N_2, N_3, \ldots) = \prod_{n=1}^{\infty} Q_n. \tag{1.2}$$

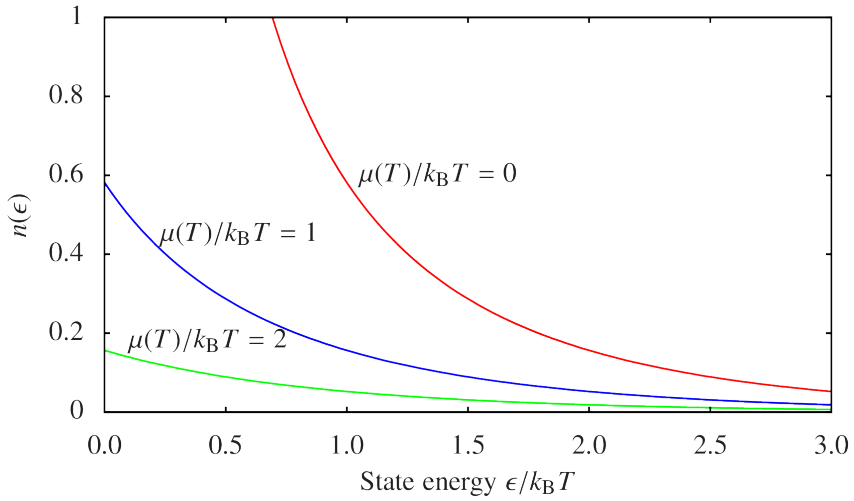

Figure 1.1: State occupation for varying temperatures

We can write the total particle number and energy as

$$N = \sum_{n=1}^{\infty} N_n, \tag{1.3}$$

$$E = \sum_{n=1}^{\infty} E_n N_n, \tag{1.4}$$

and maximise Q under these measures by using the method of Lagrange multipliers α and β in the new function G, defined as

$$G = \ln(Q) + \alpha \left[N - \sum_{n=1}^{\infty} N_n \right] + \beta \left[E - \sum_{n=1}^{\infty} N_n E_n \right]. \tag{1.5}$$

Here we have taken the logarithm of Q to simplify our arithmetic by turning the product into a sum. Setting $\partial G / \partial N_n = 0$ will maximise Q and so tell us that the most likely occupation configuration for a given total energy and particle number is

$$N_n = \frac{d_n}{e^{\alpha + \beta E_n} - 1}, \tag{1.6}$$

where we have taken $d_n \gg 1$.

In order to further explore the dynamics of the degenerate Bose gas and determine α, β we will consider a more carefully defined system.

1.2.2 Bose condensation for an ideal gas

We assume an ideal gas of an infinite number of particles in an infinite volume but keep the density N/V constant. As such the particles can take a continuous range of energies $\epsilon(k) = k^2\hbar^2/2m$, where k is the length of the particle's wave-vector $\boldsymbol{k}$ and so $\hbar k$ is its scalar momentum.

Our Lagrange multipliers α and β can be set to $-\mu(T)/k_{\mathrm{B}}T$ and $1/k_{\mathrm{B}}T$ respectively, defining T as the temperature and $\mu(T)$ as the so-called chemical potential of our (now grand canonical) ensemble. k_{B}, of course, is Boltzmann's constant. This yields the Bose–Einstein distribution:

$$n(\epsilon) = \frac{1}{e^{(\epsilon-\mu(T))/k_{\mathrm{B}}T} - 1}, \tag{1.7}$$

which quantifies the number of particles n in a state with energy ϵ. Note that this quantity differs from the number of particles with energy ϵ by a factor of the degeneracy of that energy.

Furthermore, we can now re-write our particle number and energy conditions [Eqs. (1.3) and (1.4)] in the ideal gas limit using Eq. (1.7). This is achieved by reformulating the degeneracy as the integral element over a thin spherical shell in k-space, such that $d_n \to (V/2\pi^2)k^2dk$, and rewriting our summations as integrals:

$$N = \frac{V}{2\pi^2}\int_0^\infty \frac{k^2}{e^{[(\hbar^2k^2/2m)-\mu]/k_{\mathrm{B}}T} - 1}dk \tag{1.8}$$

$$E = \frac{V}{2\pi^2}\frac{\hbar^2}{2m}\int_0^\infty \frac{k^4}{e^{[(\hbar^2k^2/2m)-\mu]/k_{\mathrm{B}}T} - 1}dk \tag{1.9}$$

By noting that $n(\epsilon)$ must be non-negative, we see from Eq. (1.7) that $\mu(T) < \epsilon_{\mathrm{min}}$, and so the chemical potential must be negative. Combining this requirement with Eq. (1.8) we see that that $\mu(T)$ increases monotonically with T. As such, a pivotal event occurs at some critical value T_λ, where $\mu(T_\lambda) = 0$. Studying Fig. 1.1 we see that, at $T = T_\lambda$ the population of the $\epsilon = 0$ energy level diverges, which we interpret as a condensation of the gas in the zero momentum state.

1.2.3 Long range off-diagonal order

Bose–Einstein condensates constitute a macroscopic quantum body supporting coherent interaction over the length of the condensate [88], long distances indeed in quantum mechanical terms. This quality is of fundamental interest to modern

physics as it allows us to bring quantum behaviour to large scales [27, 28, 89–92], further confirming the postulates of quantum mechanics and opening up new avenues for applying these ideas in fields like metrology [93–95]. The exploration and exploitation of this behaviour is a continuation of the early 20th century desire to strip thermal complications from a system to illuminate the low energy world.

Here, we will illustrate this large distance correlation utilising the concept of off-diagonal long-range order, closely following the description outlined in Ref [86]. We will first introduce the one-body density matrix which has elements defined as

$$\rho_1(\mathbf{r}, \mathbf{r}', t) = \langle \hat{\Psi}^\dagger(\mathbf{r}')\hat{\Psi}(\mathbf{r})\rangle. \tag{1.10}$$

Here, the $\langle \cdots \rangle$ notation implies a quantum and, in the case of finite temperature, thermal average with respect to the full many-particle density matrix. Taking $\hat{\Psi}^\dagger(\mathbf{r})$ as the field operator which creates a particle at point $\mathbf{r}$ [96] [along with the annihilation operator $\hat{\Psi}(\mathbf{r})$], we see that $\rho_1(\mathbf{r}, \mathbf{r}', t)$ is the probability of removing a particle at $\mathbf{r}$ and regaining it at $\mathbf{r}'$ at time t. For the moment we will not consider time dependence of the density matrix, remaining in our equilibrated ideal gas scenario. As we consider bosons, we assert that our field operators follow the bosonic commutator relations:

$$[\hat{\Psi}(\mathbf{r}), \hat{\Psi}^\dagger(\mathbf{r}')] = \delta(\mathbf{r} - \mathbf{r}'), \qquad [\hat{\Psi}(\mathbf{r}), \hat{\Psi}(\mathbf{r}')] = [\hat{\Psi}^\dagger(\mathbf{r}), \hat{\Psi}^\dagger(\mathbf{r}')] = 0. \tag{1.11}$$

Similarly, we can denote the momentum analogue of ρ_1 as,

$$\rho_1(\mathbf{p}, \mathbf{p}', t) = \langle \hat{\Psi}^\dagger(\mathbf{p}')\hat{\Psi}(\mathbf{p})\rangle, \tag{1.12}$$

where the field operators are now taken to be in momentum space, and so

$$\hat{\Psi}(\mathbf{p}) = \frac{1}{(2\pi\hbar)^{3/2}} \int d\mathbf{r}\hat{\Psi}(\mathbf{r})e^{i\mathbf{p}\cdot\mathbf{r}/\hbar} \tag{1.13}$$

As usual, setting $\mathbf{r}' = \mathbf{r}$ and $\mathbf{p}' = \mathbf{p}$ yields the diagonal spatial density $\rho(\mathbf{r}, t) = \rho_1(\mathbf{r}, \mathbf{r}, t)$ and diagonal momentum density $\rho(\mathbf{p}, t) = \rho_1(\mathbf{p}, \mathbf{p}, t)$. Both of these are normalised by $\int d\mathbf{r}\rho(\mathbf{r}, t) = \int d\mathbf{p}\rho(\mathbf{p}, t) = N$

Substituting Eq. (1.13) into Eq. (1.12) and adopting the relative coordinate system

defined as $\mathbf{s} = \mathbf{r} - \mathbf{r}'$, $\mathbf{R} = (\mathbf{r} + \mathbf{r}')/2$ we obtain

$$\rho(\mathbf{p}, t) = \frac{1}{(2\pi\hbar)^3} \int d\mathbf{R} d\mathbf{s} \rho_1 \left(\mathbf{R} - \frac{\mathbf{s}}{2}, \mathbf{R} + \frac{\mathbf{s}}{2}, t \right) e^{i\mathbf{p}\cdot\mathbf{s}/\hbar}. \tag{1.14}$$

In this analysis, we still consider the ideal Bose condensed gas as described above, where the volume is infinite, but N/V is held constant at n. In this case, we see that our density matrix no longer depends on the relative coordinate $\mathbf{R}$ and is rotationally symmetric, and so we can write $\rho_1(\mathbf{r}, \mathbf{r}', t) = \rho_1(s, t)$[1], where $s = |\mathbf{r} - \mathbf{r}'|$. This quantity is equal to the inverse 3D Fourier transform over volume V of $\rho(\mathbf{p}, t)$,

$$\rho_1(s, t) = \frac{1}{V} \int d\mathbf{p} \rho(\mathbf{p}, t) e^{-i\mathbf{p}\cdot\mathbf{s}/\hbar}. \tag{1.15}$$

When the temperature drops below T_λ our atoms macroscopically occupy the zero momentum state, and so we can partition our density operator as $\rho(\mathbf{p}, t) = N_c \delta(\mathbf{p}) + \tilde{\rho}(\mathbf{p}, t)$. Here N_c is the condensation population, with $N_c/N \leq 1$, and tells us the proportion of our atoms in the zero momentum state. Substituting this form of $\rho(\mathbf{p}, t)$ into Eq. (1.15), we see that

$$\lim_{s \to \infty} \rho_1(s, t) = N_c/V, \tag{1.16}$$

If we consider this result in the context of our previous interpretation of the density matrix, we see that we are stating that there is a non-zero probability of a particle being removed and another particle being added coherently over long distances, and that this probability remains constant outside of a certain range. This off-diagonal long-range order demonstrates that the BEC supports long-range coherent interactions independent of direct particle interactions in the form of nonlinear potentials.

1.2.4 The macroscopically occupied mode

Previously we relied on the ideal homogeneous gas case to illuminate the characteristics of the BEC. However, this is not the only system which supports BEC. Often the system of the harmonically trapped weakly interacting gas is developed by analogy to the ideal gas case. This development can introduce some inconsistencies, for instance in the determination of T_λ [97–100] and the loss of a true thermodynamic

[1] It should be noted that $\rho(\mathbf{r}, t)$ denotes the diagonal matrix elements only and is a function of only one position, while $\rho_1(s, t)$ describes groups of off-diagonal elements and can still be considered to be a function of two positions, the notations of which are condensed for brevity, and so is a general matrix element of the one body density matrix, given certain assumptions about the symmetry of the state.

phase transition in favour of a smoothed pseudo-transition [97, 101–103]. However, similar analyses to that presented in Section 1.2.2 do still show the Bose condensation event when the temperature drops below a critical value and a particular state becomes macroscopically occupied, even in the presence of weak interactions and/or harmonic trapping.

Here, we will generalise our definition of the condensate and formally introduce the definition adopted by Penrose and Onsager [84]. This definition does not rely on a zero momentum state (available to the untrapped ideal gas but not elsewhere), merely a single macroscopically occupied state. We begin with the density operator $\rho_1(\mathbf{r}, \mathbf{r}', t)$ as defined in Eq. (1.15). Previously we did not have a fixed particle number, but now we move from the grand canonical description to the canonical formulation (we still assume thermal equilibrium at temperature T), where the particle number is assumed to be well defined and so the density matrix is normalised by

$$\int d\mathbf{r}\rho_1(\mathbf{r}, \mathbf{r}, t) = N. \tag{1.17}$$

In this treatment we adopt the modes ϕ_i form an orthonormal basis of single particle wave functions. These functions are eigenstates of the Hermitian one-body density operator, with matrix element defined by Eq. (1.15) and so can be obtained through diagonalisation at any time t [86].

$$\int d\mathbf{r}'\rho_1(\mathbf{r}, \mathbf{r}', t)\phi_i(\mathbf{r}', t) = n_i(t)\phi_i(\mathbf{r}, t), \tag{1.18}$$

with $\sum_i n_i(t) = N$. We identify a condensate where an eigenstate $\phi_c(\mathbf{r}, t)$ has eigenvalue $N_c(t)$ which is of the order of N and so is much larger than all other eigenvalues (which are generally of order 1).

1.3 Dynamics of the BEC and the GPE

Overview

In this section we will outline a derivation of how one can determine the dynamics of the entire system, and particularly the dynamics of the condensate. The original results of this thesis pertain only to the condensed state in the absence of thermal effects, but it is helpful to discuss the different ways that the fundamental equation describing this state, the Gross–Pitaevskii equation (GPE), can be derived, and briefly describe the implications and results associated with the different derivations. In

brief, The GPE constitutes a lowest order description of the system dynamics, but this description is consistent throughout the various approaches, accounting for its robustness as a method to describe dynamics of BECs up to $T \approx T_\lambda/2$.

1.3.1 Second quantised Hamiltonian

Our Hamiltonian can be constructed from single-particle contributions and two-particle contributions [82, 96]. This relies on the assumption that the gas is sufficiently dilute that three-body collisions are unlikely, as discussed previously. The single-particle contributions will account for potential and kinetic energy. The two-particle contributions denote collisional events via some interaction potential. As such, we can write

$$\hat{H} = \sum_{i=1}^{N} \hat{h}_1(\mathbf{r}_i) + \frac{1}{2}\sum_{i,j=1}^{N} \hat{V}(\mathbf{r}_i, \mathbf{r}_j), \tag{1.19}$$

where $\hat{h}_1(\mathbf{r})$ is the single particle Hamiltonian and $\hat{V}(\mathbf{r}, \mathbf{r}')$ describes the two-body interactions. Note that the factor of one half prevents double counting and that the interaction potential operator $\hat{V}$ is defined to be zero for $i = j$. Moving from the standard position basis used here, we can consider the state occupation operators $\hat{a}_i, \hat{a}_i^\dagger$ which remove and add particles (respectively) in some basis mode $\phi_i(\mathbf{r}, t)$ of the system. We again assert the bosonic commutator relations for these operators

$$[\hat{a}_i^\dagger, \hat{a}_j] = \delta_{i,j}, \qquad [\hat{a}_i, \hat{a}_j] = [\hat{a}_i^\dagger, \hat{a}_j^\dagger] = 0 \tag{1.20}$$

We can now consider a single-particle Hamiltonian contribution as the event that a particle spontaneously moves from state l to mode m, and the two-particle contributions being those events where two particles move from states l, j to states m, k (remembering to symmetrise along the way to account for the interchangeable nature of the bosons). As such, we rewrite Eq. (1.19) as

$$\hat{H} = \sum_{\ell m} \langle \ell | \hat{h}_1(\mathbf{r}) | m \rangle \hat{a}_\ell^\dagger \hat{a}_m + \frac{1}{2}\sum_{\ell jmk} \langle \ell j | \hat{W} | mk \rangle \hat{a}_\ell^\dagger \hat{a}_j^\dagger \hat{a}_m \hat{a}_k. \tag{1.21}$$

The single-particle events are all weighted by the matrix elements

$$\langle \ell | \hat{h}_1(\mathbf{r}) | m \rangle = \int d\mathbf{r} \phi_\ell^*(\mathbf{r}, t) \hat{h}_1(\mathbf{r}) \phi_m(\mathbf{r}, t), \tag{1.22}$$

and the two-particle events are weighted by the symmetrised matrix elements

$$\langle \ell j | \hat{W} | mk \rangle = \frac{1}{2}\left(\langle \ell j | \hat{V} | mk \rangle + \langle \ell j | \hat{V} | km \rangle \right), \tag{1.23}$$

where

$$\langle \ell j | \hat{V} | mk \rangle = \iint d\mathbf{r} d\mathbf{r}' \phi_\ell^*(\mathbf{r}, t) \phi_j^*(\mathbf{r}', t) \hat{V}(\mathbf{r} - \mathbf{r}') \phi_m(\mathbf{r}, t) \phi_k(\mathbf{r}', t). \tag{1.24}$$

The single particle eigenstates ϕ_i which construct our field operators have eigenvalues as defined in Eq. (1.18). We can now construct our field operators $\hat{\Psi}, \hat{\Psi}^\dagger$ in terms of $\hat{a}, \hat{a}^\dagger$, such that

$$\begin{aligned} \hat{\Psi}(\mathbf{r}) &= \sum_i \hat{a}_i(t) \phi_i(\mathbf{r}, t), \\ \hat{\Psi}^\dagger(\mathbf{r}) &= \sum_i \hat{a}_i^\dagger(t) \phi_i^*(\mathbf{r}, t). \end{aligned} \tag{1.25}$$

This allows us to transform our Hamiltonian [Eq. (1.21)], yielding the second quantised system Hamiltonian

$$\begin{aligned} \hat{H} = &\int d\mathbf{r} \hat{\Psi}^\dagger(\mathbf{r}) \hat{h}_1(\mathbf{r}) \hat{\Psi}(\mathbf{r}) \\ &+ \frac{1}{2} \iint d\mathbf{r} d\mathbf{r}' \hat{\Psi}^\dagger(\mathbf{r}') \hat{\Psi}^\dagger(\mathbf{r}) \hat{V}(\mathbf{r} - \mathbf{r}') \hat{\Psi}(\mathbf{r}') \hat{\Psi}(\mathbf{r}). \end{aligned} \tag{1.26}$$

Finally, we set the forms of our single- and two-particle operators. The single-particle operator is simply the sum of kinetic and potential energies, $-\hbar^2 \nabla^2 / 2m + U_{\text{ext}}(\mathbf{r})$. The two-particle interactions are approximated by a contact potential $g\delta(\mathbf{r} - \mathbf{r}')$. The interaction strength is given by $g = 4\pi\hbar^2 a_s / m$, where a_s is the s-wave scattering length. Finally, we obtain

$$\hat{H} = \int d\mathbf{r} \hat{\Psi}^\dagger(\mathbf{r}) \left[-\frac{\hbar^2}{2m} \nabla^2 + U_{\text{ext}}(\mathbf{r}) + \frac{g}{2} \hat{\Psi}^\dagger(\mathbf{r}) \hat{\Psi}(\mathbf{r}) \right] \hat{\Psi}(\mathbf{r}). \tag{1.27}$$

Working in the Heisenberg picture [96], we can obtain the time evolution of an arbitrary operator $\hat{O}$ via the standard relation

$$i\hbar \frac{d\hat{O}}{dt} = [\hat{O}, \hat{H}] + i\hbar \frac{\partial \hat{O}}{\partial t}. \tag{1.28}$$

1.3.2 Spontaneous symmetry-breaking

Symmetry breaking partition

Having picked out the condensate mode ϕ_c and defined the mode operators $\hat{a}_i(t)$ (in particular, the condensate mode operator $\hat{a}_c(t)$ which acts on the condensate mode

$\phi_c(\mathbf{r},t)$) we can decompose and partition our field operators [104], giving

$$\hat{\Psi}(\mathbf{r}) = \phi_c(\mathbf{r},t)\hat{a}_c(t) + \hat{\delta}_{\rm n}(\mathbf{r},t). \tag{1.29}$$

The more convenient $\hat{\delta}_{\rm n}$ notation refers to the non-condensate field operator and will be explicitly defined later. The standard procedure from this point on [81, 82, 86, 105–107] is to make use of the large N_c limit, where $\langle \hat{a}_c^\dagger \hat{a}_c \rangle \gg [\hat{a}_c^\dagger, \hat{a}_c]$, and so approximate the condensate field operator term $\phi_c(\mathbf{r},t)\hat{a}_c(t)$ by the classical field $\psi_c(\mathbf{r},t) = \langle \hat{\Psi}(\mathbf{r}) \rangle$. This approximation introduces $\hat{\delta}_{\rm s}(\mathbf{r},t)$ as a fluctuation term about the finite expectation value of $\hat{\Psi}(\mathbf{r},t)$, specifically

$$\hat{\Psi}(\mathbf{r}) = \psi_c(\mathbf{r},t) + \hat{\delta}_{\rm s}(\mathbf{r},t). \tag{1.30}$$

Hamiltonian contributions

We note that $\langle \hat{\delta}_{\rm s}(\mathbf{r},t) \rangle = 0$ because $\hat{\delta}_{\rm s}(\mathbf{r},t)$ is a well defined fluctuation operator, and also note that $\hat{\delta}_{\rm s}(\mathbf{r},t)$ scales with the number of non-condensed or thermal atoms $N_t(t)$. This means that we can use this fluctuation operator not only to determine the coupled dynamics of the condensed and non-condensed atoms [via Eq. (1.28)] but also as a small expansion parameter allowing for varying degrees of exactitude in our analysis. In particular, we can substitute Eq. (1.30) into a slightly modified version of our Hamiltonian [Eq. (1.27)]. This yields

$$\hat{H}' = H_0^{\rm sb} + \hat{H}_{\rm h}^{\rm sb}, \tag{1.31}$$

The prime denotes the modification of Eq. (1.27) to obtain the grand canonical Hamiltonian [108] of the system (which is consistent with the lack of number-conservation which will be discussed later [82]), such that $\hat{H}' = \hat{H} - \mu\hat{N}$ for chemical potential μ and number operator $\hat{N} = \int d\mathbf{r} \hat{\Psi}^\dagger \hat{\Psi}$. The non-operator term $H_0^{\rm sb}$ denotes those terms which are zeroth order in terms of $\hat{\delta}_{\rm s}$ and has the form

$$H_0^{\rm sb} = \int d\mathbf{r} \left[\psi_c(\mathbf{r},t)^* \left(\hat{h}_1(\mathbf{r}) - \mu \right) \psi_c(\mathbf{r},t) + \frac{g}{2} |\psi_c(\mathbf{r},t)|^4 \right]. \tag{1.32}$$

Because this term is purely classical, we can easily obtain the equation which describes the evolution of $\psi_c(\mathbf{r},t)$ through functional differentiation, which would yield the GPE [109, 110]. Terms which are first degree or higher in $\hat{\delta}_{\rm s}$ are contained in $\hat{H}_{\rm h}^{\rm sb}$. While these terms are not directly relevant to the work presented in this thesis, it is worthwhile to point out what they can be used to achieve.

Zero temperature

Firstly, the terms up to second order can be used to determine equations for the collective modes around the ground state; the modes of the Bogoliubov quasiparticles [110–113]. These modes can, in fact, be derived from linearising a time dependent perturbation applied to $\psi_c(\mathbf{r}, t)$ in the zeroth order approximation [82]. It can be shown that these quasiparticles follow a bosonic algebra, and so, to second order, the problem can be reduced to considering a system of non-interacting bosonic quasiparticles [82].

Finite temperature, static

Secondly, the higher order terms can be used to develop static thermal cloud descriptions in the finite temperature limit. This requires a mean-field approximation of third and fourth order occurrences of $\hat{\delta}_s$ via Wick's theorem [96, 114] equivalent to ignoring particle-exchanging collisions between condensed and thermal atoms (third order) and ignoring thermal particle-exchanging collisions (fourth order). This essentially decouples the system and so describes static dynamics. Furthermore, the full treatment of all these terms after the mean-field approximations [the Hartree-Fock-Bogoliubov (HFB) limit] has the advantage of dressing the single-particle states as Bogoliubov quasiparticles [115], but is susceptible to issues arising from the contact potential approximation [116] (known as ultraviolet divergence) and contains an anomalous gap in the quasiparticle excitation spectrum [117, 118]. A further mean-field approximation is available wherein terms with double creation or annihilation operators are discarded, equivalent to describing the system with single particle energies only [82].

Finite temperature, dynamic

Finally, we consider the evolution of the coupled condensate and non-condensate. This is achieved using the Heisenberg equation of motion [Eq. (1.28)] with Eq. (1.30) to determine the coupled dynamics equations of the condensate mode and then the fluctuation operator $\hat{\delta}_s$ [119, 120]. Noting that $\psi_c(\mathbf{r}, t) = \langle\hat{\Psi}(\mathbf{r})\rangle$ (by definition), $\langle\partial(\hat{\delta}_s)/\partial t\rangle = 0$ (because the statistical average commutes with the time derivative and $\hat{\delta}_s$ is a well defined fluctuation operator with zero mean) and that

$\hat{\Psi}(\mathbf{r})$ has no explicit t dependence the condensate equation becomes

$$\begin{aligned} i\hbar\frac{d\psi_c(\mathbf{r},t)}{dt} &= \langle[\hat{\Psi},\hat{H}]\rangle \\ &= \langle\hat{h}_1(\mathbf{r})\hat{\Psi}\rangle + g\langle\hat{\Psi}^\dagger\hat{\Psi}\hat{\Psi}\rangle \\ &= \left[\hat{h}_1(\mathbf{r}) + g|\psi_c|^2\right]\psi_c + 2g\langle\hat{\delta}_s^\dagger\hat{\delta}_s\rangle\psi_c + g\langle\hat{\delta}_s\hat{\delta}_s\rangle\psi_c^* + g\langle\hat{\delta}_s^\dagger\hat{\delta}_s\hat{\delta}_s\rangle. \end{aligned} \tag{1.33}$$

Similarly, the evolution of the non-condensate operator is given by

$$i\hbar\frac{d\hat{\delta}_s(\mathbf{r},t)}{dt} = i\hbar\frac{d}{dt}\left[\hat{\Psi}(\mathbf{r}) - \psi_c(\mathbf{r},t)\right],$$

which can be written [121], with functional dependences omitted for brevity, as

$$\begin{aligned} i\hbar\frac{d\hat{\delta}_s}{dt} = \hat{h}_1(\mathbf{r})\hat{\delta}_s + g\left[2|\psi_c|^2\hat{\delta}_s + \psi_c^2\hat{\delta}_s^\dagger\right] + 2g\left(\hat{\delta}_s^\dagger\hat{\delta}_s - \langle\hat{\delta}_s^\dagger\hat{\delta}_s\rangle\right)\psi_c \\ + g\left(\hat{\delta}_s\hat{\delta}_s - \langle\hat{\delta}_s\hat{\delta}_s\rangle\right)\psi_c^* + g\left(\hat{\delta}_s^\dagger\hat{\delta}_s\hat{\delta}_s - \langle\hat{\delta}_s^\dagger\hat{\delta}_s\hat{\delta}_s\rangle\right). \end{aligned} \tag{1.34}$$

These equations are exact, but lead to an infinite hierarchy of coupled equations of motion, and so some truncation is required if they are to be solved. Various approximations and methods are available to this end, including the above mentioned HF [114] and HFB [122–124] mean field approximations. Full discussions of the available methodologies are beyond the scope of this thesis, but in depth discussions are available in the standard texts [81, 86, 107].

Problems with symmetry-breaking

There are two major problems with the symmetry-breaking approach. First, the classical field approximation requires replacing $\hat{a}_c(t)$ with $\sqrt{N_c(t)}e^{i\Phi}$ (which is a complex number), for some arbitrary phase Φ. This replacement is often referred to as the Bogoliubov approximation [125]. This assumes $\sqrt{N_c(t)}e^{i\Phi}\phi_c(\mathbf{r},t)$ to be a coherent state and fixes the phase of the condensate mode, breaking the $U(1)$ gauge symmetry of the Hamiltonian and leading to uncertainty in the particle number [106]. As such, this method is named the *symmetry-breaking* approach.

A second problem is the lack of orthogonality between the non-condensate fluctuations $\hat{\delta}_s(\mathbf{r},t)$ and the condensate mode $\phi_c(\mathbf{r},t)$. This is something of a problem when considering coupled condensate non-condensate dynamical treatments. We can see this lack of orthogonality by taking the expectation value of Eq. (1.29),

$$\langle\hat{\Psi}\rangle = \langle\hat{a}_c(t)\rangle\phi_c(\mathbf{r},t) + \langle\hat{\delta}_n(\mathbf{r},t)\rangle, \tag{1.35}$$

substituting into Eq. (1.30) and then equating to Eq. (1.29). This gives

$$\hat{\delta}_{\rm s} = [\hat{a}_c(t) - \langle \hat{a}_c(t)\rangle]\,\phi_c(\mathbf{r},t) + \left[\hat{\delta}_{\rm n}(\mathbf{r},t) - \langle \hat{\delta}_{\rm n}(\mathbf{r},t)\rangle\right]. \tag{1.36}$$

1.3.3 Number-conserving formalism

Overview

The issues associated with symmetry-breaking can be avoided by taking a different approach. The number-conserving formalism developed by C. Gardiner [126], Castin and Dum [127, 128], Morgan [117, 117, 129–132], and S. Gardiner [129] are more consistent with the Penrose-Onsager definition of the BEC [84] in that they maintain the orthogonality of the condensate and non-condensate. This yields a canonical description of the system, as apposed to the grand-canonical interpretation imposed by the lack of number conservation inherent in the symmetry-breaking.

The partition

Instead of immediately approximating the condensate mode by a classical field, we retain the condensate operators

$$\hat{a}_c(t) = \int d\mathbf{r}\phi_c^*(\mathbf{r},t)\hat{\Psi}(\mathbf{r}), \tag{1.37}$$

and define the non-condensate field operator $\hat{\delta}_{\rm n}(\mathbf{r},t)$ [Eq. (1.29)] as

$$\hat{\delta}_{\rm n}(\mathbf{r},t) = \int d\mathbf{r}' Q(\mathbf{r},\mathbf{r}',t)\hat{\Psi}(\mathbf{r}'), \tag{1.38}$$

where the projector is defined as $Q(\mathbf{r},\mathbf{r}',t) = \delta(\mathbf{r}-\mathbf{r}') - \phi_c^*(\mathbf{r},t)\phi_c^*(\mathbf{r}',t)$, and so projects $\hat{\Psi}(\mathbf{r})$ onto all modes orthogonal to $\phi_c(\mathbf{r},t)$. Considering Eq. (1.29) we see that we have reformulated our problem to be in terms of the operators $\hat{a}_c(t)$ and $\hat{\delta}_{\rm n}(\mathbf{r},t)$ (and their respective creation operators). It should be noted that the only non-zero commutators are [129]

$$[\hat{a}_c(t), \hat{a}_c^\dagger(t)] = 1, \tag{1.39}$$

$$[\hat{\delta}_{\rm n}(\mathbf{r},t), \hat{\delta}_{\rm n}^\dagger(\mathbf{r}',t))] = Q(\mathbf{r},\mathbf{r}',t). \tag{1.40}$$

This formalism neither breaks symmetry [as the condensate's phase is undetermined through the retention of $\hat{a}_c(t)$] nor leads to non-orthogonality [as $\mathcal{Q}(\mathbf{r}, \mathbf{r}', t)$ explicitly determines $\hat{\delta}_{\rm n}(\mathbf{r}, t)$ to be orthogonal to the condensate mode] and so allows us to develop a self consistent number-conserving theory of BEC dynamics even in the limit of finite temperature or low particle number (where the non-condensate has a non-negligible population).

Small and large parameters

As with the symmetry-breaking formalism, we can consider the Heisenberg picture equations of motion of an appropriate fluctuation operator in order to determine the full dynamics of the system, again using a small operator to perform a fluctuation expansion about zeroth order.

In the number-conserving formalism, we consider an operator which removes a particle from the non-condensate and creates one in the condensate [129], and so has the form

$$\hat{\Lambda}(\mathbf{r}, t) = \frac{1}{\sqrt{\hat{\mathcal{N}}}} \hat{a}_c^\dagger(t) \hat{\delta}_{\rm n}(\mathbf{r}, t). \tag{1.41}$$

The denominator $\sqrt{\hat{\mathcal{N}}}$ is generally taken to be a number operator and should be of order $\sqrt{N_c(t)}$ in order to keep our fluctuation operator of the order of the condensate fraction. There are three possible candidates for this operator [129]: $\hat{\mathcal{N}} = \hat{N}$, the total number operator; $\hat{\mathcal{N}} = N_c(t)$, the condensate number eigenvalue; or $\hat{\mathcal{N}} = \hat{N}_c(t)$ the condensate number operator. These three alternatives are judged on how well the resulting $\hat{\Lambda}$ satisfies three desirable conditions: it must be a good fluctuation operator, such that $\langle \hat{\Lambda}(\mathbf{r}, t) \rangle = 0$; it must scale as the non-condensate fraction, such that $\hat{\Lambda} \propto \sqrt{N_n(t)}$; and it should describe bosonic quasiparticles, such that $[\hat{\Lambda}(\mathbf{r}', t), \hat{\Lambda}^\dagger(\mathbf{r}, t)] = \delta(\mathbf{r} - \mathbf{r}')$.

Figure 1.2 shows how the different denominator candidates perform. The first, $\sqrt{\hat{N}}$ (used by Castin and Dum [127, 128]) is a good fluctuation operator (having zero mean), but only scales correctly in the $N_n(t) \ll N$ limit and has only approximately bosonic quasiparticles. The second, $\sqrt{N_c(t)}$ (used by Gardiner and Morgan [129]) is also a good fluctuation operator, and has the extra benefit that it scales correctly for all $N_n(t)$, but again has only approximately bosonic quasiparticles. The third, $\sqrt{\hat{N}_c(t)}$ has bosonic quasiparticles and scales exactly with the non-condensate fraction, but is not a well defined fluctuation operator.

We will now adopt the approach of Gardiner and Morgan [129], in that we prioritise

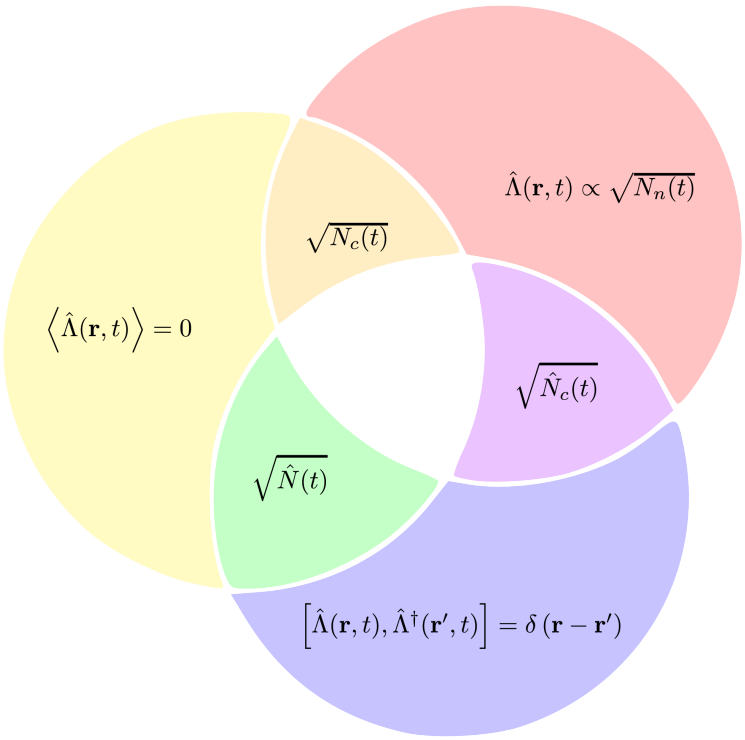

Figure 1.2: Fluctuation operator rescaling factors and their validities for a non-negligible thermal fraction. The blue region satisfies bosonic quasiparticles, the yellow region contains well defined fluctuation operators and the red region scales appropriately with the non-condensed fraction [129].

that $\hat{\Lambda}(\mathbf{r},t)$ scale correctly and be a good fluctuation operator. This selection is largely unimportant in the current context, as the differences in analysis engendered by the selection will not affect the work presented in this thesis, and the outcomes are broadly similar up to some subtle caveats. However, a selection must be made in order to continue. As such, we select $\sqrt{N_c(t)}$ as our denominator:

$$\hat{\Lambda}(\mathbf{r},t) = \frac{1}{\sqrt{N_c(t)}} \hat{a}_c^\dagger(t) \delta\hat{\Psi}(\mathbf{r},t). \tag{1.42}$$

Beyond this point the derivations and considerations become somewhat involved. For instance, third order factorisations of the Hamiltonian require the assumption that fluctuations in the dynamics operator $\hat{\Lambda}(\mathbf{r},t)$ are essentially Gaussian. This allows a process analogous to the HF and HFB formulation of the symmetry-breaking dynamics [133] but is not consistent to fourth order as it requires that terms of magnitude comparable to fourth order terms be discarded [117]. As such, the higher order dynamics of the condensate will not be discussed further in this thesis. We will stop at identifying a set of candidates for the fluctuation operator and illustrate

how one of these operators can be used to determine the GPE.

Zeroth order expansion

In order to approximate the dynamics to first order, the full second quantised Hamiltonian must be expanded in terms of Eq. (1.29) and then reduced to first order in $\hat{\Lambda}(\mathbf{r}, t)$, yielding [129]

$$\begin{aligned}\hat{H}_1^{\mathrm{nc}} =& N_c \int d\mathbf{r} \phi_c^*(\mathbf{r}, t) \left[\hat{h}_1(\mathbf{r}) + \frac{gN_c}{2}|\phi_c(\mathbf{r}, t)|^2\right] \phi_c(\mathbf{r}, t) \\ &+ \sqrt{N_c} \int d\mathbf{r} \left\{\phi_c^*(\mathbf{r}, t) \left[\hat{h}_1(\mathbf{r}) + gN_c|\phi_c(\mathbf{r}, t)|^2\right] \hat{\Lambda}(\mathbf{r}, t) + \mathrm{H.c.}\right\},\end{aligned} \tag{1.43}$$

with H.c. denoting the hermitian conjugate. Substituting Eq. (1.42) into Eq. (1.28) yields, to first order and taking care with explicit time dependencies,

$$i\hbar \frac{d}{dt}\hat{\Lambda}(\mathbf{r}, t) = [\hat{\Lambda}(\mathbf{r}, t), \hat{H}_1^{\mathrm{nc}}] - \sqrt{N_c} \int d\mathbf{r}' \boldsymbol{Q}(\mathbf{r}, \mathbf{r}', t) \left[i\hbar \frac{\partial}{\partial t}\psi_c(\mathbf{r}', t)\right] \tag{1.44}$$

Since the fluctuation operator has zero expectation and the statistical average commutes with the time derivative, taking the average of Eq. (1.44) gives us the fully 3D Gross–Pitaevskii equation

$$i\hbar \frac{\partial \phi_c(\mathbf{r}, t)}{\partial t} = \left[-\frac{\hbar^2}{2m}\nabla^2 + U_{\mathrm{ext}}(\mathbf{r}) + gN_c|\phi_c(\mathbf{r}, t)|^2 - \lambda_0\right] \phi_c(\mathbf{r}, t), \tag{1.45}$$

where λ_0 is a global energy offset, defined as

$$\lambda_0 = \int d\mathbf{r} \phi_c^*(\mathbf{r}, t) \left[-\frac{\hbar^2}{2m}\nabla^2 + U_{\mathrm{ext}}(\mathbf{r}) + gN_c|\phi_c(\mathbf{r}, t)|^2 - i\hbar \frac{\partial}{\partial t}\right] \phi_c(\mathbf{r}, t), \tag{1.46}$$

which can generally be discarded as an arbitrary global phase [81].

1.4 Classical analysis of dimensionality

Now that we have determined the dynamical equation governing the lowest order approximation of the BEC we will make one final approximation in order to obtain the dynamics equation which the results of this thesis will focus on. This is the reduction to 1D. First, however, we must outline a 3D effect which cannot be overlooked, namely the collapse threshold, and point out a method of making this analysis.

1.4.1 Collapse in attractive condensates

The Pérez-García treatment

As previously mentioned, through the use of Feshbach resonances it is possible to tune the scattering length of the atoms in a BEC to a wide range of values, positive or negative. As such, we can create both dispersive (repulsive, $a_s > 0$) or self-focusing (attractive $a_s < 0$) condensates. Dispersive condensates will not be discussed in the current thesis, but are interesting systems in that they support a wide range of fundamental excitations (including vortices and dark solitons) and intriguing behaviours. In this thesis we consider the self-focusing case only, such that we can create bright solitary waves and solitons (as opposed to the dark solitary waves and solitons of the dispersive GPE).

An important feature of the dynamics of the self-focusing GPE is the collapse threshold. Clearly, the presence of attractive interactions will increase the rate of inelastic two-body collisions and three-body collisions resulting in depletion. However, even if this process is ignored, the 3D GPE is fundamentally unstable to collapse when unconfined. This phenomenon has been observed and investigated experimentally [80, 134–138] and through extensive theoretical investigations [139–151]. In particular, here we will highlight the work of Pérez-García *et al.* [152], where a variational method was employed to determine regions of stability in the GPE by assuming a 3D Gaussian profile of the condensate.

Considering a condensate wavefunction denoted as $\psi(\mathbf{r}, t)$ and taking the classical Lagrangian density functional $\mathcal{L}[\psi]$

$$\mathcal{L}[\psi] = \frac{i}{\hbar}\left(\psi\frac{\partial\psi^*}{\partial t} - \psi^*\frac{\partial\psi}{\partial t}\right) - \frac{\hbar^2}{2m}|\nabla\psi|^2 + \frac{m\nu^2}{2}\left(\lambda_x^2x^2 + \lambda_y^2y^2 + \lambda_z^2z^2\right)|\psi|^2 + \frac{2\pi a_s\hbar^2}{m}|\psi|^4. \tag{1.47}$$

The λ_η and ν parameters describe the harmonic trapping aspect ratios and base frequency. We then vary the parameters of some ψ *ansatz* to get a minimal extrema in the action $\int \mathcal{L} d\mathbf{r}dt$. This is the classical mechanical approach wherein the action is made extremal by taking the Euler–Lagrange (E–L) equations for some free parameters of the *ansatz*. Pérez-García *et al.* selected a Gaussian *ansatz* for this purpose [152]:

$$\psi(\mathbf{r}, t) = A(t)\prod_{\eta=x,y,z}\exp\left\{-\left[\eta - \eta_0(t)\right]^2/2w_\eta^2 + i\eta\alpha_\eta(t) + i\eta^2\beta_\eta(t)\right\}. \tag{1.48}$$

The parameter η runs over the x, y, z coordinates. Substituting this *ansatz* [Eq. (1.48)] into our Lagrangian density [Eq. (1.47)] and integrating over the spatial coordinates, we obtain the effective Lagrangian[2]

$$\begin{aligned} L = \int d\mathbf{r}\mathcal{L} = \frac{\pi^{3/2}}{2} w_x w_y w_z \Bigg\{ & i\hbar\left(A^*\dot{A} - A\dot{A}^*\right) \\ & + |A|^2 \sum_{\eta=x,y,x} \Bigg[\left(\dot{\beta}_\eta - \frac{2\hbar^2}{m}\beta_\eta^2 - \frac{1}{2}m\nu^2\lambda_\eta^2\right)\left(w_\eta^2 + 2\eta_0^2\right) \\ & - \frac{\hbar^2 w_\eta^2}{2m} + \frac{\hbar^2\alpha_\eta^2}{m} + 2\eta_0\left(\dot{\alpha}_\eta - \frac{2\hbar^2}{m}\alpha_\eta\beta_\eta\right)\Bigg] \\ & + \frac{\sqrt{2}\pi\hbar^2 a}{m}|A|^4 \Bigg\}. \end{aligned} \tag{1.49}$$

Taking the E–L equations of our effective Lagrangian L,

$$\frac{d}{dt}\left(\frac{\partial L}{\partial \dot{q}_j}\right) - \frac{\partial L}{\partial q_j} = 0, \tag{1.50}$$

gives us a set of dynamics equations for all parameters

$$q \equiv \{w_x, w_y, w_z, A, A^*, x_0, y_0, z_0, \alpha_x, \alpha_y, \alpha_z, \beta_x, \beta_y, \beta_z\}. \tag{1.51}$$

For clarity, w_η denotes the Gaussian width, A is the complex amplitude, η_0 denotes the centre of mass position, α_η denotes the linear phase contributions (or slope, which can be shown to be unimportant) and β_η describes the curvature radius.

It can be shown that the only true dynamical variables of note are the $\eta_0(t)$ and $w_\eta(t)$. All other variables are fixed or can be determined from the width and COM position. The COM position coordinates are shown to follow simple harmonic motion, and the width and COM dynamics are independent. This is an interesting result, which will later be confirmed through a different methodology. Simply put, a harmonically trapped condensate's internal dynamics and COM position can be shown to decouple (for both Gaussian [152] and solitonic parameter regimes [153]) from the condensate's internal degrees of freedom. This can be a useful characteristic,

[2]It is strongly recommended that any reader who would like to use the Pérez-García analysis, or similar variational methods, take great care as inconsistencies in notation are a common pitfall with such laborious algebraic manipulation. Here we have transcribed exactly from Ref. [152] in order to outline the process and broader results.

and will be used later. If we now consider the width dynamics, we find

$$\ddot{w}_\eta + \lambda_\eta^2 \nu^2 w_\eta = \frac{\hbar^2}{m^2 w_\eta^3} + \sqrt{\frac{2}{\pi}} \frac{a\hbar^2 N}{m^2 w_x w_y w_z w_\eta}. \tag{1.52}$$

This system of PDEs describes a particle with position ν_η (essentially a rescaling of the widths w_η) moving in a 3D potential

$$\begin{aligned} V_{\mathrm{p}}(\nu_x, \nu_y, \nu_z) = \frac{1}{2}\left(\lambda_x^2 \nu_x + \lambda_y^2 \nu_y + \lambda_z^2 \nu_z\right) \\ + \frac{1}{2\nu_x^2} + \frac{1}{2\nu_y^2} + \frac{1}{2\nu_z^2} + \frac{P}{\nu_x \nu_y \nu_z}. \end{aligned} \tag{1.53}$$

If we consider this potential we see that the key parameter $P = \sqrt{2/\pi} N a_s / a_0$ is fundamental in determining whether or not there is a local minimum corresponding to $w_\eta \neq 0$. Any of the w_η going to zero signifies collapse. In Fig. 1.3 we consider the spherically symmetric case ($\lambda_\eta = 1$, $w_\eta = \nu$) with the condensate initially "at rest" ($\dot{w}_\eta = 0$), giving the 1D equation of motion

$$\frac{\partial^2 \nu}{\partial \tau^2} + \nu = \frac{1}{\nu^3} - \frac{|P|}{\nu^4}. \tag{1.54}$$

This is essentially the motion of a particle in the potential

$$V_{\mathrm{1D}}(\nu) = \frac{\nu^2}{2} + \frac{1}{2\nu^2} - \frac{|P|}{3\nu^3}. \tag{1.55}$$

Note that τ is simply a dimensionless rescaling of the time variable. To obtain the critical point ν_c, where the condensate is stable, we set the potential's first and second derivatives to zero (such that the "particle" does not accelerate), yielding

$$\begin{aligned} \nu_c &= \frac{1}{\nu_c^3} - \frac{|P|}{\nu_c^4}, \\ 1 &= -\frac{3}{\nu_c^4} + \frac{4|P|}{\nu_c^5}. \end{aligned} \tag{1.56}$$

This tells us that Eq. (1.54) has a stable region for $|P| < |P_c| = 4/5^{5/4}$. When this is the case, the width oscillates around a local minimum in the potential. If this is not the case then ν (and consequently w_η) decays to zero and the condensate collapses.

Similar analyses can be conducted for different trapping geometries where 3D harmonic trapping is employed (namely prolate and oblate) [139, 145, 147, 148] and different *ansätze* [16, 25, 146, 151, 154].

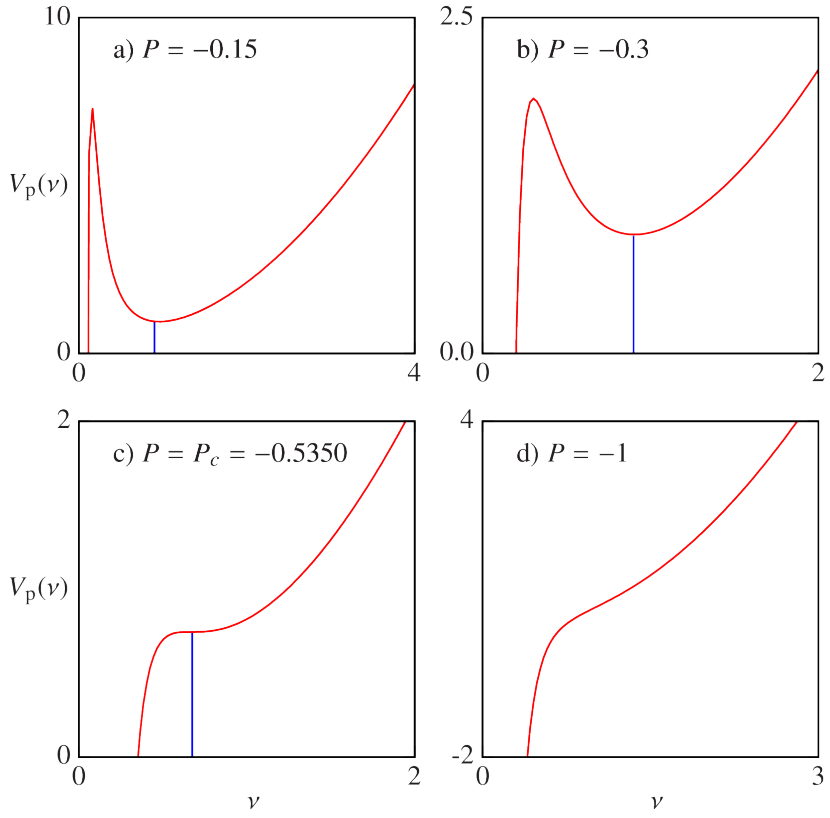

Figure 1.3: Regions of stability in the GPE: Here we show various instances of the "particle" potential of the widths of the symmetric Gaussian *ansatz* to the GPE. For $|P| < |P_c|$ [a),b)] we see a stable region wherein the width oscillates without collapsing. For $|P| = |P_c|$ [c)] we see that there is an unstable state where the width can remain but is unstable to any perturbation. For $|P| > |P_c|$ [d)] the condensate will always collapse. The blue labelling lines indicate the turning point in the potential.

The Salasnich treatment

A second such analysis of note was carried out by Salasnich *et al.* [147]. In this variational method the radial and axial dynamics are separated through the *ansatz*

$$\psi(\mathbf{r}, t) = \phi(y, z, t; \sigma_f(x, t)) f(x, t) \tag{1.57}$$

where $\phi(y, z, t; \sigma_f(x, t))$ is the radial wavefunction parameter defined as

$$\phi(y, z, t; \sigma_f(x, t)) = \frac{e^{-[y^2+z^2]/2\sigma_f(x,t)^2}}{\pi^{1/2}\sigma_f(x, t)}. \tag{1.58}$$

where $\sigma_f(x,t) = a_\perp^2\sqrt{1+2a_sN|f(x,t)|^2}$ is the Gaussian radial width. Through action minimisation via the E–L equation for $f(x,t)$ Salasnich obtained the non-polynomial Schrödinger equation (NPSE) [155]

$$i\hbar\frac{\partial f(x,t)}{\partial t} = \left[-\frac{\hbar^2}{2m}\frac{\partial^2}{\partial x^2} + V_{\text{ext}}(x,t) + \frac{1+(3/2)(2a_s/a_\perp)|f(x,t)|^2}{\sqrt{1+(a_s/a_\perp)|f(x,t)|^2}}\right]f(x,t). \quad (1.59)$$

this equation is particularly powerful, as it allows the determination of the width $\sigma_f(x,t)$ which becomes zero upon collapse. This can be seen to result in a divergent non-linear term, illuminating the concept that this collapse is brought about by a catastrophic over-focusing of the condensate. Furthermore, this equation allows for the consideration of 3D collapse behaviour in a 1D system. This method has been used to find collapse events in systems where solitons interact with narrow potentials, and showed good qualitative agreement with 3D methods [45].

1.4.2 1D reduction and soliton units

It is now widely accepted that sufficiently (i.e. very) prolate geometries are well suited to supporting effectively 1-D dynamics [15, 16, 146, 147, 156, 157]. There are two main requirements associated with the 1D regime: the radial direction confinements must be much tighter than the axial confinement, $\omega_y = \omega_z = \omega_r \gg \omega_x$, essentially freezing out radial excitations and dynamics; and the radial confinement must not be so tight that the scattering is no longer 3D, with $\omega_r \ll (\hbar/ma_s)^{1/2}$. While under these conditions the condensate may be described as effectively 1D, the reduction is not perfect, especially for attractive condensates [25].

This allows us to substitute the factorisation

$$\phi(\mathbf{r},t) = \Psi(x,t)\Phi(y,z), \quad (1.60)$$

where

$$\Phi(x,t) = \left(\frac{m\omega_r}{\pi\hbar}\right)^{1/2}\exp\left[-\frac{m\omega_r}{2\hbar}\left(y^2+z^2\right)\right] \quad (1.61)$$

into Eq. (1.45), yielding

$$i\hbar\frac{\partial\Psi(x,t)}{\partial t} = \left[-\frac{\hbar^2}{2m}\frac{\partial^2}{\partial x^2} + U_{\text{ext}}(x,t) - g_{1\text{D}}N|\Psi(x,t)|^2 - \lambda_1\right]\Psi(x,t), \quad (1.62)$$

Where λ_1 is the energy associated with the radial groundstate and can, again, be discarded as a global phase. We have rescaled the strength of our nonlinearity to $g_{1\text{D}} = 2\hbar\omega_r|a_s|$.

The final adaptation we can make to our dynamics equation is a dimensionless rescaling. For the purposes of the work presented in this thesis, the soliton rescaling is the most appropriate [25]. As such, we take position units of $\hbar^2/mgN$, time units of $\hbar^3/mg^2N^2$, and energy units of $mg^2N^2/\hbar^2$ we obtain the dimensionless, quasi-1D GPE

$$i\frac{\partial\psi(\tilde{x},\tilde{t})}{\partial\tilde{t}} = \left[-\frac{1}{2}\frac{\partial^2}{\partial\tilde{x}^2} + \frac{\tilde{\omega}^2\tilde{x}^2}{2} - \left|\psi(\tilde{x},\tilde{t})\right|^2\right]\psi(\tilde{x},\tilde{t}), \tag{1.63}$$

where $\tilde{\omega}$ denotes the dimensionless axial trapping frequency and the dimensionless wave function is $\psi(\tilde{x},\tilde{t}) = \hbar\Psi(x,t)/\sqrt{mgN}$.

It is helpful to characterise these units in terms of typical experimental parameters. The following information is determined using experimental parameters for a condensate of ^{85}Rb atoms [10], expressed in S.I. units:

$$\begin{aligned} N &= 4000 \\ m &= 85\text{u} \\ a_s &= -11a_0 \\ \omega_r &= 2\pi \times 17.3\text{Hz} \\ \omega_x &= 2\pi \times 6.92\text{Hz} \end{aligned}$$

Where $u = 1.66 \times 10^{-27}$kg is the atomic mass unit, and $a_0 = 5.29 \times 10^{-11}$m is the Bohr radius. The non-linearity is now quantified by

$$g_{1\text{D}} = 2\hbar\omega_r|a_s| = -1.37 \times 10^{-41}\text{kg m}^3\text{s}^{-2}$$

Working in soliton units:

$$\begin{aligned} x &= \frac{\hbar^2}{mg_{1\text{D}}N}\tilde{x} && = (1.43 \times 10^{-6}\text{m}) \times \tilde{x} \\ t &= \frac{\hbar^3}{mg_{1\text{D}}^2N^2}\tilde{t} && = (2.73 \times 10^{-3}\text{s}) \times \tilde{t} \\ v &= \frac{g_{1\text{D}}N}{\hbar}\tilde{v} && = (5.22 \times 10^{-4}\text{ms}^{-1}) \times \tilde{v} \\ E &= \frac{mg_{1\text{D}}^2N^2}{\hbar^2}\tilde{E} && = (3.84 \times 10^{-32}\text{kg m}^2\text{s}^{-2}) \times \tilde{E} \end{aligned}$$

where tildes denote dimensionless variables and quantities. This notation will be omitted for brevity after this point.

Chapter 2: Solitons in the nonlinear Schrödinger equation

2.1 Introduction

As noted previously, the macroscopic quantum nature of BECs can be used as a powerful tool in that we can observe wave-like features in the behaviour of matter on large scales, but this begs the question of what other features are intrinsic to BECs. The goal of our analysis in this chapter is to identify robust structures within BECs and determine how they behave and to what uses they can be put. In the case of condensates of mutually attractive atoms, where the *s*-wave scattering length is negative, recent experiments [8, 10, 34, 158] report the existence of localised, finite sized wave-packets within the condensate. These bright solitary waves retain their shape even when in close proximity to one-another, despite the intrinsically attractive nature of the condensate, and so are in some sense topological features of the system. These excitations are often referred to as solitons [10], and are physical analogues to the topological defect of the same name [159–161]. In this chapter we will describe the nature of these structures and the mathematical tools available to those who wish to study them.

In the previous chapter we developed a description of BECs which was complete up to the degree of second quantisation [82]. However, this degree of completeness is not a stringent requirement for the analysis to illuminate the fundamental quantum nature of the system. Under the Copenhagen interpretation, the standard interpretation of quantum mechanics, the probabilistic nature of quantum mechanical states is key. Our 1D leading order approximation, the GPE [Eq. (1.63)], is used to define the probability density function (PDF) of the atoms in the condensed state in the quasi-1D system. The GPE is , from a mathematical perspective, a partial differential equation (PDE), and so we can analyse the coarse-grained quantum mechanical characteristics of the system using the more classical tools of PDE analysis.

We will now adopt the ideas of the wave equation to describe the dynamics exhibited by the GPE, and so allow us to better understand bright solitary matter-waves. Wave equations determine the dynamics of a field over some spatial domain (with appropriate boundary and initial -conditions) [159]. As such they are PDEs contain-

ing spatial and temporal derivatives. Essentially, we can consider the propagation of oscillations and pulses through a classical field $u(x,t)$ (which describes our wave function PDF) by considering the structure of the dynamics equation associated with that field. The fundamental form of Eq. (1.63), in the absence of external potentials, is that of the focusing non-linear Schrödinger equation (NLSE), a commonly discussed wave equation:

$$iu_t + \frac{u_{xx}}{2} + u\,|u|^2 = 0. \tag{2.1}$$

Here the subscripts denote a partial derivative. Before we analyse this equation, we will first develop an understanding of some of the basic behaviours such a system can exhibit.

2.2 Fundamentals of wave behaviour

2.2.1 Simple harmonic motion

Here we will follow ideas presented in [159] to introduce some fundamental wave behaviours. Wave propagation can be introduced with simple harmonic motion in 1D, as described by

$$u_{tt} - c^2 u_{xx} = 0 \tag{2.2}$$

This simple model will allow us to develop a framework within which we can consider various types of wave behaviour. Studying Eq. (2.2) we see that the amplitude's acceleration at any point is proportional to how quickly its gradient varies spatially at that point. If we consider a region where the amplitude varies from zero, up to some finite value and then returns to zero (also requiring that the amplitude varies smoothly, slowly and is single valued) we see that where the gradient is positive or zero it will accelerate to zero, and that where the gradient is negative it will accelerate away from zero. This describes a pulse in the amplitude which travels through the medium as the amplitude at a given point oscillates. This is, of course, our wave. The variable c can be seen to be the wave's speed of translation if we introduce characteristic variables $(x \pm ct)$ such that our solution has the form

$$u(x,t) = f(x - ct) + g(x + ct), \tag{2.3}$$

where f and g are functions which are well defined up to their second derivatives. Equation (2.3), known as *d'Alambert's solution*, describes two wave forms f and g moving in opposite directions [159]. A useful example of such a solution is, of

course,

$$u(x,t) = e^{i(kx-\omega t)}. \tag{2.4}$$

$$\tag{2.5}$$

This is the elementary harmonic wave solution with wavenumber k, frequency ω and wave speed $c = \omega/k$.

2.2.2 More complex wave equations

Linear wave properties

As elementary as Eq. (2.2) may seem, let us reduce it further, and consider a system where waves can move in one direction only:

$$u_t + cu_x = 0. \tag{2.6}$$

Any twice differentiable solution of this equation is a solution of Eq. (2.2), but the reverse is not true, and so the set of solutions to Eq. (2.6) is a subset of Eq. (2.2)'s solutions, given by

$$u(x,t) = f(x - ct). \tag{2.7}$$

Notice that Eq. (2.3) is a linear combination of Eq. (2.7) and a second set of solutions g. This is the superposition principle, which applies to linear systems such as Eqs. (2.2) and (2.6). Simply put, the sum of any two solutions to a linear equation is also a solution to that equation. We will revisit this concept later.

Now let us add terms to this equation and consider their implications. For instance, let us add a third-order spatial derivative, yielding

$$u_t + u_x + u_{xxx} = 0. \tag{2.8}$$

We can successfully seek a solution of the form Eq. (2.5). This treatment yields a dispersion relation between the frequency ω and wave number k of the form

$$\omega = k - k^3, \tag{2.9}$$

and so the wave speed is

$$c = \frac{\omega}{k} = 1 - k^2.$$

This tells us that waves of differing wavelength (different values of k) move at dif-

ferent speeds, and so we might call Eq. (2.8) a *dispersive* wave equation [159].

Similarly, adding in a second order spatial derivative to Eq. (2.6),

$$u_t + u_x - u_{xx} = 0, \tag{2.10}$$

yields the dispersion relation

$$\omega = k - ik^2. \tag{2.11}$$

In a harmonic wave solution the imaginary part of the frequency causes the harmonic wave solution's amplitude to decay exponentially over time, and so we might call Eq. (2.10) a *dissipative* wave equation [159].

Nonlinear wave properties

We now broaden our investigation to nonlinear terms and their characteristics. For instance, equations of the form

$$u_t + a(u)u_x = 0 \tag{2.12}$$

yield no non-trivial solutions after application of the harmonic wave *ansatz*. Instead, we employ the method of characteristics. This is a standard method for the solution for first order nonlinear PDEs [162]. To use this methodology, we will first consider the formulation of conservation equations, following Ref. [163]. Beginning in full 3D we note that the rate of change of a physical entity within a region G bounded by surface S is determined by the flux out of that region, $\mathbf{f} \cdot \mathbf{n}$, and write

$$\frac{d}{dt} \iiint_G u d\mathbf{r} = - \oiint_S \mathbf{f} \cdot \mathbf{n} dS. \tag{2.13}$$

This equation asserts that the rate of change of the integral of u is equal to the flux of u normal to the boundaries of G. Through the divergence theorem, allowing G to tend to a point and considering our problem in 1D we obtain the conservation equation,

$$u_t + f_x = 0. \tag{2.14}$$

We now assume that the flux f depends on u alone and is nonlinear in u. We then assert that

$$\frac{df}{du} = a(u), \tag{2.15}$$

and note that Eqs. (2.12) and (2.14) are equal under this assertion, making Eq. (2.12) a conservative equation [162–164]. As such we can determine a family of curves

$x_c(t)$ along which u remains constant by setting

$$\begin{aligned}\frac{d}{dt}u(x_c[t],t) =& u_t + u_x x_t \\ =& 0\end{aligned} \tag{2.16}$$

and equating this with Eq. (2.12). Note that the notation on the left-hand side of Eq. (2.16) is intended to highlight that $u(x_c,t)$ is purely a function of t, and the square brackets merely describe x_c's dependence on t. This shows that u is constant along the curves satisfying

$$\frac{dx_c}{dt} = a(u). \tag{2.17}$$

These are the characteristic curves with signal speed $a(u)$. Taking the initial condition

$$u(x,0) = u_0(x) \tag{2.18}$$

we can formulate a solution of the form

$$u(x,t) = u_0(x - a[u_0]t). \tag{2.19}$$

We will now point out the major problem with this solution. Let us take $a_u > 0$, such that Eq. (2.12) is genuinely nonlinear [163], and consider the time and space derivatives. According to the implicit function theorem [163] we obtain

$$u_t = -\frac{u_0' a}{1 + u_0' a_u t} \qquad \text{and} \qquad u_x = \frac{u_0'}{1 + u_0' a_u t} \tag{2.20}$$

for small t. These equations clearly satisfy Eq. (2.12), and if $u_0' \geq 0$ then the characteristic curves are divergent in the positive t direction, and so the initial condition can propagate indefinitely and remain single valued as the wave form of u dissipates [163]. However, if $u_0' < 0$ then both parts of (2.20) are divergent. In this scenario the characteristic curves issuing from two points $y_1 < y_2$ (with associated amplitudes $u_1 = u_0(y_1) > u_0(y_2) = u_2$ and speeds $a_1 = a(u_1) > a(u_2) = a_2$) will cross at time $t_s = (y_2 - y_1)/(a_1 - a_2)$. When this occurs u_x becomes infinite and $u(x,t)$ is no longer single valued. Our wave topples [159]. This crossing of characteristic curves is known as a shock wave and is an inherent problem of the solution of nonlinear wave equations in terms of both stability and solution [164].

Combination of behaviours

The benefit of this analysis is to consider the outcome of mixing one or more of the above behaviours. If an equation were amenable to a solution constructed in such a way that the nonlinear term could counteract the effects of dissipation and dispersion then that solution could translate along the x-axis coherently and indefinitely. Equations such as the Korteweg-de Vries (KdV) equation [165] and the NLSE are amenable to just such a type of solution [159–161]. These are the fabled soliton solutions.

2.3 Solutions to nonlinear equations and the NLSE

2.3.1 Fourier and inverse scattering transforms

A noteworthy feature of the NLSE is that the nonlinear $|u|^2$ term and the dissipative u_{xx} term[1] can counteract one another and lead to stable travelling wave solutions. However, as shown above the nonlinearity is a more difficult feature to describe as it is not amenable to simpler methods of solution. In particular, (2.1) is not amenable to solution by linear combination of other solutions. This is a fundamental property of nonlinear equations and is a severe impediment to their easy solution. For instance, equations such as (2.2) and (2.6) can be informatively solved by a Fourier transform of the form

$$A(k,t) = \int_{-\infty}^{\infty} u(x,t)e^{-2\pi ikx}dx. \tag{2.21}$$

This is effectively the Fourier transform of u in momentum space (although k has units of inverse length). Once obtained, the wavenumber amplitudes A can often be evolved in time more efficiently than when represented in the spatial basis, as spatial derivative operations can be easily carried out via wavenumber multiplication, and so the dispersion relation of the dynamical equation can be used to easily evolve the system. After this evolution, the spatial representation can be retrieved by the transform

$$u(x,t) = \int_{-\infty}^{\infty} A(k,t)e^{2\pi ikx}dk. \tag{2.22}$$

Such transform pairs are particularly useful in a numerical context, as there exist a number of well optimised libraries of spectral methods based on the Fourier transform [166]. These transforms, however, depend on linear superpositions being a

[1] In Eq. (2.10) u_{xx} was said to have dissipative, not dispersive properties. However, in the NLSE the presence of the complex factor i in the time derivative term alters this behaviour.

valid solution to the initial equation.

The nonlinear analogue to Fourier transforms, *inverse scattering transforms*, utilise a similar process: the spatial data are transformed into some new basis, the scattering data $\mathcal{S}$; the scattering data are then evolved in time by an appropriate dynamical equation; and at the end of this evolution the data are transformed back. Furthermore, the scattering data can be used to construct complete solutions and illuminate the behaviour of these solution.

There are many methodologies of the inverse scattering transform, (See Refs. [159–161, 165, 167]). Here we will give a brief sketch of the behaviour common to all of these techniques and discuss what features this behaviour shows us. All the approaches are, in essence, the reformulation of the nonlinear equation in terms of an auxiliary linear scattering problem [168],

$$\psi_{xx} + (u - \lambda)\psi = 0 \tag{2.23}$$

where the initial condition of the nonlinear problem, $u(x, 0)$, acts as a potential. The construction of an operator which achieves this transformation is the first major hurdle to creating an inverse scattering transform, as there is no process or algorithm which is guaranteed to be successful, and in general is found through shrewd guesswork [159, 160, 165].

The illuminating features come from consideration of the eigenvalues of the linear problem, which has eigenfunctions in the form [159, 168]

$$\hat{\psi}(x; k) \sim \begin{cases} e^{-ikx} + b(k)e^{ikx} & \text{as } x \to +\infty \\ a(k)e^{-ikx} & \text{as } x \to -\infty, \end{cases} \tag{2.24}$$

and

$$\psi_n(x) \sim c_n e^{-\kappa_n x} \text{ as } x \to +\infty \tag{2.25}$$

Here $k^2 = \lambda > 0$ denotes the continuous spectrum of eigenvalues and corresponding eigenfunctions $\hat{\psi}(x; k)$. These eigenfunctions are oscillatory as $x \to \pm\infty$ and so the first exponential in equation (2.24) can be thought of as an incident wave while $a(k)$ and $b(k)$ denote the amplitudes of that wave transmitted or reflected by the potential $u(x, 0)$.

The discrete spectrum denoted by $-\kappa_n^2 = \lambda_n < 0$ corresponds to eigenfunctions ψ_n with amplitudes c_n for $n = 1, 2, 3...N$. These parts of the solution decay as $x \to \pm\infty$

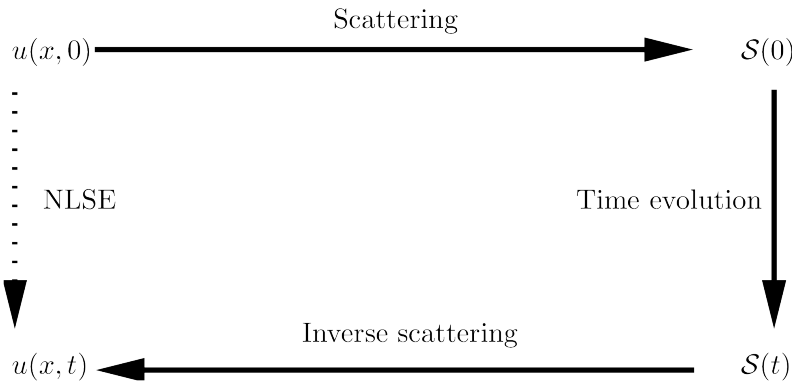

Figure 2.1: Schematic of the inverse scattering technique

and so form discrete wave packets and represent bound states in the scattering problem which are poles in the upper half complex-plane of the scattering eigenvalue. This presence as a topological defect is what affords solitons their stability, in a mathematical sense [159].

Once the initial scattering data have been determined it is then necessary to use the nonlinear wave equation in question to develop a method of time evolution for the scattering data. Determining this time evolution is the second major obstacle in constructing an inverse scattering transform for a particular wave equation.

Finally it is necessary to reconstruct our solution $u(x,t)$ as the solution to the inverse scattering problem. This process uses the result [159–161, 165, 165, 167]

$$u(x,t) = -2\frac{d}{dx}K(x,x;t), \tag{2.26}$$

where $K(x,z;t)$ (here t plays the role of a parameter) is the solution of the Marchenko equation

$$K(x,z;t) + F(x+z;t) + \int_x^\infty K(x,y)F(y+z)dy = 0 \tag{2.27}$$

and

$$F(X) = \sum_{n=1}^{N} c_n^2(t)e^{-\kappa_n X} + \frac{1}{2\pi}\int_{-\infty}^{\infty} b(k;t)e^{ikX}dk \tag{2.28}$$

is constructed from our time dependent scattering data.

Through application of the methods of inverse scattering transforms, not only can the dynamics of nonlinear equations be determined exactly, but the structure and dynamics of topological defects can be described. This makes the inverse scattering transform a powerful, if capricious, tool in the analysis of nonlinear problems.

2.3.2 NLSE solutions

Inverse scattering transforms, with their links to integrability [161], are often considered to be the fundamental mathematical definition of solitons. However, a more pragmatic definition relies on the excitations having the characteristics of localised stability and robustness to collision with one-another. This definition is common because these characteristics are of particular interest in experimental terms, and so they are often considered the most important characteristics of solitons [30, 45, 169].

We will now show that the NLSE does indeed support stable-travelling wave solutions. The derivation that follows is a specific case of a more complete analysis presented in Appendix A. The analysis in Appendix A is concerned with the exact form of travelling wave solutions to the NLSE when considered in a translational frame of reference, and will be relevant to later results. Here we present the case retrieved when the speed of translation is zero. We will leave the question of the multiple soliton case, and the associated question of collisional stability, to the literature concerned with the properties of inverse scattering transforms [159–161]. We will begin by seeking solutions to Eq. (2.1) of the form

$$u = re^{i(\theta+nt)} \tag{2.29}$$

as suggested in Ref. [159]. As such, we set r and θ to be functions of the variable $\xi = x - ct$. We also assert that r and θ are real (as any imaginary component in these functions would result in exponential growth or decay of the solution, which is incompatible with our stability requirement) and note that r^2 must be ≥ 0 for a meaningful solution. Substitution of this *ansatz* into the NLSE and separation into real and imaginary parts yields, from the imaginary part,

$$\theta' = c + \frac{A}{r^2}. \tag{2.30}$$

Here, A is an arbitrary real constant of integration and the prime denotes a derivative with respect to the argument of the function. This is then substituted into the real part, and we obtain

$$r^3 - \alpha\frac{r}{2} + \frac{r''}{2} - \frac{A^2}{2r^3} = 0, \tag{2.31}$$

where

$$\alpha = 2n - c^2. \tag{2.32}$$

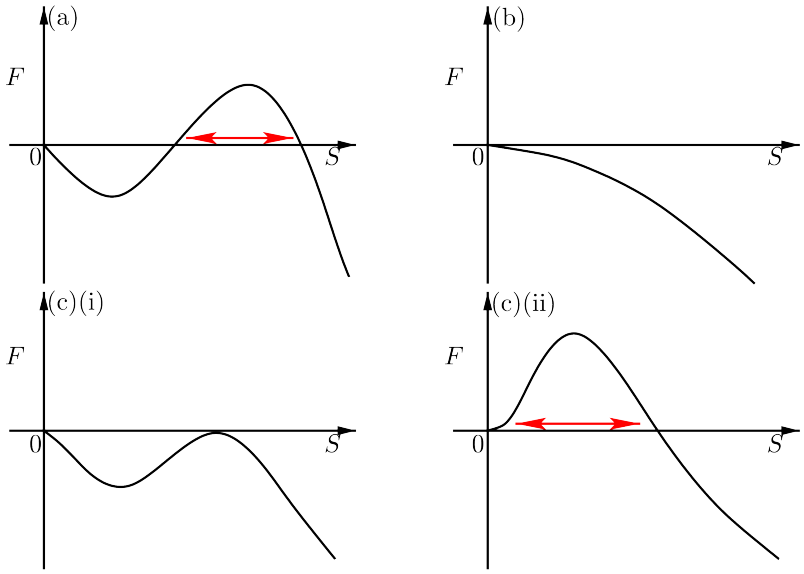

Figure 2.2: Here we see that the polynomial $F(S)$ can satisfy one of three cases: a) three single roots, b) one double root and one single root and c)one triple root

Using r' as an integrating factor we obtain, after some manipulation,

$$\begin{aligned}(S')^2 &= -4S^3 + 4\alpha S^2 + BS - 2A^2 \\ &= F(S).\end{aligned} \tag{2.33}$$

We have also used the substitution $S = r^2$, where $S \geq 0$ is the density. Equation (2.33) tells us that valid solutions to the NLSE only exist where $F(S)$ is greater than zero, as S' (and indeed S) must be real. The requirement of valid solutions for $S = 0$ fixes $A = 0$ and $F(0) = 0$. Considering the behaviour as $S \to \infty$, and knowing that $F(S)$ is a third order polynomial, we can narrow its structure down to four possible cases. These are displayed in Fig. 2.2.

We can see that scenarios (b) and (c)(i) hold no interesting solutions, as there is no range of S over which F is positive. There are, however, ranges of values of S in scenarios (a) and (c)(ii) which hold travelling wave solutions. We can see that in a) this range exits between two simple zeros of F. In (c)(ii) the range is between a double zero at $S = 0$ and a simple zero.

It can be shown (Ref. [159] and Appendix A) that if $F(S_i) = 0$, where $S_i = S(\xi_i)$, is a single zero then S has a local minimum or maximum at ξ_i. If S_i is a double zero then it can be shown that $S \to S_i$ as $\xi \to \pm\infty$. Applying this result to scenario (a) we see that if we start at a value of ξ such that $S(\xi)$ lies between the two non-zero

roots of F, as we increase or decrease ξ we will either increase or decrease S until we reach a turning point in S, where we will reverse direction and return to our starting value of S. Put simply, as we move in space or time, the amplitude u will oscillate regularly between the two values S_1 and S_2 which are the roots of F. This scenario shows us periodic regular wave-like excitations translating along the top of a bulk condensate. For completeness, further analysis of this scenario is presented in Appendix A.

In scenario (c)(ii) we see that by correctly varying ξ we will asymptotically depart from zero density, approach a maximum value in the wave's density, and then asymptotically return to zero again. This describes our classic solitary wave. A single wave form travelling at a set speed and maintaining its form indefinitely.

With $A = 0$ and setting $r, r' \to 0$ as $\xi \to \pm\infty$ in (2.33), which is true for a solitary wave profile, we determine that $B = 0$. Note that this result only holds true for $(S')^2/S \to 0$ as $\xi \to \pm\infty$ which we will justify later. Hence we find that

$$(S')^2 = S^2(\alpha - S),$$

which can be rewritten as

$$\int d\xi = \pm \int \frac{dS}{2S(\alpha - S)^{1/2}}.$$

This can be solved by the substitution $S = \alpha \mathrm{sech}^2(\alpha^{1/2}\eta)$, where η is a dummy integration argument. Normalising to the quantity $2D > 0$ such that

$$\int_{-\infty}^{\infty} |u(x,t)|^2 = 2D \tag{2.34}$$

we obtain $\alpha = D^2$ and so

$$r(x - ct) = D\mathrm{sech}\left(D\left[x - ct\right]\right). \tag{2.35}$$

If we now consider Eq. (2.30), recall that $A = 0$ and note that the second integration of this equation results in a global phase constant which can be discarded, we obtain

$$\theta(\xi) = c\xi \tag{2.36}$$

Combining this information with Eq. (3.11), now uniquely determined in terms of

the normalisation, we can determine the full phase evolution

$$u(x,t) = D\text{sech}\left[D\left(x - ct\right)\right]\exp\left[icx + i(D^2 - c^2)t/2\right]. \tag{2.37}$$

We see that our initial *ansatz* has exactly retrieved the standard J. P. Gordon soliton solution [20]. Note that this solution also satisfies $(S')^2/S \rightarrow 0$ as $\xi \rightarrow \pm\infty$, justifying our previous selection.

2.3.3 Asymptotic behaviour after collisions

Finally, we will cover the results pertaining to soliton collision and the asymptotic behaviour after collisions. We consider a train of solitons with individual amplitudes D_j (which are all positive and satisfy $\sum_j D_j = 2D$), initial phase differences ϕ_{j0} and initial positions (x_{j0}). After a sufficient amount of time the solitons are well separated and will not undergo any further collision (assuming that any solitons with exactly equal velocities are initially well separated). After this time the general solution has the form [20]

$$u(x,t) = \sum_{1}^{N} u_j(x,t) \tag{2.38}$$

where each individual soliton is given by

$$u_j(x,t) = D_j\text{sech}\left[D_j\left(x - x_j\right) + q_j\right]\exp\left[i\left(\phi_j + \Psi_j\right)\right]. \tag{2.39}$$

Here the position is given by $x_j = x_{j0} + c_j t$, and the phase is given by $\phi_j = c(x - x_j) + (D_j^2 + c_j^2)t/2 + \phi_{j0}$. The quantities of interest to us are the asymptotic shifts to position and phase, q_j and Ψ_j. These shifts are given by [20]

$$q_j + i\Psi_j = \sum_{j\neq k} \pm \ln\left[\frac{D_j + D_k + i(c_j - c_k)}{D_j - D_k + i(c_j - c_k)}\right], \tag{2.40}$$

where the plus applies for $x_k > x_j$ and the minus sign applies otherwise.

Chapter 3: Soliton splitting on narrow barriers

3.1 Introduction

The collision of a bright solitary wave with a narrow potential barrier is a good candidate for a mechanism for the creation of coherent localised condensates, much as a beamsplitter coherently splits a light beam in an optical interferometer. This mechanism has been investigated extensively in the quasi-1D, mean-field description of an atomic BEC [36–41, 48, 169–172], and sufficiently fast collisions with potential barriers have been shown to lead to the desired beamsplitting effect [40, 41].

Incomplete/bound state splitting has been considered in the context of the formation of soliton molecules [29], within a mean-field description, and also in the context of many-body quantum mechanical descriptions: in the latter it has been demonstrated that macroscopic quantum superpositions of solitary waves could be created, offering intriguing possibilities for future atom interferometry experiments [27, 28]. While in the context of atomic BECs the NLSE represents a quasi-1D condensate with tight radial trapping and either zero or very weak axial trapping (e.g., a periodic "ring" trap [173], or a waveguide or weak harmonic trap [25]), we emphasise that the equation we study here remains general and could also be used to describe similar systems in, e.g., nonlinear optics.

In this chapter we investigate a broad range of behaviours which can be exhibited by a soliton splitting event. The work is comprised of content from the first halves of Refs. [48, 49]. We first consider the case of splitting a soliton on both δ-function and Gaussian barriers in the absence of axial confinement. We discuss how the finite width of the barrier becomes relevant in the high energy regime (Sec. 3.3). We then explore the transition to the low energy regimen, wherein the kinetic and internal energies of the soliton become comparable, and some splitting events become inaccessible (Sec. 3.4). Finally, we analyse the effect of quantum fluctuations in the centre of mass position and momentum on soliton splitting. We will also present a rigorous determination of the phase shift accrued between the resulting solitons after a splitting event, based on the work presented in [40].

3.2 Physical system

We begin with the 3D N-particle mean-field energy Hamiltonian $\mathcal{H}[\psi]$ for a Bose field, defined as [81]

$$\mathcal{H}[\Psi] = \int \mathrm{d}\mathbf{r}\left[\frac{\hbar^2}{2m}|\nabla\Psi(\mathbf{r})|^2 + V_{\mathrm{ext}}(\mathbf{r})|\Psi(\mathbf{r})|^2 - \frac{2\pi N|a_s|\hbar^2}{m}|\Psi(\mathbf{r})|^4\right]. \tag{3.1}$$

Here N, m and a_s are the atom number, mass, and (negative) s-wave scattering length respectively. A delta function contact potential is assumed. Further details of the system this Hamiltonian describes are available in Section 1.3.1. The wave function, Ψ, is normalised to 1. The potential $V_{\mathrm{ext}}(\mathbf{r})$ is comprised of both the trapping potentials and any external potentials used to construct narrow barriers used for splitting the soliton. We model this potential as

$$V_{\mathrm{ext}}(\mathbf{r}) = E_{\mathrm{B}}e^{-2x^2/x_r^2} + \frac{m}{2}\left[\omega_{\mathrm{T}}^2x^2 + \omega_r\left(y^2+z^2\right)\right]. \tag{3.2}$$

The first term describes the narrow splitting barrier and can be generated by an off-resonant Gaussian light sheet [34] perpendicular to the x direction with $1/e^2$ radius x_r in the x direction, and with peak beam strength E_{B}. The second term denotes a standard magnetic harmonic confinement which we take to be a cylindrically symmetric waveguide; such a configuration is approximately achieved in an atomic waveguide trap [34].

By increasing the radial trapping we can reach a quasi-1D regime, as defined in detail in Ref. [25] and Section 1.4.2, where the radial trapping is tight but remains 3D [$a_s \ll (\hbar/m\omega_r)^{1/2}$]. In this regime we can separate the radial and axial dynamics with the *ansatz* $\Psi(\mathbf{r}) = \Psi_{1\mathrm{D}}(x)(m\omega_r/\pi\hbar)^{1/2}\exp\left(-m\omega_r[y^2+z^2]/2\hbar\right)$. After factoring out global phases associated with the radial harmonic ground state energies, this yields both the quasi-1D classical field Hamiltonian [81],

$$\mathcal{H}_{1\mathrm{D}}[\Psi_{1\mathrm{D}}] = \int \mathrm{d}x\left[\frac{\hbar^2}{2m}\left|\frac{\partial}{\partial x}\Psi_{1\mathrm{D}}(x)\right|^2 + V_{\mathrm{ext}}(x)|\Psi_{1\mathrm{D}}(x)|^2 - \frac{gN}{2}|\Psi_{1\mathrm{D}}(x)|^4\right], \tag{3.3}$$

and its associated quasi-1D GPE [81]

$$i\hbar\frac{\partial\Psi_{1\mathrm{D}}(x)}{\partial t} = \left[-\frac{\hbar^2}{2m}\frac{\partial^2}{\partial x^2} + V_{\mathrm{ext}}(x) - g_{1\mathrm{D}}N\left|\Psi_{1\mathrm{D}}(x)\right|^2\right]\Psi_{1\mathrm{D}}(x). \tag{3.4}$$

The non-linearity is quantified by $g_{1\mathrm{D}} = 2\hbar\omega_r|a_s|$. If we take $V_{\mathrm{ext}} = 0$ then this equation reduces to the NLSE.

Working in soliton units yields the dimensionless, quasi-1D GPE[1]

$$i\frac{\partial\psi(x)}{\partial t} = \left[-\frac{1}{2}\frac{\partial^2}{\partial x^2} + \frac{q}{\sigma_{\rm b}\sqrt{2\pi}}e^{-x^2/2\sigma_{\rm b}^2} + \frac{\omega_x^2 x^2}{2} - |\psi(x)|^2 \right]\psi(x), \tag{3.5}$$

where the dimensionless wave function is $\psi = \hbar\Psi_{\rm 1D}/\sqrt{mgN}$, the barrier width is characterised by $\sigma_{\rm b}$ (the dimensionless form of half the $1/e^2$ radius) and the barrier strength is given by

$$q = \sqrt{\frac{\pi}{2}}\frac{E_{\rm B}x_r}{gN}. \tag{3.6}$$

Equation (3.5) is equivalent to Eq. (1.63) with an extra externally applied splitting potential.

3.3 Classical soliton splitting on narrow barriers

3.3.1 Splitting on δ-function barriers

In this section we examine the splitting of a single bright soliton on a δ-function barrier in the absence of harmonic confinement [Eq. (3.5) with $\omega_x = 0$]. The assumption of a δ-function barrier facilitates an analytic treatment and is valid for narrow barriers with $\sigma_{\rm b} \to 0$. A detailed analytic treatment of single-bright-soliton splitting on such a barrier is given by Holmer, Marzuola and Zworski in Ref. [40]. Here we briefly restate two key results of Ref. [40] within our own notation.

Firstly, the transmission coefficient for a fast-moving bright soliton splitting on a δ-function barrier is approximately equal to the transmission coefficient for plane waves incident on an identical δ-function barrier in linear quantum mechanics, $T_q(v)$, given by

$$T_q(v) = |t_q(v)|^2 = \frac{v^2}{v^2+q^2} = \frac{1}{1+\alpha^2}. \tag{3.7}$$

Here, $t_q(v)$ is the transmission amplitude associated with a δ-function barrier in linear quantum mechanics, and the soliton velocity v plays a role analogous to the wavenumber of the incident wave. The transmission and reflection amplitudes $t_q(v)$ and $r_q(v)$, are defined as

$$t_q(v) = \frac{iv}{iv-q} \qquad \text{and} \qquad r_q(v) = \frac{q}{iv-q}. \tag{3.8}$$

[1] It should be noted that in the very low N limit this rescaling takes a slightly different form, with N replaced by $N-1$. This rescaling is used in Ref. [153]

The quantity α characterises the transmission in the linear case, and hence the transmission of bright solitons in the high velocity limit. The exact relation between $T_q(v)$ and the actual transmission coefficient for the incident bright soliton,

$$T_q^s(v) = \lim_{t\to\infty} \int_0^\infty |\psi(x,t)|^2 dx, \tag{3.9}$$

is determined in Ref. [40] to be

$$\begin{aligned} T_q^s(v) &= \frac{v^2}{v^2+q^2} + O(v^{1-3\eta/2}) \\ &= T_q(v) + O(v^{1-3\eta/2}), \qquad \text{as } v \to \infty, \end{aligned} \tag{3.10}$$

provided that the initial offset is $x_0 \leq -v^{1-\eta}$ and the transmission rate

$$\alpha = \frac{q}{v} \tag{3.11}$$

is fixed. Here, η is a parameter linked to the duration for which the soliton interacts with the barrier, and must satisfy $2/3 < \eta < 1$. The brevity of this duration for a fast-moving bright soliton, which allows one to treat the splitting as a *linear* process, is fundamental to the proof of the above result [40]. The error term in Eq. (3.10) is minimized for brief collisions ($\eta \to 1$), in which case it decays with increasing velocity as $v^{-1/2}$.

Secondly, it is also determined in Ref. [40] that the outgoing waves resulting from splitting a bright soliton on a δ-function barrier are composed of either one, or two, bright solitons, and a time-decaying radiation term. This is significant, as previously the transmitted and reflected waves were considered to be only 'soliton-like' [39, 41]. The resulting bright solitons are described, for high velocity, by

$$\psi(x,t) = \psi_T(x,t) + \psi_R(x,t) + O\left([t-|x_0|/v]^{-1/2}\right) + O(v^{1-3\eta/2}) \tag{3.12}$$

where [40]

$$\begin{aligned} \psi_T(x,t) &= e^{i\vartheta_T} e^{i(xv+[A_T^2-v^2]t/2)} A_T \mathrm{sech}(A_T[x-x_0-tv]), \\ \psi_R(x,t) &= e^{i\vartheta_R} e^{i(-xv+[A_R^2-v^2]t/2)} A_R \mathrm{sech}(A_R[x+x_0+tv]). \end{aligned}$$

The amplitudes of the transmitted and reflected solitons are given by

$$A_T = \max(0, 2|t_q(v)| - 1) \text{ and } A_R = \max(0, 2|r_q(v)| - 1); \tag{3.13}$$

in the case that A_T (A_R) is equal to zero, the transmitted (reflected) outgoing wave does not contain a soliton, but only radiation. More generally, the inequalities $A_T < T_q^s(v)$ and $A_R < 1 - T_q^s(v)$ hold. The exact forms of $\vartheta_{R/T}$ will be given later.

3.3.2 Splitting on Gaussian barriers

We now give numerical analysis of the bright soliton splitting process at a Gaussian barrier, again in the absence of axial confinement ($\omega_x = 0$). Our numerical simulations use a Fourier pseudo-spectral split-step method with a periodic grid (see Appendix B). We ensure that grid size and spacing are chosen such that the bright solitons are well separated and the effects of the periodicity are negligible.

Our initial condition takes the form

$$\psi_0 = \frac{1}{2}\mathrm{sech}\left(\frac{x - x_0}{2}\right)e^{ivx}, \tag{3.14}$$

where $x_0 < 0$. Figure 3.1(a) shows the transmission coefficient $T_q^s(v)$ obtained from numerical simulations of a single bright soliton splitting on a Gaussian barrier with width $\sigma = 0.1$, and with $\alpha = q/v = 0.6$, 0.8, 1.0, 1.2, and 1.4. In our numerics we define $T_q^s(v)$ by the integral of $\psi(x, t_1)$ over the positive x domain,

$$T_q^s(v) = \int_0^\infty |\psi(x, t_1)|^2 dx. \tag{3.15}$$

Here $t_1 = 2|x_0|/v$, such that at this time an unimpeded bright soliton would have reached the point $x = +|x_0|$; at this time the outgoing waves are well-separated. The results are comparable to the δ-function barrier case explored in Ref. [40] and the previous section.

Figure 3.1(a) shows that as α increases so does the discrepancy between the asymptotic δ-function limit and $T_q^s(v)$. This can be understood by considering how the strength of the barrier compares to the (particle-like) kinetic energy of the soliton $v^2/2$. In the region where the strength of the barrier is greater than the soliton's kinetic energy the wave function decays, reducing transmission. By equating these two values,

$$\frac{v^2}{2} = \frac{q}{\sigma\sqrt{2\pi}}e^{-x_d/2\sigma^2}, \tag{3.16}$$

we determine that the distance over which the wave function decays, x_d, is described

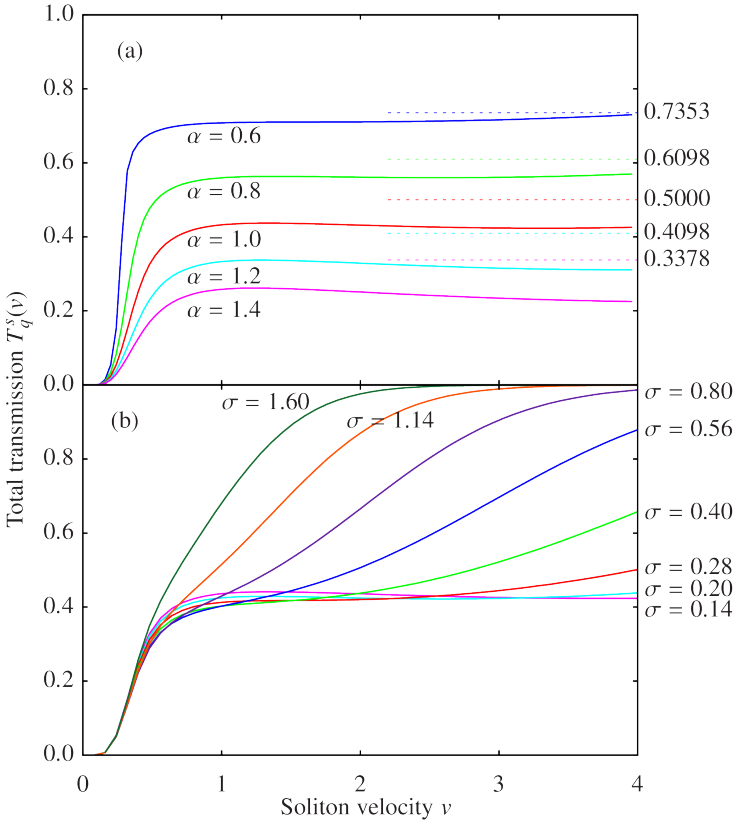

Figure 3.1: (a) Plot of numerically obtained bright soliton transmission, $T_q^s(v)$, as a function of velocity v for a range of fixed $\alpha = q/v$ and a narrow Gaussian barrier with width $\sigma = 0.1$. Dashed lines show the transmission through a δ-function in the linear regime for the same range of α. (b) Numerically obtained bright soliton transmission for $\alpha = 1$ and with a range of barrier widths σ. Reproduced from Ref. [48].

by

$$x_d^2 = 2\sigma^2 \ln\left(\sqrt{\frac{2}{\pi}}\frac{\alpha}{|v|\sigma}\right). \tag{3.17}$$

It is clear that, for a given v and σ, as we increase α (by increasing q) we increase x_d. This is inconsistent with the assumption of a brief barrier-soliton interaction period, which is required in the delta function case of soliton splitting. This inconsistency causes an increase in the attenuation of the wave function, reducing transmission.

We show the computed dependence of the transmission on the barrier width σ in Fig. 3.1(b). These computations were carried out with $\alpha = 1$. For wider barriers or in the higher velocity range, where the peak height of the potential is less than the (particle-like) kinetic energy $v^2/2$ of the incident soliton, the amount of

transmission is greatly increased. This illustrates the classical transmission regime where the soliton simply passes through the potential, and, for the Gaussian barriers considered, boils down to an argument that we must have

$$\frac{v^2}{2} \ll \frac{q}{\sigma\sqrt{2\pi}} \Rightarrow |v| \ll \frac{2|\alpha|}{\sigma\sqrt{2\pi}} \tag{3.18}$$

to be definitely out of the classical transmission regime. From Eq. (3.18) it is apparent that for satisfactorily large v we will always enter the classical transmission regime for any given finite Gaussian barrier. This regime cannot be retrieved in the δ-function case.

The comparison to the δ-function case is valid in the quantum transmission regime, where the velocity is low enough (for a given q, σ) that the soliton cannot classically pass through the barrier and must tunnel through instead. For example, this is true when $0.5 \lesssim v \lesssim 2$ and $\sigma \leq 0.28$ [see Fig. 3.1]. Within the quantum transmission regime [Eq. (3.18)] the δ-function limit of 0.5 is reached (from below) by reducing σ. This allows for larger values of v, as is consistent with Holmer and Marzuola's work in [40] where results are general for any $v \gtrsim 1$ (which is the high velocity regime).

Figure 3.1(b) shows that the transmission approaches the analytic prediction for a δ-function barrier as the barrier width σ tends to zero. This confirms that the analytic expressions given in Ref. [40] and the previous section for the δ-function barrier can be quantitatively useful for realistic Gaussian barrier widths. For example, Fig. 3.1(b) indicates the analytic prediction is reasonably quantitatively accurate for $\sigma \leq 0.28$ in soliton units. For a condensate of ^{85}Rb and using typical experimental parameters of $N \sim 6 \times 10^3$ atoms, $a_s \sim 5a_0$ (the Bohr radius) and $\omega_r \sim 17$Hz this translates to a splitting beam with a full width at half maximum of $\sim 9\ \mu$m. These parameters are consistent with the experimental setup in [10]. For a similarly sized condensate of ^{7}Li atoms tuned to a similar scattering length this width becomes $\sim 2\ \mu$m. This parameter regime is consistent with [8] apart from the radial trapping frequency, which we reduced from $2\pi \times 710$Hz to $2\pi \times 200$Hz.

3.4 Low energy soliton splitting

3.4.1 Overview

In this section we probe the transition from low- to high-energy soliton splitting. We quantify the energy by the velocity of the soliton at the point of collision with the barrier, denoted as v for an untrapped system, where the velocity is brought about by an imprinted phase on the initial condition; or v_0 for the axially trapped system, where the velocity is a result of the axial trapping ω_x being greater than zero and an initial offset x_0 in the initial condition. This offset separates the soliton from the point where the soliton is split by the barrier at $x = 0$.

We take $v, v_0 \gtrsim 1.0$ to be the high energy regime and $v, v_0 \lesssim 0.25$ to be the low energy regime [92]. As such, the transitional energy regime lies within the $0.25 \leq v, v_0 \leq 1$ velocity range. We will justify the lower bound of this regime by considering classical descriptions of the kinetic and ground state energies of the system. We will also show that these arguments describe a process which is analogous to the quantum mechanical transition from product state wave-functions (where, after scattering the transmitted/reflected portions of the wave function can range continuously between zero and full transmission/reflection) to bimodal systems (where the soliton is either reflected by or transmitted through the barrier, but never split)[2].

3.4.2 Classical analysis of the transitional regime

Hamiltonian analysis of the transitional regime

We explain the transition between high and low energy dynamics by comparing the incoming collisional kinetic energy E_{K} and the energy required to split the soliton E_{S}. Firstly, rescaling the quasi-1D Hamiltonian [Eq. (3.3)] in to soliton units with $\omega_{\mathrm{T}} = 0$ gives

$$\mathrm{H}_{1\mathrm{D}}[\psi] = \int \mathrm{d}x \left[\frac{1}{2} \left| \frac{\partial}{\partial x} \psi(x) \right|^2 - \frac{1}{2} |\psi(x)|^4 \right]. \tag{3.19}$$

We then substitute the 1D soliton solution, Eq. (3.14) into our Hamiltonian, with $v = 0$, and obtain both the per-particle soliton ground state energy ($\mathrm{H}_{1\mathrm{D}}[\psi_0] = -1/24$) and N-particle soliton ground state energy [$E_{\mathrm{G}}(N) = -N/24$]. We then

[2] It should be noted that even in the high energy regime we cannot make a soliton of arbitrary size by simply scattering a larger soliton off a barrier. The scattered portion of the wavefunction may be too small to form a soliton and must be considered radiation [40].

consider an n particle soliton which is spatially well separated from the rest of the condensate and any potentials. Failure to satisfy this separation assumption may result in a bound state, and further contributions to the ground state energy will arise. The effects of such bound states will be discussed later. Assuming that the whole condensate contains a total of N particles we see that the spatially separated soliton's contribution to the total energy is

$$E_{\mathrm{G}}(n) = -\frac{n}{24}\left(\frac{n}{N}\right)^2. \tag{3.20}$$

We reach this conclusion by rescaling the n-particle soliton ground state energy $E_{\mathrm{G}}(n)$ into N particle soliton units. This is equivalent to multiplying by $(n/N)^2$. By constructing the energy difference E_{S} we can easily see that the energy required to split the soliton is

$$\begin{aligned} E_{\mathrm{S}} &= E_{\mathrm{G}}(N-n) + E_{\mathrm{G}}(n) - E_{\mathrm{G}}(N), \\ &= 3|E_{\mathrm{G}}(N)|\left(1-\frac{n}{N}\right)\frac{n}{N}. \end{aligned} \tag{3.21}$$

We can now re-cast this result in terms of the transmission, T_+:

$$T_+ = \int_0^\infty |\psi|^2 \mathrm{d}x = \frac{n}{N} \tag{3.22}$$

yielding

$$E_{\mathrm{S}} = \frac{1}{8} T_+ \left(1 - T_+\right) N. \tag{3.23}$$

Next, we describe the classical particle energy of an N-particle soliton moving at velocity v:

$$E_{\mathrm{K}} = \frac{v^2 N}{2}. \tag{3.24}$$

We can now see that, for splitting to occur, we must satisfy $E_{\mathrm{K}} > E_{\mathrm{S}}$ and so

$$|v| > \frac{1}{2}\sqrt{T_+\left(1-T_+\right)}. \tag{3.25}$$

This inequality can be used to characterise the transition to the low energy regime in that parameters which do not satisfy it are only available in the transitional to low energy regime. If we consider the functional form of our inequality we see that $\sqrt{T_+\left(1-T_+\right)}$ is maximal for $T_+ = 0.5$, at which value we have $|v| > 0.25$. As such, the first state to become inaccessible is the equal splitting case, which cannot be accessed for $|v| < 0.25$. Equivalently, we must satisfy $E_{\mathrm{K}}/E_{\mathrm{S}} > 0.75$ [Eq. (3.21)].

This is consistent with results described in Ref. [92].

As noted above, splitting the soliton reduces the amount of kinetic energy available to the solitons. This was numerically investigated in Ref. [92]. In the high energy regime, this reduction is negligible and the solitons are capable of becoming well separated from the barrier, and one another, after the split occurs. At lower energies this is not always the case. As less and less energy is available to the resulting solitons their outgoing velocities are notably reduced, and eventually the solitons become trapped at the barrier. The effect of the harmonic trap enhances this effect, as the outgoing velocity determines the maximal separation which the resulting solitons can achieve. This phenomenon is shown in Fig. 3.2 and will be discussed in the next section.

Numerical analysis of the transitional regime

We numerically verify these results by evolving the initial condition described by Eq. (3.14) according to the dynamics of Eq. (3.5). We perform two types of evolution. For the first type we set $\omega_x = 0$ and perform integrations over a range of v and q. These calculations allow us to consider the behaviour of the untrapped, true, soliton to which the above analytic results apply exactly. Fig. 3.2(a-c) shows the results of these simulations. For the second type of simulation we set the initial velocity $v = 0$ and integrate over a range of ω_x and q. By keeping the initial offset constant at $x_0 = -L/4$, where the numerical algorithm has spatial domain $-L/2 < x \leq L/2$, we are able to use ω_x to select a collisional velocity $v_0 = \omega_x x_0$. This allows us to more accurately describe the behaviour we would see in an experiment where the soliton is accelerated by an axial harmonic trap. Fig. 3.2(d-f) shows the results of these equations.

For all simulations the barrier is situated at the trap minimum (specifically $x = 0$) and we set the barrier width to $\sigma_b = 0.2$. Barrier potentials of finite width/height have some limitations in the extremely high velocity regime, in that if the peak energy of the barrier is not notably higher than the kinetic energy of the soliton then the soliton classically passes over the barrier and no splitting occurs [48] . This restricts the width of the barrier in a given energy regime by requiring that the barrier be narrow enough to constitute a quickly varying potential when compared to the incoming velocity of the soliton. The energy regimes we consider in the current work are compatible with a barrier width of $\sigma_b \lesssim 0.2$. A broader discussion of the effect of finite width (for a Rosen–Morse i.e. sech^2 potential barrier) is presented in Ref. [169].

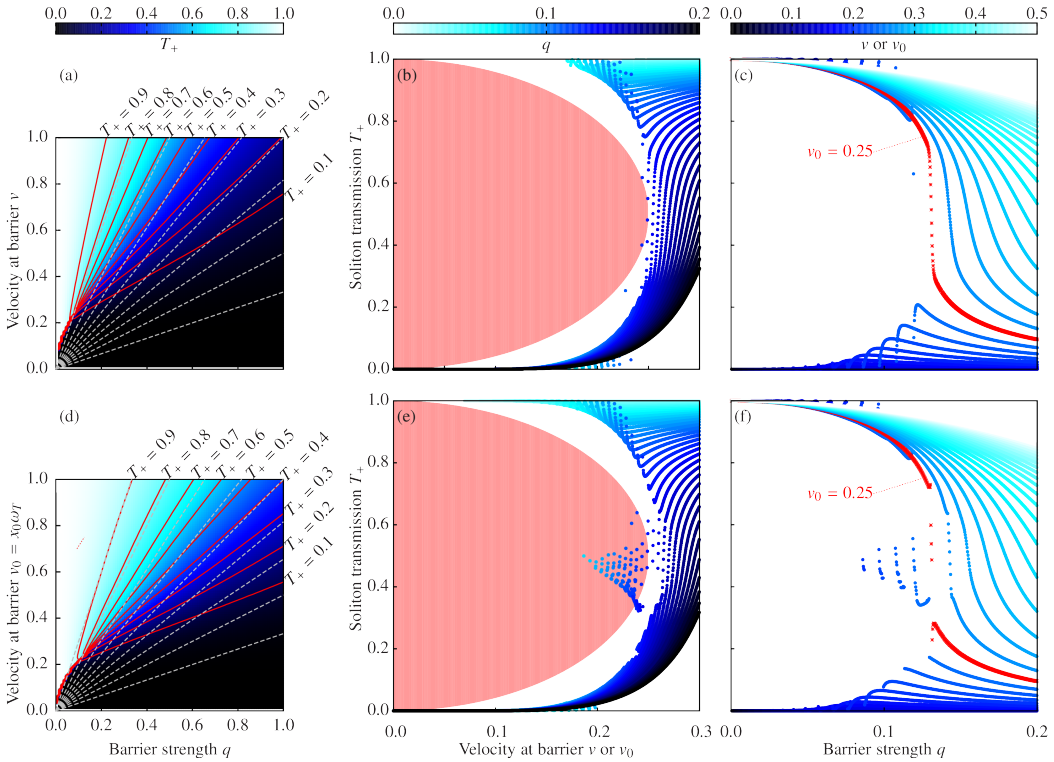

Figure 3.2: Numerical results of splitting a soliton travelling at velocity v-(a–c) or v_0-(d–f) at a Gaussian barrier of strength q and width $\sigma = 0.2$. (a,d) Colormaps of transmission as a function of q and v or v_0. The solid (red) curves are iso-lines of constant transmission T_+ obtained from the numerics, while the dashed (gray) curves are theoretical predictions of transmission T_q^s in the linear case over the same range. (b,e) Curves of transmission as a function of collisional velocity v or v_0 for various barrier strength q. The shaded (red) region shows energetically disallowed splitting events. (c,f) Curves of transmission as a function of barrier strength q for various values of v or v_0. The labelled (red) curve, for which $v, v_0 = 0.25$ indicates the classical, untrapped lower energy bound on the region where a continuous range of transmission is accessible. Reproduced from Ref. [49].

Figure 3.2(a) displays a broad scan of the q, v parameter space. At higher velocities ($v > 0.25$) we see a continuous range of transmissions is accessible. At lower velocities this is not the case, and for $v \lesssim 0.1$ we see that we are effectively left with only full transmission and full reflection as accessible final states.

We have displayed two sets of curves of constant transmission on Fig. 3.2(a): solid (red) and dashed (grey). The solid (red) curves are iso-lines of constant transmission $T_+ = 0.1, 0.2, \ldots 1.0$ taken from the colormap itself. At higher values of v

these curves are well separated, illustrating that we can access the full range of transmissions by selecting q and v accordingly. As v decreases these curves begin to converge. The convergence of iso-curves signifies that the splitting state associated with the curves has become disallowed.

We derived the second set of curves in Fig. 3.2, the dashed (grey) curves, from Eq. (3.7). This illustrates that in the high energy regime the transmission is determined solely by the ratio $\alpha = q/v$, and we predict the dashed (grey) curves of constant transmission which take the form

$$v = \left(\frac{T_q^s}{1 - T_q^s}\right)^{1/2} q. \tag{3.26}$$

Here we have adopted Holmer's T_q^s notation [40] to denote the limiting case of a high energy mean-field soliton colliding with a δ-function barrier. In Fig. 3.2 we display the curves for $T_q^s = 0.1, 0.2, \ldots 1.0$. It should be noted that these curves are also the transmission rates of plane-waves though a δ-function barrier in the linear Schrödinger equation, where the energy is expressed in terms of the velocity instead of the wavenumber.

Comparing the two sets of curves, we see that the system does, indeed, retrieve a more linear behaviour in the high energy regime where the effect of kinetic energy is greater than that of the non-linear energy. While the curves do not quantitatively align in the range displayed, they at least share a qualitative agreement. At lower energies, where we see bunching/convergence of the red iso-curves which illustrates disallowed states, the transmission behavior departs from being comparable to the linear system and becomes truly non-linear.

In Fig. 3.2(b) we display curves of transmission as a function of velocity for a range of values of q. The shaded (red) region is the region of T_+, v combinations disallowed under inequality Eq. (3.25). In the high kinetic energy regime these curves increase monotonically, but at low kinetic energies this ceases to be true [92, 169–171]. We see that here (in the absence of an axial harmonic trap) the disallowed region is quite strict, with no substantial violation of Eq. (3.25). Indeed, Eq. (3.25) is generally found to be more strict than the numerical result, as seen by the empty gaps between the disallowed region and the transmission curves.

In Fig. 3.2(c), the last part that pertains to the axially untrapped case, we display curves of transmission as a function of barrier strength for a range of collisional/initial velocities. The labelled (red) curve, for which $v = 0.25$, shows the

bound below which there is never enough kinetic energy to access all splitting events. We see that all curves $T_+(q;v)$ are discontinuous for $v \leq 0.25$, although the discontinuous region is narrower for higher v, and is instantaneous for the $v = 0.25$ case.

Figure 3.2(d–f) are the harmonically trapped counterparts of the figures described above, as we described at the beginning of this subsection. The behaviour is broadly the same, however there are some specific qualitative and quantitative differences.

In terms of qualitative differences, we see in Figs. 3.2(e) and (f) that there exists a class of solution which appears to access disallowed outcomes, shown by points lying within the shaded (red) region of the plot. Upon closer inspection we determined these outcomes to be bound state solutions [169]. The energetic arguments leading to Eq. (3.25) suppose that the solitons are, after splitting, well separated. If this is not the case then we can access a bound state solution. In this event, the kinetic energy shortfall (the deficit of energy required to fully split the soliton) is made up for by the bound-state interaction energy which is gained from the overlap, and attraction, between the resulting solitons. This effect can be greatly enhanced in the harmonically trapped system, where an insufficient kinetic energy after splitting means that the solitons cannot fully separate in the trap, necessitating a bound state.

Quantitatively we see that the value of v_0 (the velocity of the soliton at the bottom of the trap in the absence of a splitting potential, which we take to be the collisional velocity) must be slightly higher than its untrapped counterpart v in order to access a continuous range of splitting outcomes. This is because the soliton begins to interact with the barrier slightly before it reaches the bottom of the trap at $x = 0$, and so the collisional velocity is, in fact, slightly lower than v_0. This is shown by: the gap between the transmission curves and the disallowed region being wider in Fig. 3.2(e) than in Fig. 3.2(b); and the labelled (red) transmission curve in Fig. 3.2(f) having a substantially wider discontinuous region than its counterpart in Fig. 3.2(c), where the GPE limit of $N \to \infty$ is taken.

3.4.3 Classical indicators of the quantum regime

The behaviour we observe here, which describes an energy bound below which the possibility for splitting to occur is progressively curtailed, mirrors behaviour which leads to the generation of entangled states [174] in the purely quantum mechanical treatment. Indeed, it has been shown that entangled states in the fully quantum mechanical regime imply the discontinuities we see here [92]. There is also evidence

for the reverse implication [174], and so it is conceivable that these behaviours are equivalent to the extent that transmission discontinuities in the mean-field treatment delimit the regime where mesoscopic Bell states would exist in the fully quantum mechanical treatment, despite these states not being present in the GPE formalism.

3.4.4 Analysis of centre-of-mass uncertainty

We now address this high- to low-energy transitional regime by considering how quantum uncertainty impacts the dynamics of the system. The transmission through the barrier is determined by the velocity of the soliton at the point of collision. In the harmonically trapped system, fluctuations in the initial COM position and momentum will affect this velocity and so affect the transmission. We consider these uncertainties in the harmonically trapped system only, which presents a better defined situation than the untrapped, periodic regime when considering quantum fluctuations of the COM. In order to delimit a regime where the position and momentum uncertainty of the soliton affects the outcome of a splitting event, we must develop a formalism which allows us to introduce this uncertainty into our system.

First we consider a full many body treatment of our 1D N-particle system. We can write the first quantized form of the Hamiltonian as [175]

$$\hat{H}(\boldsymbol{x}) = \sum_{k=1}^{N}\left(-\frac{\hbar^2}{2m}\frac{\partial^2}{\partial x_k^2} + \frac{m\omega_{\mathrm{T}}^2 x_k^2}{2}\right) - g_{1\mathrm{D}}\sum_{k=2}^{N}\sum_{j=1}^{k-1}\delta(x_k - x_j). \tag{3.27}$$

In this notation, $\boldsymbol{x}$ denotes the vector of the positions of all N particles, $\{x_1, x_2, .., x_N\}$, and all quantities are expressed in their fully dimensional form.

Moving to Jacobi coordinates we can show that the COM dynamics and the internal degrees of freedom separate [153] by expressing the Hamiltonian as $H = H_{\mathrm{C}} + H_{\mathrm{R}}$, where

$$H_{\mathrm{C}}(x_{\mathrm{C}}) = -\frac{\hbar^2}{2Nm}\frac{\partial^2}{\partial x_{\mathrm{C}}^2} + \frac{Nm\omega_{\mathrm{T}}^2 x_{\mathrm{C}}^2}{2} \tag{3.28}$$

is simply the single particle Hamiltonian for a particle of mass Nm at position x_{C} – the COM coordinate. H_{R} describes the residual internal dynamics.

The dimensional wave function for the COM, ψ_{C}, is then given by

$$\psi_{\mathrm{C}}(x_{\mathrm{C}}) = \left(\frac{1}{\tilde{s}_x\sqrt{2\pi}}\right)^{1/2}\exp\left(-\frac{x_{\mathrm{C}}^2}{4\tilde{s}_x{}^2}\right). \tag{3.29}$$

which is simply the 1D wave function of a single particle of mass mN in an axial harmonic trap of frequency ω_{T} normalized to 1. We can interpret $|\psi_{\mathrm{C}}|^2$ as the probability density function for the normally distributed random variable x_{C} such that the expected value is $\langle x_{\mathrm{C}} \rangle = 0$ and the variance (or the position uncertainty of our soliton) is given by $\langle x_{\mathrm{C}}^2 \rangle = \tilde{s_x}^2 = 2mN\omega_{\mathrm{T}}/\hbar$.

For our purposes, it is better to consider velocity uncertainty than it is to consider momentum uncertainty. Regardless, we must express our COM wave function in momentum space to obtain the momentum/velocity uncertainty. We now use standard result for the Fourier transform of a Gaussian, giving us the Fourier space wave function

$$\phi_{\mathrm{C}}(k_{\mathrm{C}}) = \left(\frac{1}{\tilde{s_k}\sqrt{2\pi}}\right)^{1/2} \exp\left(-\frac{k_{\mathrm{C}}^2}{4\tilde{s_k}^2}\right). \tag{3.30}$$

where the wavenumber variance is $\langle k_{\mathrm{C}}^2 \rangle = \tilde{s_k}^2 = 1/4\tilde{s_x}^2 = mN\omega_{\mathrm{T}}/2\hbar$. We can now determine the momentum uncertainty ($\hbar s_k$) and so the velocity uncertainty $\tilde{s_v} = (\hbar/mN)\tilde{s_k}$.

Rescaling the position and velocity uncertainties into dimensionless quantities, we now have

$$\begin{aligned} s_x &= (1/2N\omega_x)^{1/2}, \\ s_v &= (\omega_x/2N)^{1/2}. \end{aligned} \tag{3.31}$$

These uncertainties are consistent with the GPE formalism in that as $N \to \infty$ they both disappear. In this limit, the full wave function ψ gives the actual density profile, rather than a probability density function.

We now consider this system with an initial condition described by a ground state soliton at position x_0. If we consider a single observation of the quantum system, we see that the soliton's initial position and velocity are given by $x_0 + x_{\mathrm{f}}$ and v_{f}, where x_{f} and v_{f} denote the quantum fluctuations and are, therefore, normally distributed random variables with mean 0 and standard deviations s_x and s_v respectively. By classically evolving these initial conditions (according to Eq. (3.5)) we can apply previous results to state that the final transmission will depend on the fluctuating collisional velocity v_{b}, where $v_{\mathrm{b}} = [\omega_x^2 (x_0 + x_{\mathrm{f}})^2 + v_{\mathrm{f}}^2]^{1/2}$.

By re-writing this velocity as $v_{\mathrm{b}} = [\omega_{\mathrm{f}}^2 + v_{\mathrm{f}}^2]^{1/2}$, where $\omega_{\mathrm{f}} = \omega_x(x_0 + x_{\mathrm{f}})$, we can see that v_{b} is essentially the length of a vector comprised of two normally distributed random variables: $\omega_{\mathrm{f}} \sim \mathrm{N}(\omega_x x_0, s_v^2)$ and $v_{\mathrm{f}} \sim \mathrm{N}(0, s_v^2)$. Note that both variables are

Gaussian and have the same variance. As such, we can treat the collisional velocity v_b as a Rician distributed random variable $v_\mathrm{b} \sim \mathrm{R}(\omega_x x_0, s_v)$, and so is described (in terms of the Laguerre polynomials of order $1/2$, $\mathrm{L}_{1/2}$ [176]) by mean and variance $\mu_{v_\mathrm{b}}, \sigma_{v_\mathrm{b}}$ defined as

$$\mu_{v_\mathrm{b}} = \mathrm{E}\left[v_\mathrm{b}\right] = s_v \sqrt{\frac{\pi}{2}} \mathrm{L}_{1/2}\left(\frac{-(\omega_x x_0)^2}{2s_v^2}\right), \tag{3.32}$$

$$\sigma^2_{v_\mathrm{b}} = \mathrm{Var}\left[v_\mathrm{b}\right] = 2s_v^2 + (\omega_x x_0)^2 - \mu^2_{v_\mathrm{b}}. \tag{3.33}$$

3.4.5 Numerical analysis of the effects of quantum effects in the transitional regime

Overview of the method

We now wish to characterise the effect of COM and collision velocity uncertainties on the soliton's transmission through the barrier after being accelerated by the harmonic trap (T_+). To determine the effect of these quantum fluctuations we perform a Monte-Carlo analysis, where we numerically evolve the GPE [Eq. (3.5)] with fluctuations in the initial COM position and momentum. This procedure uses the COM truncated Wigner approximation (TWA), as used in Ref. [174] to describe the behavior of mesoscopic quantum superpositions. The COM TWA was shown to agree well with the effective potential approach of Ref. [27], demonstrating the validity of this method for describing quantum fluctuations in bright soliton systems. Note the related work investigating bright solitons using the TWA in Refs. [30, 177].

To characterise the effects of quantum fluctuations, we performed numerical calculations of soliton splitting for varying particle numbers and trap frequencies. We perform these calculations over the same range of velocities as that explored in Section 3.4.2, allowing for comparisons over the same energetic regime.

Given that this is the velocity range of interest we must select a range of values for the particle number N such that the relevant uncertainties [Eq. (3.31)] generate fluctuations which are significant relative to the grid spacing in the numerical algorithm. With 4096 spatial grid points over a $-20\pi < x < 20\pi$ domain we have a grid spacing $\Delta x \approx 0.031$. If we now require that $s_x/\Delta x > 10$ (giving twenty grid points within one standard deviation of the spatial mean), we are limited to $N \lesssim 166$. We will distribute N logarithmically over this range (taking powers of 2) and so we consider $N = 16, 32, 64, 128$.

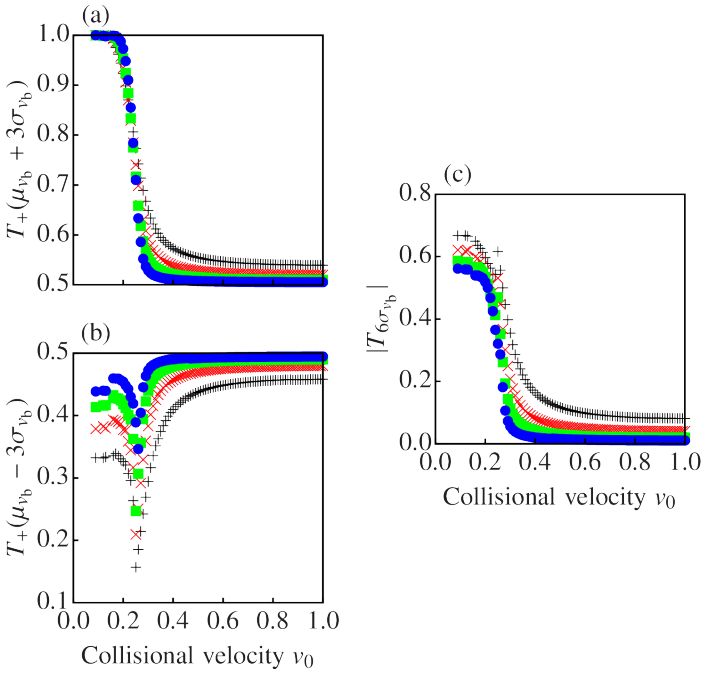

Figure 3.3: Results of numerical integrations of the GPE illustrating the sensitivity of equal splitting to extreme quantum fluctuation for various particle numbers. The transmission after extreme positive (negative) energy quantum fluctuations are displayed in panel (a) (panel (b)). The number fluctuation measure $T_{6\sigma_{v_b}}$ [Eq. (3.34)] is plotted in (c). For all plots we show $N = 16$ (+), 32 (×), 64 (■) and 128 (●). Reproduced from Ref. [49].

It should be noted that this limit on N was determined with $v_0 = 1$, and so in general there are significantly more than twenty grid points within one standard deviation of the mean. For example, with $N = 16$ and $v_0 = 0.1$ there are over two hundred grid points within one standard deviation of the mean.

In both sections, for each value of v_0 a value of the barrier strength q was selected such that the soliton would be split equally in the absence of quantum fluctuations on the initial condition. The barrier's width was $\sigma_b = 0.2$ for all runs.

Transmission sensitivity to quantum fluctuations

We first characterise the sensitivity of the equal splitting case to extreme quantum fluctuations over a continuous range of v_0. For v_0 in the range $0 < v_0 \leq 1$ the barrier strength q was found such that $T_+(v_0) = 1/2$. The simulation was then run twice more, replacing the initial position x_0 with $x_\pm = (\mu_{v_b} \pm 3\sigma_{v_b})/\omega_x$ [Fig. 3.3(a,b)]. This selection achieves collisional velocities at the barrier of $\mu_{v_b} \pm 3\sigma_{v_b}$. The transmis-

sions associated with these initial conditions $[T_+(\mu_{v_b} \pm 3\sigma_{v_b})]$ illustrate the effects of extreme quantum fluctuations. These velocities represent extreme cases of quantum uncertainties adding/removing energy from the system, and so the $+/-$ cases correspond to extreme positive/negative energy quantum fluctuations in the system, and will be referred to as such hereafter.

We have also constructed the number fluctuation measure

$$T_{6\sigma_{v_b}} = |T_+(\mu_{v_b} + 3\sigma_{v_b}) - T_+(\mu_{v_b} - 3\sigma_{v_b})|. \tag{3.34}$$

This measure takes values between 0 and 1, with 0 indicating absolute insensitivity to fluctuation and 1 indicating a complete population shift resulting from extreme fluctuations in the initial COM position and momentum.

Figure 3.3(a) shows that $T_+(\mu_{v_b} + 3\sigma_{v_b})$ behaves as we might expect. As the collisional kinetic energy of the system decreases (shown by decreasing v_0), we see that extreme fluctuations in the initial COM position and momentum cause a deviation from from equal splitting. At first, when v_0 is relatively high ($v_0 \gtrsim 0.5$), the deviation of T_+ from 0.5 is weakly dependent on v_0. Then, as v_0 approaches 0.25 the effect of disallowed states becomes dominant. In this regime we see that extreme positive energy quantum fluctuations rapidly enhance transmission.

The effects of extreme negative energy quantum fluctuations, quantified by $T_+(\mu_{v_b} - 3\sigma_{v_b})$, are slightly more complicated. The careful selection of q makes the bound states (as described in Section 3.4.2 and observed in Section 3.4.2) a notable factor. This can be seen by the more complex structure of the data displayed in Fig. 3.3(b). At the high energy end of the velocity range we see the same weak deviation of T_+ from 0.5 as that described above for extreme positive energy fluctuations. However, where we might expect disallowed states to enhance reflection (namely $v \lesssim 0.25$), we see a revival in the transmission. This is a result of a bound state confining the wave function to the region around the barrier at the bottom of the trap, resulting in a T_+ failing to tend to 0. This effect is consistent with the reduced kinetic energy being insufficient to split the soliton in the low velocity regime.

Finally, in Fig. 3.3(c) we see that $T_{6\sigma_{v_b}}$ does generally increase as v_0 decreases, showing that number fluctuations become very important at low kinetic energies as a result of energetically disallowed states enhancing transmission/reflection. However, as a result of the previously discussed impact of bound states, $T_{6\sigma_{v_b}}$ does not vary smoothly between 0 and 1. This effect could be treated as an artefact and re-

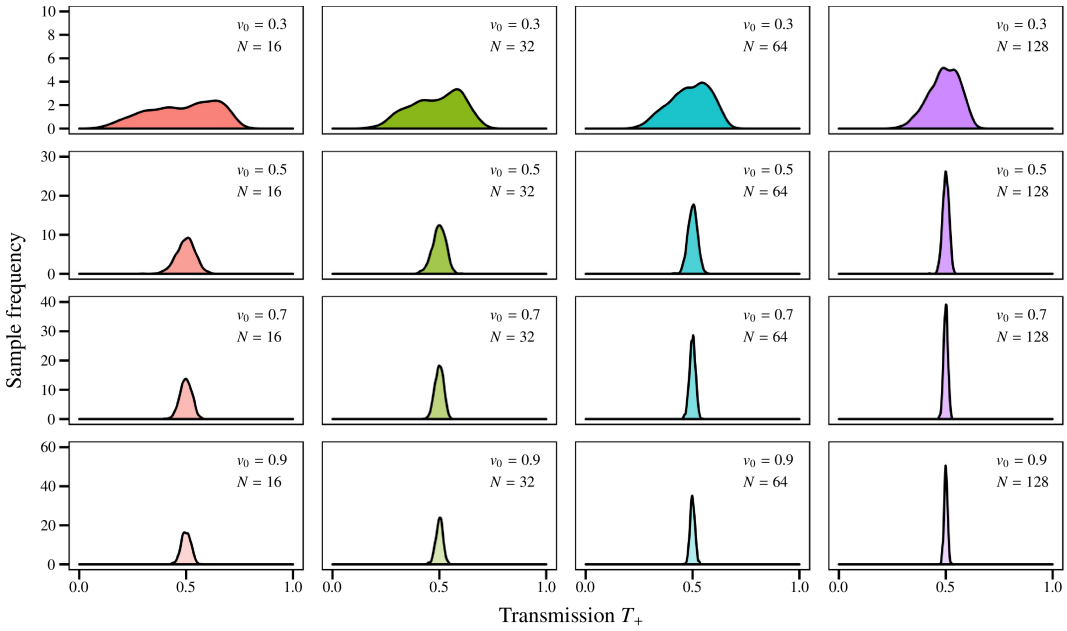

Figure 3.4: Distributions of the transmission T_+ obtained from Monte-Carlo simulations. Here we show results for a range of trap frequencies and particle numbers, giving a range of uncertainties in the initial COM position and momentum. In the range explored, we see that the effects of varying the trap frequency (and so kinetic energy) dominate the dynamics, with narrow Gaussians at high energy, but a bimodal structure arising at low energy when energetically disallowed states arise. Reproduced from Ref. [49].

moved by only taking the post-splitting positive domain integral (T_+) far from the barrier, thus excluding bound states. This would give a continuous, smooth range between 0 and 1, but would obscure the effect of bound states.

Monte-Carlo analysis of transmission with quantum fluctuations

In order to characterise the distribution of the transmission T_+ after factoring in quantum uncertainty in the initial condition we performed a selection of Monte-Carlo simulations. These simulations allow us to develop a broader qualitative understanding of the effects of quantum uncertainty. Here we have selected the same values of the particle number N as used previously and consider velocities $v_0 = 0.3, 0.5, 0.7, 0.9$. We present the results of 16 Monte-Carlo simulations for each v_0, N pair. Each simulation is comprised of 1000 realisations.

Figure 3.4 displays the different distributions of the transmission T_+ which arise from varying the energetic regime and particle number. In the bottom row we see that for high v_0 the distribution is a narrow Gaussian for all displayed N. Reduc-

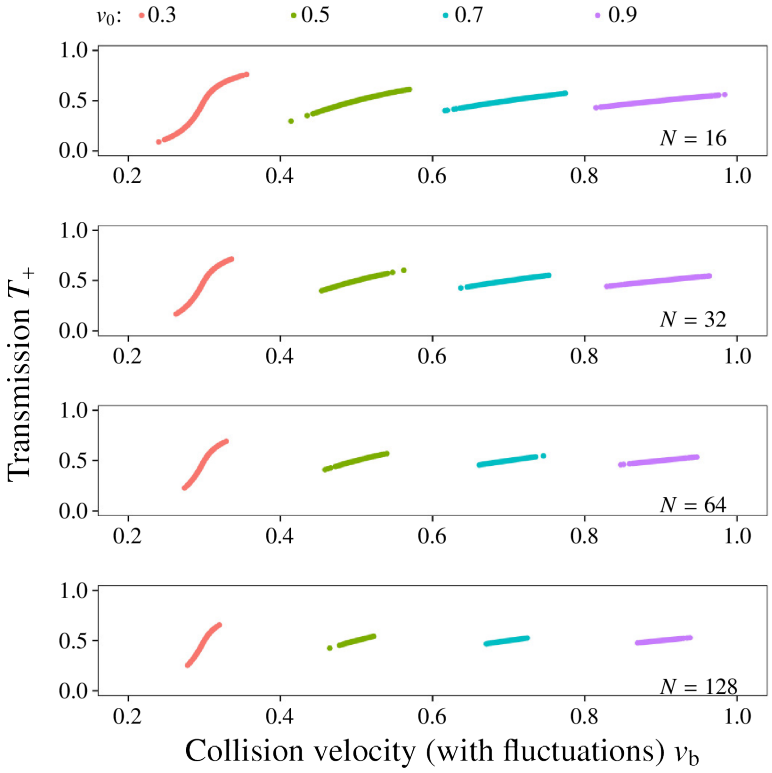

Figure 3.5: Results of Monte-Carlo simulations. Here we show the dependence of transmission on T_+ on the collision velocity (v_b) after quantum position and momentum fluctuations have been added to a base collision velocity (v_0). For each v_0 the barrier strength was set to ensure equal splitting in the limit of zero fluctuations. We see that in the low energy regimes the transmission can be very sensitive to quantum fluctuations. Reproduced from Ref. [49].

ing v_0 for a given N (reading up the column) causes the standard deviations of the Gaussians to broaden. For $v_0 = 0.3$ (the top row of Fig. 3.4) a bimodal distribution appears, again illustrating that the equal splitting case is less easily accessed. This behaviour is evident for all N. Reading across the rows (varying N while keeping v_0 constant) shows that increasing N simply reduces the width of the transmission distribution. This illustrates that the N dependence is secondary to the v_0 dependence in the range explored here. This is evident in that there is still significant broadening of the transmission distribution at low v_0 even for the highest values of N. We might expect this to be the case, given that the range of N explored here is, in experimental terms, very low.

We can see the functional dependence of transmission on v_b ($T_+(v_b)$) in Fig. 3.5.

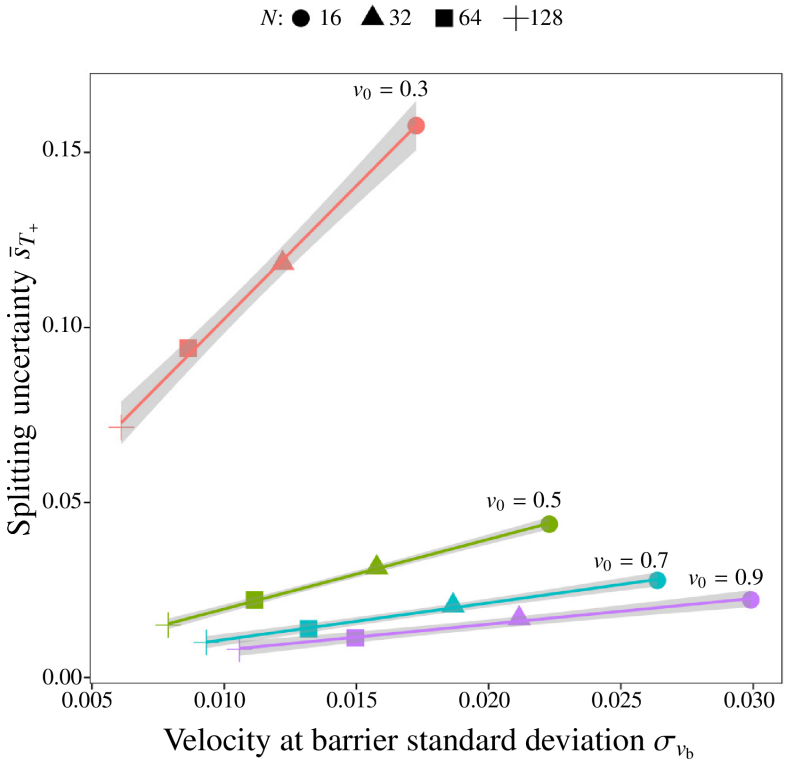

Figure 3.6: Results of Monte-Carlo simulations. Here, the standard deviations associated with the final transmission distributions depicted in Fig. 3.4. We see a weak linear dependence on the sample velocity uncertainty $\bar{s}_{v_b}$ for high v_0, which becomes stronger, but less linear, as we reduce the energy. This can be seen by the widening (shaded) 95% confidence intervals of the linear fits. Reproduced from Ref. [49].

We see that in the higher energetic regime ($v_0 > 0.5$) the transmission has a weak approximately linear dependence on the velocity. The relatively small gradient of this dependence indicates that the transmission is less sensitive to the fluctuations. For the $v_0 = 0.3$ data we see that the dependence becomes very sensitive to small fluctuations around $v_b = 0.3$, the equal splitting case. This confirms that proximity to the energetically disallowed state can cause large variations in transmission when quantum fluctuations are considered. Increasing N has the effect of narrowing the distributions of the fluctuations, and so these fluctuations can affect the transmission less dramatically, even when close to the energetically disallowed state. It should be noted that the points in Fig. 3.5 lie along curves with structure analogous to those depicted in Fig. 3.2(e).

We can quantify the relationship between the initial quantum uncertainties (via σ_{v_b})

and the resulting transmission uncertainty σ_{T_+} by making a maximum-likelihood estimate $\bar{s}_{T_+}$ based on our data. The process of maximum-likelihood parameter estimation is a standard statistical technique, and so we refer the reader to standard texts for a full discussion (see, for instance, Ref. [178]). It is used to obtain the most probable set of distribution parameters given a set of data and an assumed probability density function with associated characteristic parameters (generally a measure of location and spread, such as the Gaussian's mean μ and variance σ^2). In essence, the method achieves these estimates by constructing a "likelihood function" $L(\mu, \sigma)$ which is the product of probabilities of each individual data point given μ and σ (the probabilities are obtained from the probability density function $f(x_i; \mu, \sigma)$ for all x_i in the data set $\mathbf{x}$). The likelihood function L is then maximised with respect to μ and σ, giving the most probable values of these parameters given the data. This maximisation can often be obtained analytically (for instance, the sample mean and variance are maximum-likelihood estimators of the Gaussian distribution [178]), but it is often necessary to carry out this process numerically for more complex distributions.

We assume that the data follows a truncated Gaussian distribution on the interval $[0, 1]$. The results of numerical estimates of the width parameter $\bar{s}_{T_+}$ are shown in Fig. 3.6. We see that $\bar{s}_{T_+}$ has approximately linear correlations with σ_{v_b}. This correlation becomes stronger, illustrated by the increased gradient of the linear fit, as we reduce v_0. The grey shaded areas indicate a 95% confidence interval for the least squares linear regression. The confidence interval associated with $v_0 = 0.3$ is widest, indicating a less linear relation between σ_{v_b} and $\bar{s}_{T_+}$ in the low energy regime.

3.4.6 Split induced phase shift

In order to construct an analysis of soliton interferometry there is another aspect of soliton splitting which we must address. The act of splitting the soliton (which gives us two coherent matter waves to interfere) causes a phase difference to arise between the solitons. This is similar to the case of classical optics. A classical analysis of electromagnetic fields at interfaces between media, yielding the Fresnel equations [179], shows us that when light passes into a medium with a higher refractive index the reflected part is phase shifted by π with respect to the transmitted part. This effect is particularly relevant in the case of optical interferometers where a beam of light is split by a beam splitter. In the case of soliton splitting the principle is similar, and the barrier (here acting as our beam splitter) imparts a

phase difference between the two residual solitons. In contrast to the optical case, the transmitted soliton is $\pi/2$ phase shifted with respect to the reflected soliton. In other words, the phase difference has half the magnitude and opposite sign. This difference between the two cases is understandable, as the two are very different physical systems and so are governed by very different sets of equations. The systems are analogous but, of course, not identical. We now present a derivation of this phase shift.

It has been rigorously analytically shown [40] that, in the high kinetic energy limit (high soliton velocity v) of the 1D untrapped system, when a soliton is split at a δ-function barrier the phases imparted to the solitons by the split are

$$\begin{aligned}\vartheta_T &= \left[1 - A_T^2\right]\left|\frac{x_0}{2v}\right| + \arg\left(t_q(v)\right) + \vartheta_0\left(|t_q(+v)|\right),\\ \vartheta_R &= \left[1 - A_R^2\right]\left|\frac{x_0}{2v}\right| + \arg\left(r_q(v)\right) + \vartheta_0\left(|r_q(-v)|\right),\end{aligned} \tag{3.35}$$

where

$$\vartheta_0(\omega) = \int_0^\infty \ln\left(1 + \frac{\sin^2(\pi\omega)}{\cosh^2(\pi\zeta)}\right)\frac{\zeta}{\zeta^2 + (2\omega - 1)^2}d\zeta. \tag{3.36}$$

The $\vartheta_{R,T}$ are the reflected, transmitted soliton phases, and $A_{R,T}$ are the reflected, transmitted soliton amplitudes. Quantities $r_q(v)$ and $t_q(v)$ are the transmission and reflection rates of a δ-function in the linear regime, given by

$$t_q(v) = \frac{iv}{iv - q} \qquad \text{and} \qquad r_q(v) = \frac{q}{iv - q}. \tag{3.37}$$

If the barrier strength and initial velocity (q and v) are selected to be equal ($q = v$), such that $|r_q(v)| = |t_q(v)|$ and (as a result) $A_R = A_T$ then the soliton is split equally into two secondary solitons of equal amplitude. This is desirable because later we will wish to collide the resulting solitons at a barrier, and if these solitons are of similar size then the interference between them is more pronounced. It is also true that a size difference causes secondary nonlinear phase shifts to arise during the collision, which is undesirable.

Making this selection, such that the soliton is equally split, and substituting appropriate values of q, v, $A_{R,T}$, $|r_q(v)|$ and $|t_q(v)|$ into Eq. (3.35) we see that the relative phase between the solitons reduces to

$$\begin{aligned}\vartheta_T - \vartheta_R &= \arg(t_q(v)) - \arg(r_q(v))\\ &= \pi/2.\end{aligned} \tag{3.38}$$

A broader discussion of the effect of a finite width barrier on the phase shift accumulated during splitting is, again, available in Ref. [169]. We will use the $\pi/2$ figure as an estimate of the phase difference accumulated by splitting on a Gaussian barrier, as justified in [48], for the rest of the current work.

Chapter 4: Soliton collisions at narrow barriers

4.1 Introduction

In this chapter we demonstrate that a potential barrier can be used to recombine solitary waves, by arranging for them to collide at the location of the barrier. In such collisions, the relative norms of the two outgoing solitary waves were shown to be governed by the phase difference Δ between the incoming ones. In the mean-field description the relative norms of the outgoing waves exhibit enhanced sensitivity to small variations in the phase Δ; however, a simulation of the same system including quantum noise, via the truncated Wigner method [47], showed increased number fluctuations that ultimately negated this enhancement [30]. The work presented in this chapter was originally published in Ref. [48]

4.2 Physical system

To describe such collisions we introduce a two-soliton initial condition of the form

$$\psi(x) = \frac{1}{2+2b}\left\{\mathrm{sech}\left(\frac{x+x_0}{2+2b}\right)e^{ivx} + b\,\mathrm{sech}\left(\frac{b[x-x_0]}{2+2b}\right)e^{-i(vx+\Delta)}\right\}, \tag{4.1}$$

This is a two-soliton initial condition which has arbitrary relative amplitude determined by b and is normalised to 1 for $0 \leq b \leq 1$. In this chapter we only consider the untrapped version of Eq. (3.5), specifically

$$i\frac{\partial\psi(x)}{\partial t} = \left[-\frac{1}{2}\frac{\partial^2}{\partial x^2} + \frac{q}{\sigma_\mathrm{b}\sqrt{2\pi}}e^{-x^2/2\sigma_\mathrm{b}^2} - |\psi(x)|^2\right]\psi(x). \tag{4.2}$$

By examining soliton collisions at a barrier for general b, Δ, σ_b, q and v we give a detailed explanation of the nonlinear recombination which occurs after the solitons collide at the potential barrier and are recombined into left- and right-travelling waves in a phase-sensitive way. This general and comprehensive treatment of two-soliton collisions at a barrier constitutes the main result of the chapter. For the case of solitons of equal size (as reported in Ref. [30]) we illustrate this phase dependence in Fig. 4.1(b). In this chapter we present an analytic description of the recom-

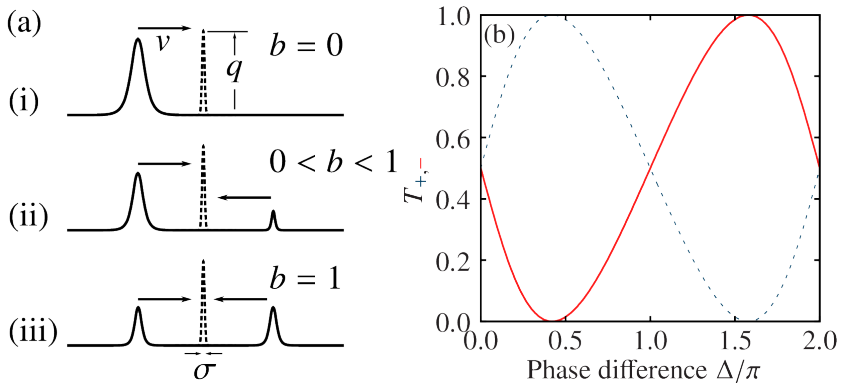

Figure 4.1: (Color online) (a) Schematic of the collisions we consider: two bright solitons [one in the case $b = 0$ (a)(i)] (solid lines) collide at a narrow Gaussian potential barrier (dashed line). The norms of the two outgoing waves are nonlinearly dependent on the relative phase Δ between the solitons, as illustrated in (b) for equal-amplitude solitons [the case $b = 1$ (a)(iii)]; solid red (dashed blue) lines indicate the outgoing wave in the negative (positive) x domain. Here the soliton velocity is $v = 2$ and the barrier width is characterised by $\sigma_b = 0.28$. Reproduced from Ref. [48].

bination for the general two-soliton case ($b > 0$) in the limit of a δ-function barrier ($\sigma_b \to 0$). This description is derived from an exact description of the single-soliton case ($b = 0$) in the same limit [40, 41]. We compare this to numerical simulations, and find the analytic description is exact in the limit of high velocity. In addition to yielding useful predictions for the relative norms of the recombined waves, this analytic method allows us to estimate whether one, or both, of the outgoing waves are bright solitons. We also numerically investigate the case of a Gaussian barrier, $\sigma_b > 0$.

4.3 Analytic treatment for δ-function barrier

We now give an approximate analytical description of the dynamics of two fast-moving bright solitons colliding at a δ-function barrier, which we subsequently compare to numerical simulations in order to give a fuller picture of the real dynamics that we might expect to see in an experiment. This analysis stops short of the full analytic rigor used in [40] but is consistent within its assumptions of linearity. As previously stated, during the time over which *one* bright soliton interacts with the potential we can describe the system as linear [40]. Here we extend this argument to a scenario in which *two* bright solitons collide at a δ-function potential,

as described by the equation

$$i\frac{\partial\psi(x,t)}{\partial t} = \left[-\frac{1}{2}\frac{\partial^2}{\partial x^2} + q\delta(x) - |\psi(x,t)|^2\right]\psi(x,t), \tag{4.3}$$

(which, again, is [Eq. (1.63)] plus an externally applied potential) and initial condition

$$\begin{aligned}
\psi(x,0) &= \psi_+(x) + \psi_-(x),\\
\psi_-(x) &= \frac{1}{2+2b}\operatorname{sech}\left(\frac{x+x_0}{2+2b}\right)e^{ivx},\\
\psi_+(x) &= \frac{b}{2+2b}\operatorname{sech}\left(\frac{b(x-x_0)}{2+2b}\right)e^{-i[vx+\Delta]},
\end{aligned} \tag{4.4}$$

[Eq. (4.1)]. We achieve this by making use of the second result of Ref. [40], which we apply to the positive and negative domain bright solitons, ψ_+ and ψ_-, separately, before taking a linear combination of the results. This means that at some time $|x_0|/v < t < v^{-\eta} + |x_0|/v$ after the barrier collision the solution can be written as a sum of four sech profiles, two in each of the positive and negative domains;

$$\psi(x,t) = \psi_{+T}(x,t) + \psi_{-R}(x,t) + \psi_{-T}(x,t) + \psi_{+R}(x,t). \tag{4.5}$$

Here ψ_{+T} denotes the bright soliton transmitted to the negative domain which originated in the positive domain, ψ_{-R} denotes the bright soliton originating from and reflected back into the negative domain, and so on. In this scheme

$$\begin{aligned}
\psi_{+T}(x,t) &= e^{i(\phi_{+T}+\varphi_{+T}+\Delta)}A_{+T}\operatorname{sech}\left(A_{+T}\left[x-x_0+tv\right]\right),\\
\psi_{+R}(x,t) &= e^{i(\phi_{+R}+\varphi_{+R}+\Delta)}A_{+R}\operatorname{sech}\left(A_{+R}\left[x+x_0-tv\right]\right),\\
\psi_{-T}(x,t) &= e^{i(\phi_{-T}+\varphi_{-T})}A_{-T}\operatorname{sech}\left(A_{-T}\left[x+x_0-tv\right]\right),\\
\psi_{-R}(x,t) &= e^{i(\phi_{-R}+\varphi_{-R})}A_{-R}\operatorname{sech}\left(A_{-R}\left[x-x_0+tv\right]\right).
\end{aligned} \tag{4.6}$$

Two phase factors appear above; the $\phi_{\pm R/T}$ are those associated with the standard soliton solution and are given by

$$\begin{aligned}
\phi_{\pm T} &= \mp vx + \left[A_{\pm T}^2 - v^2\right]t/2,\\
\phi_{\pm R} &= \pm vx + \left[A_{\pm R}^2 - v^2\right]t/2.
\end{aligned} \tag{4.7}$$

The $\varphi_{\pm R/T}$ factors are imparted by the collision, and are described by

$$\begin{aligned}\varphi_{\pm T} &= \left[1 - A_{\pm T}^2\right]|x_0|/(\mp 2v) + \arg\left(t_q(v)\right) + \varphi_0(|t_q(\mp v)|),\\ \varphi_{\pm R} &= \left[1 - A_{\pm R}^2\right]|x_0|/(\mp 2v) + \arg\left(r_q(v)\right) + \varphi_0(|r_q(\mp v)|).\end{aligned}$$

With $b = 1$, barrier height $q = v$, and fast-moving solitons (v large) both initial bright solitons are split equally, such that the amplitudes $A_{\pm R/T}$ are all equal and global phases can be dropped. In this case Eq. (4.5) simplifies dramatically, and shortly after the collision can be written as

$$\begin{aligned}\psi(x,t) &= \psi_{++}(x,t) + \psi_{--}(x,t)),\\ \psi_{++}(x,t) &= P_+(\Delta) f_+(x,t),\\ \psi_{--}(x,t) &= P_-(\Delta) f_-(x,t),\end{aligned} \tag{4.8}$$

where the terms

$$\begin{aligned}P_-(\Delta) &= \frac{1}{2}\left\{e^{i\arg(r_q(q))} + e^{i\left[\arg(t_q(q))+\Delta\right]}\right\},\\ P_+(\Delta) &= \frac{1}{2}\left\{e^{i\arg(t_q(q))} + e^{i\left[\arg(r_q(q))+\Delta\right]}\right\},\end{aligned} \tag{4.9}$$

contain information about the constructive and destructive interference between the transmitted and reflected waves. It should be noted that this treatment allows us to infer the bright soliton interactions, but does not give us a complete solution; the terms f_+ and f_- contain information about the outgoing wave profiles. By taking a linear superposition of the resultant bright solitons we initially obtain a sech profile which is not a single-soliton solution. However, in subsequent nonlinear evolution this profile returns to a soliton profile to within a known error, as documented in Appendix B of Ref. [40].

At a suitably large time after the collision, when the solitons have again separated to the extent that they are again effectively independent, inspection of $|\psi|^2$ shows that the bright solitons are modulated by the factors

$$\begin{aligned}|P_-(\Delta)|^2 &= \frac{1}{2}\left[1 - \sin(\Delta)\right],\\ |P_+(\Delta)|^2 &= \frac{1}{2}\left[1 + \sin(\Delta)\right].\end{aligned} \tag{4.10}$$

These factors determine the norm of the outgoing waves in the positive and negative

domains, defined by

$$T_{\pm} = \pm \lim_{t\to\infty} \int_{0}^{\pm\infty} |\psi(x,t)|^2 dx = |P_{\pm}(\Delta)|^2. \tag{4.11}$$

Within the analytic approach presented here $T_{\pm}$ are functions of Δ alone. It should be noted that the symmetry of the initial condition and linear interaction means that the phase interactions apply to both the transmitted and reflected bright solitons and the radiation terms. As a result the quantity $T_{\pm}$ scribes the total density in the positive and negative domains, not just the respective bright solitons. For suitably high incident velocities this radiation becomes negligible, in accordance with Eq. (3.12).

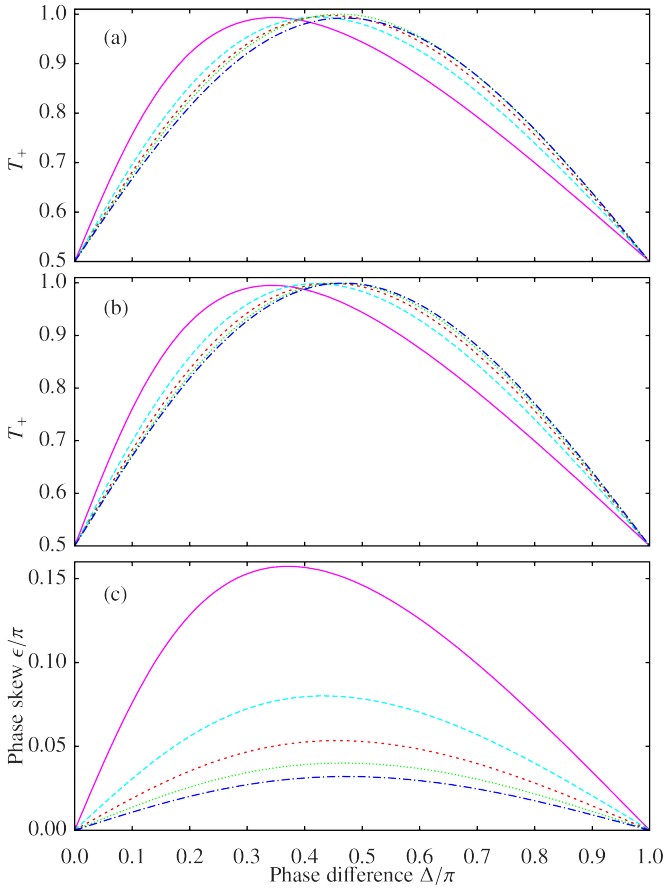

Figure 4.2: (Color online) Phase skew of numerical results with respect to analytic prediction for equal-size ($b = 1$) bright soliton collisions at a narrow barrier. (a) Numerically obtained data showing the dependence of the norm of the outgoing wave in the positive domain, T_+, after Gaussian barrier collision, on phase difference Δ. Shown here are interference curves for solitons moving with velocity $v = 1$ (fuchsia, solid), 2 (light blue, long dashed), 3 (red, short dashed), 4 (green, dotted) and 5 (dark blue, dot-dashed). The width of the barrier was $\sigma_b = 0.14$. (b) [see (a)] Collisions at a δ-function barrier. Notice the qualitatively identical form of the curves, illustrating that both δ-function and Gaussian barriers exhibit the same skew, and so both undergo the same non-linear effects. (c) Numerically obtained data showing the phase perturbation ϵ [Eq. (4.13)] due to non-linear effects in a soliton collision at a δ-function barrier. Shown here, in order of descending amplitude, are the skewness parameters (ϵ) of the interference curves for solitons moving with velocity $v = 1, 2, 3, 4$, and 5 colliding at a δ-function barrier. (a)-(c) are the upper left quarters of the full data set; the plots are both symmetric about the lower and right hand axes. All results shown are calculated for $\alpha = q/v = 1$. Reproduced from Ref. [48].

4.4 Numerical results for δ-function and Gaussian barriers

In Fig. 4.2 we present results of numerical simulations of fast ($v \gtrsim 1$) bright soliton collisions at both δ-function[1] and Gaussian barriers. The norms of the outgoing waves, defined in our numerics by

$$T_{\pm} = \pm \int_{0}^{\pm\infty} |\psi(x, t_1)|^2 dx, \tag{4.12}$$

agree qualitatively with the predictions of our analytic treatment, but with a noticeable skew in the predicted sinusoid. This skew is also visible in the results for the Gaussian barrier case shown in Fig. 4.1. We parametrise this skew by ϵ and describe the norms of the outgoing waves, $T_{\pm}$, as

$$T_{\pm} = \frac{1 \pm \sin(\Delta + \epsilon(\Delta))}{2}. \tag{4.13}$$

This skewness parameter is less pronounced for increasing velocities, i.e.,

$$\lim_{v\to\infty} \max(|\epsilon|) = 0. \tag{4.14}$$

The presence of the skew in simulations with both Gaussian and δ-function barriers rules out any explanation in terms of the barrier structure. However, it is well known that when solitons collide in the absence of a barrier they induce a small phase and position shift in one another [20, 29, 159]. We propose that the skew is a result of interactions between the solitons while approaching the barrier; more fundamentally, this is a result of the condition of a brief interaction not being fully satisfied. For instance, from initial condition Eq. (4.1) the phase (φ_l') and position (x_l') shift on the left hand soliton are given by

$$\frac{2x_l'}{1+b} + i\varphi_l' = 2\ln\left(\frac{v+i}{v+i\,[(1-b)/(1+b)]}\right). \tag{4.15}$$

In the case of equal amplitudes and velocities total phase difference reduces to $\varphi' = \pm 4\arctan(1/v)$ or, in the limit of high velocity, $\varphi' \approx \pm 4/v$. In our scenario only part of this phase-shift can occur before the solitons enter the linear regime, and so we expect that our skewness parameter ϵ will be some fraction of φ'. What we have

[1] Within our Fourier pseudo-spectral method a δ-function barrier can be implemented with high accuracy in momentum space using the approach outlined in Ref. [180].

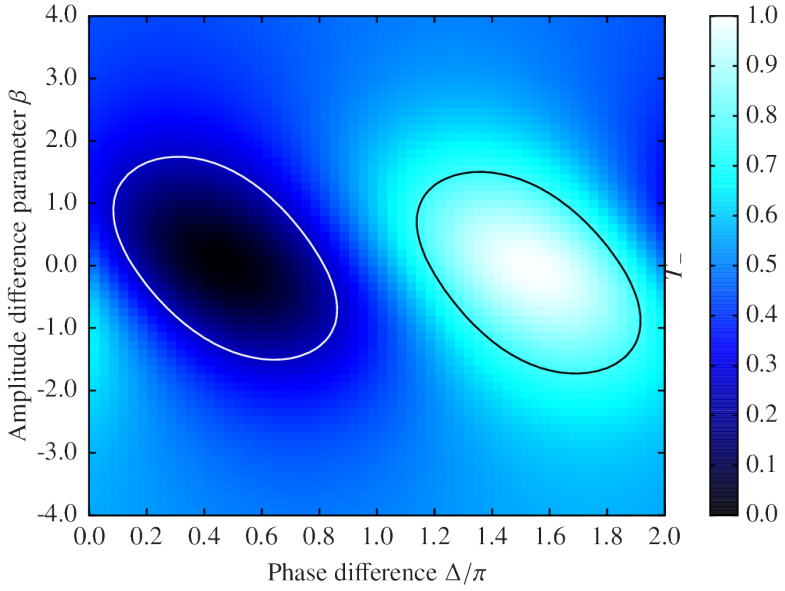

Figure 4.3: Numerically computed transmission coefficient T_+ illustrating the interference between solitons of different initial amplitudes ($b = e^{\beta}$) colliding at a δ-function barrier. Even in the case of a large difference in initial amplitude (large $|\beta|$) there is still interference between the solitons. The contour lines show the boundary between having one (interior regions) and two (exterior region) outgoing bright solitons in the analytic treatment [see Eq. (3.13)]. All results shown are calculated for $\alpha = q/v = 1$ and $v = 5$. Reproduced from Ref. [48].

observed from our numerics is that ϵ oscillates with Δ but the maximum value is $\epsilon_{\max} \approx \varphi'/8$. This is consistent with the behaviour we observe in the high velocity limit.

4.5 Inhomogeneous soliton collisions

It should also be noted that the interference effect is present in collisions between solitons of differing amplitudes. By taking $b = e^{\beta}$ we see that there is still interference between the transmitted positive and reflected negative bright solitons (and vice versa) [Fig. 4.3]. Along the line $\beta = 0$, where the amplitudes of the incoming bright solitons are equal, we can clearly see a sinusoidal dependence on Δ. For nonzero β there is still a notable dependence on the incoming phase difference, but this effect is soon washed out if the difference in initial amplitudes becomes too large. It is true, however, that the solitons do not have to be of similar size to constructively or destructively interfere.

The black (white) contour on Fig. 4.3 shows where the final population in the positive (negative) domain was not great enough, after interference, for the final aggregation to form a soliton. This is determined by treating the total positive (negative) domain population as the transmission (reflection) coefficient in equation (3.13). From Eq. (3.13) we see that $|t_q|$ and $|r_q|$ must both be > 0.5 to get two outgoing solitons. We determine $|t_q|$ and $|r_q|$ numerically as

$$\sqrt{T_\pm} = \sqrt{\pm \int_0^{\pm\infty} |\psi|^2 dx}. \tag{4.16}$$

As such, the white contour marks where $T_- = 0.25$ ($T_+ = 0.75$) and the black contour marks where $T_+ = 0.25$ ($T_- = 0.75$).

Chapter 5: Bright matter-wave soliton interferometry

5.1 Introduction

A related work [30] considered an interferometer using a narrow potential barrier as a beamsplitter for harmonically trapped solitary waves, based on the particular configuration of a recent experiment [46]. In this chapter our first result will be to construct the interferometer system and analyse its behaviours. In particular, we wish to consider the boundary between quantum behaviour and more classical behaviour investigated in Chapter 3, which will determine where interferometry is a more practical goal. We will outline two different geometries which might be employed for soliton interferometry and delineate energetic regimes where these implementations are practicable. This chapter is comprised of work presented in the second half of Ref. [49] and Ref. [50].

We again consider the dynamical equation

$$i\frac{\partial\psi(x)}{\partial t} = \left[-\frac{1}{2}\frac{\partial^2}{\partial x^2} + \frac{q}{\sigma_{\rm b}\sqrt{2\pi}}e^{-x^2/2\sigma_{\rm b}^2} + \frac{\omega_x^2 x^2}{2} - |\psi(x)|^2 \right]\psi(x), \tag{5.1}$$

which is equivalent to Eq. (1.63) with an extra externally applied splitting potential, and initial condition

$$\psi_0 = \frac{1}{2}\mathrm{sech}\left(\frac{x-x_0}{2}\right)e^{ivx}, \tag{5.2}$$

5.2 Analysis of soliton interferometry

We can use the above results regarding soliton interactions at narrow barriers to analyse and construct a soliton interferometer. Soliton interferometry is a three step process.

First we split a ground state soliton into two lesser solitons of equal size at a narrow potential barrier [Fig. 5.1(a,b)(i)]. In the case of a δ-function barrier, this split causes the transmitted soliton to gain a $\pi/2$ phase shift relative to the reflected soliton, as described in Section 3.4.6.

These solitons then accumulate a further relative phase difference δ_{MZ}. This phase difference is the quantity we wish to measure. In this thesis we consider the case where this difference is gained by exposing one soliton to a phase shifting phenomenon.

In the third step the two solitons are made to collide at a narrow barrier [Fig. 5.1(a,b)(ii)]. After this final barrier collision the wave-function integrals on either side of the barrier,

$$I_{\pm} = \pm \int_{0}^{\pm\infty} |\psi(x)|^2 \mathrm{d}x, \tag{5.3}$$

allow us to determine the magnitude of δ_{MZ} [Fig. 5.1(a,b)(ii)]. Here I_{+} is the positive domain population and I_{-} is the negative domain population. We can determine the dependence of $I_{\pm}$ on δ_{MZ} by recalling the result obtained in Chapter 4, namely Eqs. (4.13) and (4.14). Using this result we can see that taking the phase difference Δ to be the sum of the phase shift we wish to measure, δ_{MZ}, and the phase shift accumulated during the initial split, $\pi/2$ we obtain

$$I_{\pm} = \frac{1 \pm \cos(\Delta + \epsilon)}{2}, \tag{5.4}$$

The different types of soliton interferometry available are determined by the geometry of the potentials used to confine and split the BEC. Here we investigate two different geometries. The first is a toroidal trap giving a periodic geometry with two splitting potentials at antipodal points (Sec. 5.3) [Fig. 5.1(a,c)]. This geometry is somewhat challenging to create experimentally but provides the simplest framework in which to establish our analytical results. The second geometry uses a non-periodic geometry with a weak axial harmonic trap centred on a narrow splitting potential (Sec. 5.4) [Fig. 5.1(b,d)]. This geometry makes it more experimentally viable, but questions of broken integrability require that we confirm the applicability of the results established above.

We will now present more expansive numerical analyses of these cases in order to determine whether our analytical results are confirmed numerically and also to determine the best energy regime in which to attempt soliton interferometry.

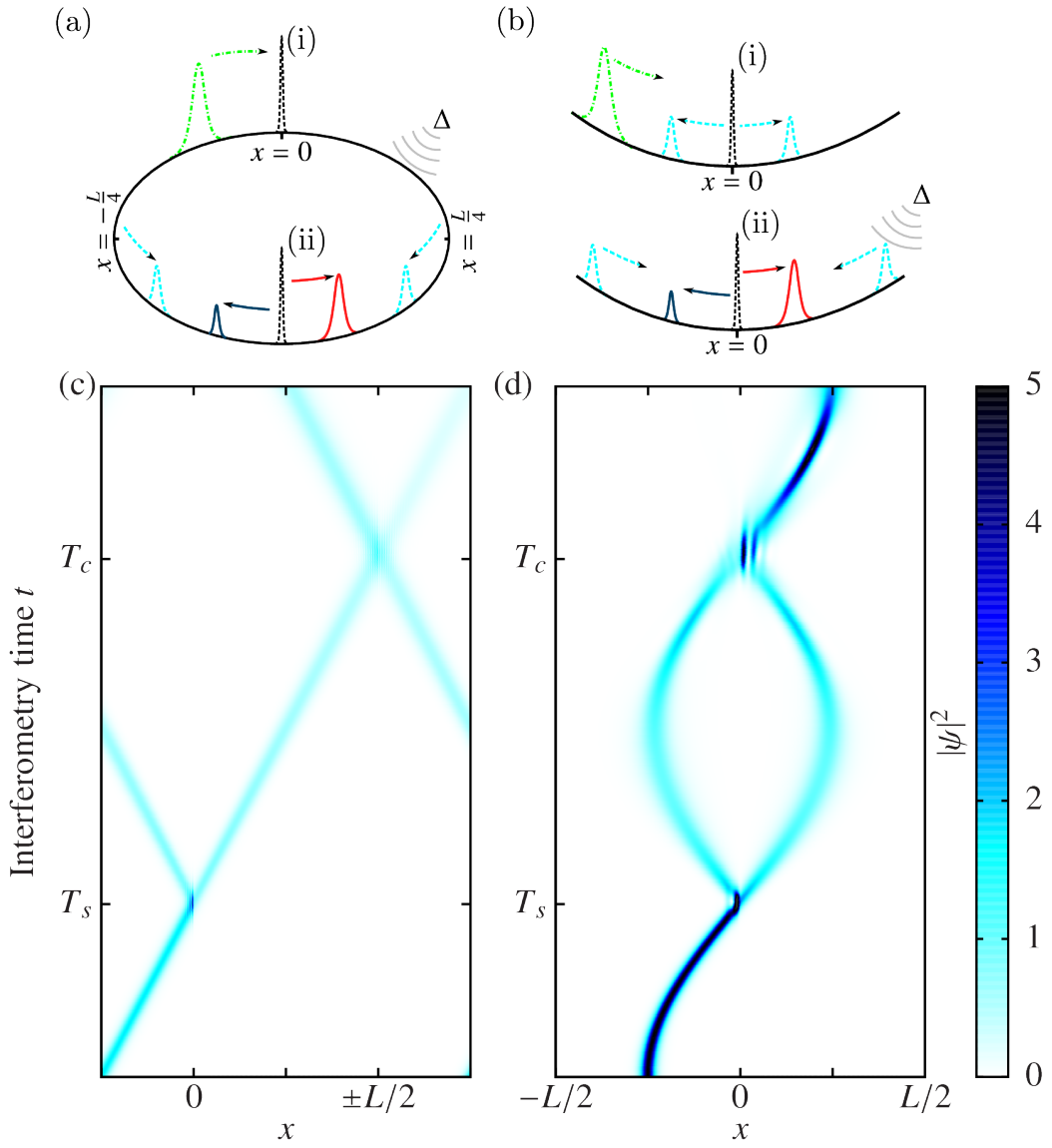

Figure 5.1: (a) Diagram of a Mach–Zehnder interferometer utilising a periodic confinement with two antipodal barriers. An example of the time evolution of the density for this configuration is displayed in (c). (b) Diagram of a Mach–Zehnder interferometer utilising harmonic confinement and a single splitting barrier. Again, an example of the time evolution for such a configuration is displayed in (d). Reproduced from Ref. [49].

5.3 Toroidal confinement Mach–Zehnder interferometry

An often discussed trapping geometry is the periodic toroidal trap. The existence of experimental results utilising optical [173] and magnetic [181, 182] confinement methods coupled with theoretical investigations proving localised bright soliton states exist in mean-field/truncated Hamiltonian [183], 3–D GPE [184], and coupled Gross–Pitaevskii Bogoliubov-de Gennes equations[185, 186] makes it worthwhile to consider extending our theory into this geometry. The toroidal geometry is beneficial in that it has no axial trapping, the presence of which breaks integrability and could, arguably, compromise our previous results. [1]

By treating Eq. (5.1) as periodic over the domain $-L/2 < x \leq L/2$, such that $\psi(-L/2) = \psi(L/2)$, we obtain a suitable dynamical equation. We use the same initial condition [Eq. (5.2)] and initial offset, but set the trap frequency $\omega_x = 0$ and directly vary the velocity v by imprinting a phase on the initial condition. We also add a second barrier at $x = \pm L/2$, where the solitons will be collided for interferometry, giving the dynamical equation

$$i\frac{\partial\psi(x)}{\partial t} = \left[-\frac{1}{2}\frac{\partial^2}{\partial x^2} + \frac{q}{\sigma_{\rm b}\sqrt{2\pi}}e^{-x^2/2\sigma_{\rm b}^2} + \frac{q}{\sigma_{\rm b}\sqrt{2\pi}}e^{-(x\pm L/2)^2/2\sigma_{\rm b}^2} - |\psi(x)|^2 \right]\psi(x). \quad (5.5)$$

Results of GPE simulations are shown in Figs. 5.2(a) and (b). We see that for very high velocities, $v \approx 4$, the interference follows our prediction [Eq. (5.23)] closely, with very small skews arising from nonlinear effects during the final barrier collision, showing that $\epsilon \approx 0$ in this regime.

As the velocity decreases, and we enter the transitional regime between high and low kinetic energy, ϵ increases and the skew becomes more prominent. As this happens the interference curve ceases to be sinusoidal and becomes approximately linear over some range, with $I_\pm \propto \mp\delta_{\rm MZ}$ up to some discontinuity. This discontinuity becomes narrower for higher ϵ and is situated at 2π for $v \approx 0.3$. In this regime, however, we are drawing close to the regime where equal soliton splitting becomes disallowed. For $v \lesssim 0.3$ the structure of the transmission becomes very complex, as the sensitivity of splitting to small changes in velocity becomes apparent. In this regime, soliton interferometry becomes impracticable.

[1] Indeed, adding any potential breaks the integrability, but for narrow splitting barriers one can consider the system to be widely integrable with small regions where the solution behaves differently.

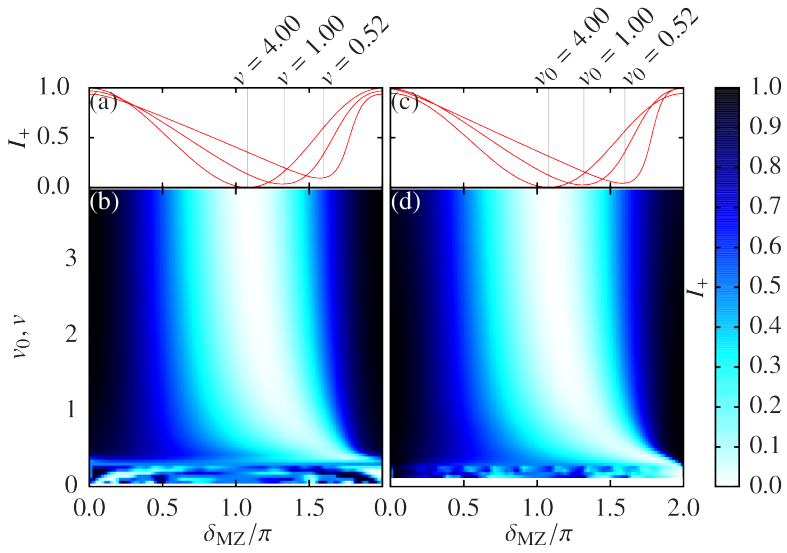

Figure 5.2: Numerically calculated transmission rates after the second collision, I_+, for two Mach–Zehnder interferometry geometries. Color-maps for the (b) toroidal Mach–Zehnder and (d) harmonic Mach–Zehnder cases show the full parameter space. (a) and (c) show specific curves of constant v, v_0 for the same respective scenarios and highlight the transition from the high energy sinusoidal dependence regime to the lower energy quasi-linear dependence regime. Reproduced from Ref. [49].

5.4 Harmonic confinement Mach–Zehnder interferometry

5.4.1 Overview

When considering trapping geometries for BEC experiments it is important to note that the addition of an axial harmonic trap globally breaks the integrability of the system, and so we can no longer say that we are studying true NLSE solitons in the mathematical sense. It is true, however, that the bright solitary waves supported by the system and confined in the harmonic trapping potential behave in a very soliton-like manner, staying robust to collisions and retaining their forms for long periods. Investigations utilising particle Hamiltonian models [15] to describe the soliton motion agree well with GPE simulations, and so we can safely treat these bright solitary waves as solitons.

5.4.2 Classical numerical analysis

The results of fully classical numerical simulations are displayed in Fig. 5.2(c)(d), obtained by evolving the initial condition described by Eq. (5.2) according to Eq. (5.1). In this case, the initial velocity v was set to zero while the soliton's velocity at the barrier, v_0, was set by varying the axial trap frequency ω_x (the dimensionless from of ω_{T}) and holding the initial offset x_0 at a constant value such that the soliton is initially well separated from the barrier.

The results are comparable to those seen for the periodic Mach–Zehnder case (Sec. 5.3), with good agreement with theory for high velocities, a linear dependence arising as we approach $v_0 \approx 0.3$ and finally complex structure arising in the low energy regime making interferometry impracticable. It should be noted that in the data set displayed in Fig. 5.2(d) is incomplete. The solid white band at $v \approx 0$ is a region where the system evolved too slowly to be numerically practical.

5.4.3 Interferometry sensitivity to quantum fluctuations

It was stated above that the linear relation between final domain population and phase shift might make interferometry more easily interpreted in the lower velocity regime. However, if we are to work in the regime we must consider the implications of the results outlined in Chapter 3; namely the impacts of energetically disallowed states and quantum uncertainty in the initial condition.

We again characterise the system's sensitivity to extreme positive/negative energy fluctuations. As such, we construct the quantities $I_+(\mu_{v_\mathrm{b}} \pm 3\sigma_{v_\mathrm{b}})$ and

$$I_{6\sigma_{v_\mathrm{b}}} = |I_+(\mu_{v_\mathrm{b}} + 3\sigma_{v_\mathrm{b}}) - I_+(\mu_{v_\mathrm{b}} - 3\sigma_{v_\mathrm{b}})|. \tag{5.6}$$

These quantities are analogous to those used previously (Sec. 3.4.5), but are obtained by allowing the system to evolve through the entire process of interferometry, rather than just the initial splitting event. In this section and the next section [where we discuss results displayed in Figs. 5.3, 5.4, 5.5 and 5.6] we have considered the $\Delta = 0$ case only in order to simplify our analysis.

Figure 5.3 shows the results of these simulations. We see that for high N and high v_0 the systems are reasonably insensitive to fluctuations. However, even in the high energy limit we see that as we decrease N the interferometry transmissions significantly deviate from their asymptotic values. This sensitivity is high compared

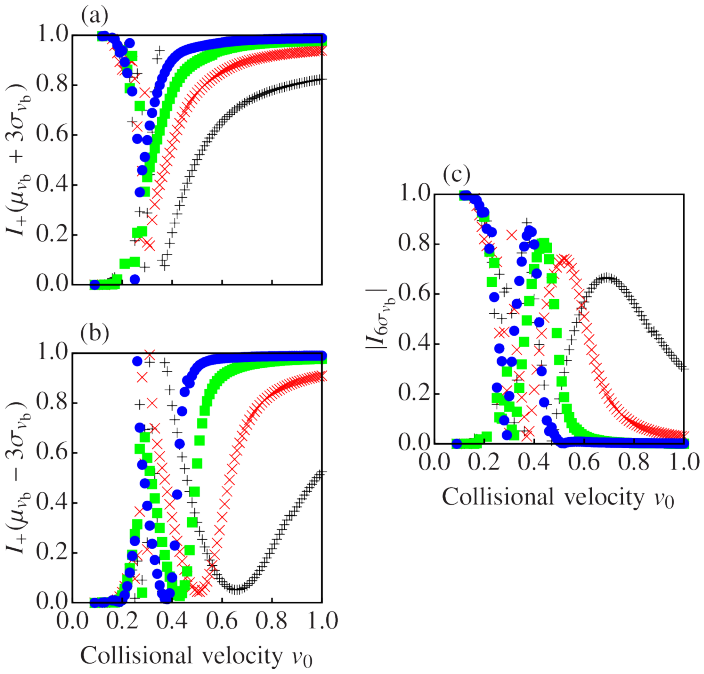

Figure 5.3: Results of numerical integrations illustrating the sensitivity of interferometry to extreme quantum fluctuation for various particle numbers. The interferometry transmission after extreme positive (negative) energy quantum fluctuations are displayed in panel (a) (panel (b)). The number fluctuation measure $I_{6\sigma_{v_b}}$ [Eq. (5.6)] is plotted in (c). For all plots we show $N = 16$ (+), 32 (×), 64 (■) and 128 (•). Reproduced from Ref. [49].

to that of the single splitting case, illustrating that the process of splitting (which occurs twice in interferometry) enhances the sensitivity of the classical system to initial fluctuations. The double enhancement in interferometry requires that we must be closer to the mean-field limit or suffer intolerable deviations from the classical behaviour.

As we decrease v_0 still further the previously discussed bound states and disallowed splitting events greatly complicate the dynamics of interferometry, making both the system and the results of our numerics difficult to interpret. This difficulty clearly shows that interferometry is impracticable in the low energy limit.

5.4.4 Monte-Carlo analysis of interferometry with quantum fluctuations

We now present a Monte-Carlo analysis of the effects of quantum uncertainties in the COM initial position and momentum. We explore the same parameter regime as

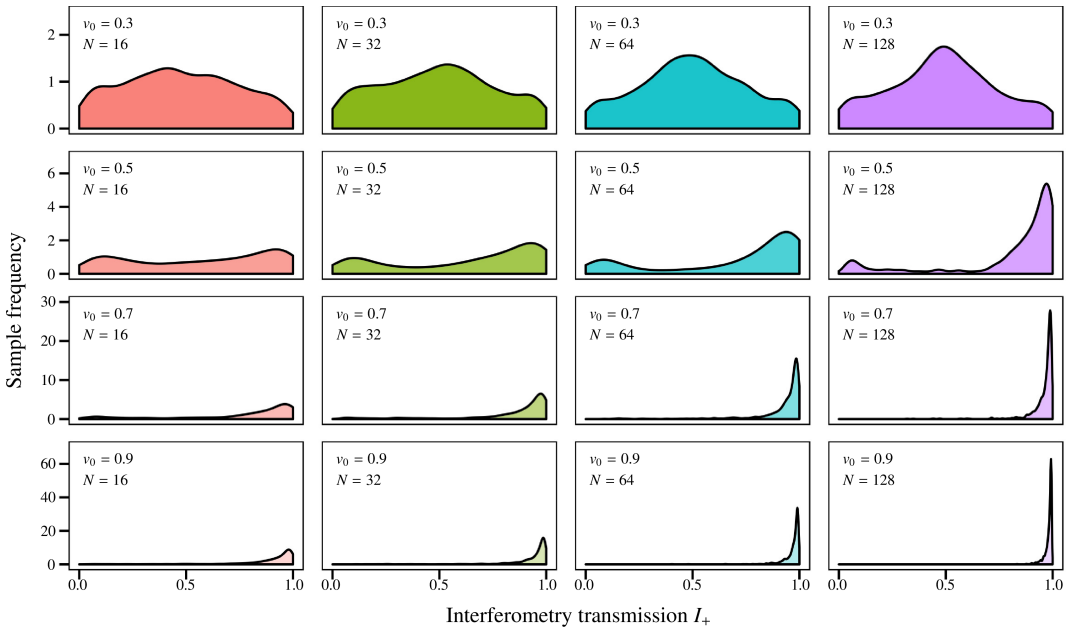

Figure 5.4: Distributions of the interferometry transmission I_+ obtained from Monte-Carlo simulations. Here we show results for a range of trap frequencies and particle numbers, giving a range of uncertainties in the initial COM position and momentum. In the range explored, we see that the effects of varying the trap frequency (and so kinetic energy) dominate the dynamics, with narrow Gaussians at high energy, but a uniform structure arising at low energy when interferometry becomes impracticable. Reproduced from Ref. [49].

in Section 3.4.5 and again present the results of 16 Monte-Carlo simulations. The plots in Fig. 5.4, illustrating the distributions of the interferometry transmission I_+, show characteristics similar to those in Fig. 3.4, but more pronounced. The distributions are approximately Gaussian at higher energies/particle numbers, but become more uniform at low energies ($v_0 = 0.3$), with a peak in the frequencies near $I_+ = 0.5$ arising from the presence of persistent bound states. This again indicates that interferometry is not viable in the low energy regime.

The transmission curves in Fig. 5.5 have a much more complex structure than that exhibited in its counterpart Fig. 3.5. At higher velocities, the points are clearly centred on the $I_+ = 1$ state, as we would expect, but as we lower the velocity the transmission becomes very sensitive to quantum fluctuations. This can be attributed to nonlinear phase shifts arising during the soliton collision at the barrier, compounded by a mis-match between the barrier strength and soliton velocity upon collision. Indeed, for the $v_0 = 0.3$ case these nonlinear phase shifts can cause I_+ to take literally

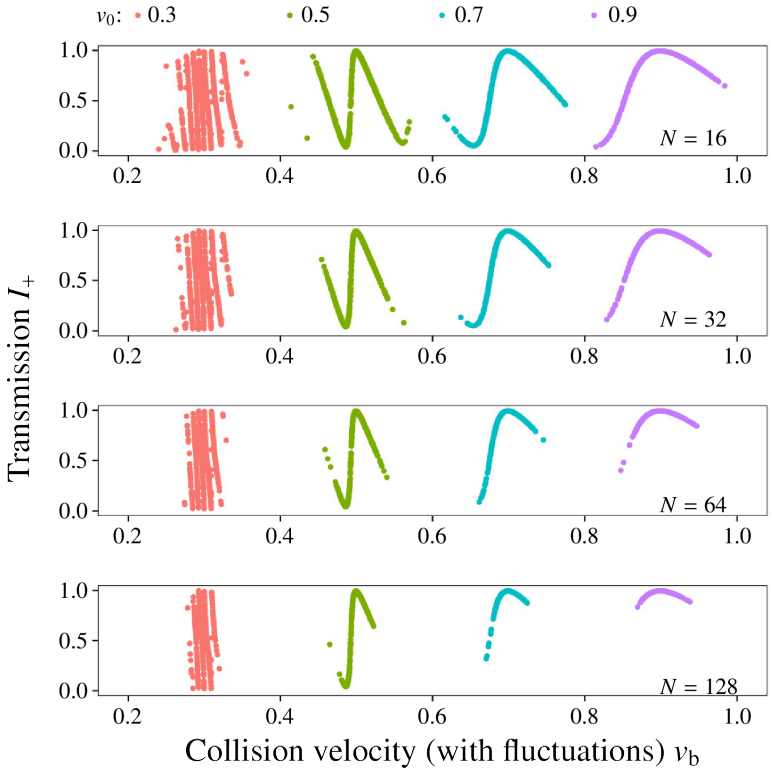

Figure 5.5: Results of Monte-Carlo simulations. Here we show the dependence of interferometry transmission on I_+ on the collision velocity (v_b) after quantum position/momentum fluctuations have been added to a base collision velocity (v_0). For each v_0 the barrier strength was set to ensure equal splitting in the limit of zero fluctuations. We see that in the low energy regimes the complex and velocity sensitive structure of the transmission renders interferometry unworkable. Reproduced from Ref. [49].

any value between 0 and 1, and the quantum fluctuations cause I_+ to tune across this period multiple times. This, alone, precludes any possibility of soliton interferometry in this regime. It is also visible that, even for high energies, a particle number of less than ≈ 130 can cause increased sensitivity, and so we really must ensure that we are in the regime of high N. After these considerations have been taken into account, it should be possible to perform interferometry with a quasi-linear signal [similar to that associated with the $v_0 = 0.52$ curve in Fig. 3.2(e)] for values of $v_0 \gtrsim 0.5$.

Finally, we again calculated maximum-likelihood estimates of the variance $\bar{s}_{I_+}$ of the transmission, which we again assumed to be distributed as a truncated Gaussian. The results of these calculations are displayed in Fig. 5.6. At higher velocities, we

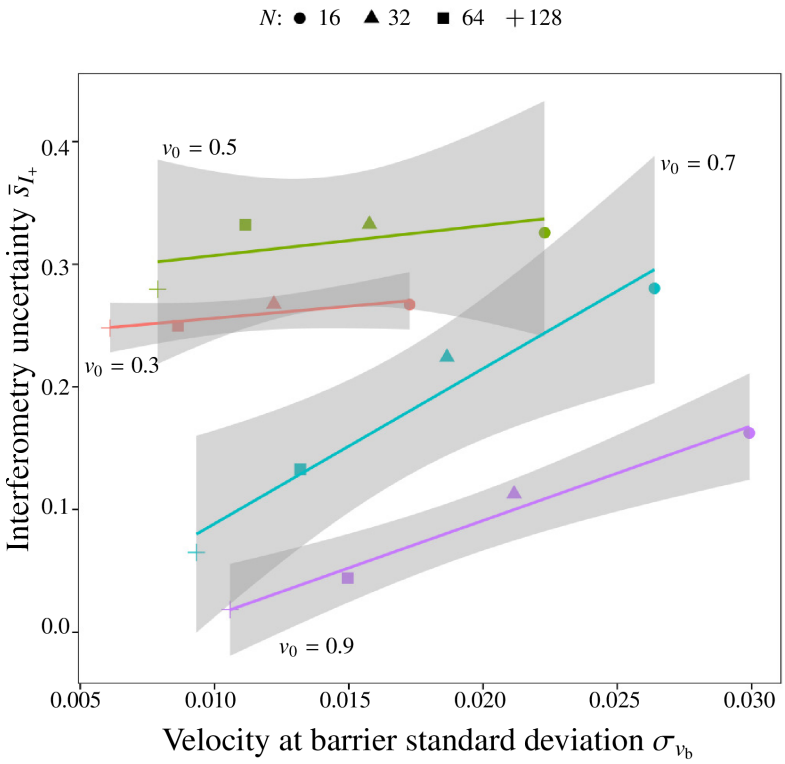

Figure 5.6: Results of Monte-Carlo simulations. Here, the standard deviation associated with the final interferometry distributions depicted in Fig. 5.4. We see a strong, weakly linear dependence on $\bar{s}_{v_b}$ for high v_0, which becomes stronger, but less linear, as we reduce the energy. The variance saturates when the distribution becomes effectively uniform. Reproduced from Ref. [49].

see an approximately linear correlation between the transmission uncertainty and collisional velocity uncertainty standard deviation σ_{v_b}. The gradient of the regression lines is much steeper than those in Fig. 3.6, showing the increased sensitivity of I_+ to quantum fluctuations. Again, the shaded regions show a 95% confidence interval for the linear fit. For all velocities shown the confidence intervals are notably wider than their counterparts in Fig. 3.6, and so we can conclude that the dependence of $\bar{s}_{I_+}$ on σ_{v_b} is more complicated than in the soliton splitting case, as we would expect. At lower velocities $\bar{s}_{I_+}$ saturates below ~ 0.4. This is a result of attempting to fit a Gaussian to a distribution which is, in effect, uniform. This becomes apparent when we consider that $\sim 38\%$ of the probability mass of a Gaussian lies within a central period of width σ, and so applying a fitting algorithm to a uniform distribution will likely produce a standard deviation with a width encompassing $\sim 38\%$ of the sample. In this case, that with is ~ 0.4. This saturation is

a strong indicator of a velocity/particle number regime in which interferometry is unworkable.

5.5 Sagnac interferometry

Our final result will be to explore how the framework of soliton interferometry might be extended to the measurement of the Sagnac effect, first observed in an atom interferometer by Riehle *et al.*[187]. In this experiment the observation manifested as a shift in the Ramsay fringes produced by passing an atomic beam of ^{40}Ca through four travelling waves in a Ramsay excitation geometry, producing an atomic beam interferometer.

The Riehle setup differs from the ideas developed in the current work in two ways. First we have that in Ref. [187] some of the phase information is transported optically. Here we discuss a system where atom-light interactions serve only to coherently split the condensate. Any phase dynamics resulting from these interactions are incidental. Secondly, in the current work we propose a system which results, not in an interference fringe shift, but a population shift between the positive and negative domains of the interferometer. This allows inferences of the Sagnac effect to be drawn from measurements of the particle numbers of the spatially distinct condensates on either side of the barrier, and not the structure of those condensates (which should remain solitonlike).

5.5.1 Physical system

In the case of Sagnac interferometry, we must first slightly alter Eq. (5.5). As we are now working in a moving frame of reference we must transform our spatial coordinate: $x \to x - \Gamma t$. This results in the following dynamical equation in the moving frame

$$i\frac{\partial\psi(x)}{\partial t} = \Bigg[-\frac{1}{2}\frac{\partial^2}{\partial x^2} + i\Gamma\frac{\partial}{\partial x} + \frac{q}{\sigma\sqrt{2\pi}}e^{-x^2/2\sigma^2} + (n_{\mathrm{b}}-1)\frac{q}{\sigma\sqrt{2\pi}}e^{-(x\pm L/2)^2/2\sigma^2} - |\psi(x)|^2 \Bigg]\psi(x). \quad (5.7)$$

Notice that we have gained a translational term and altered the second barrier term. Adding or removing the second barrier allows us to implement two different forms of Sagnac interferometry: one where the solitons both perform a full circumnavigation of the ring, enclosing the area within the ring twice; and one where each soliton

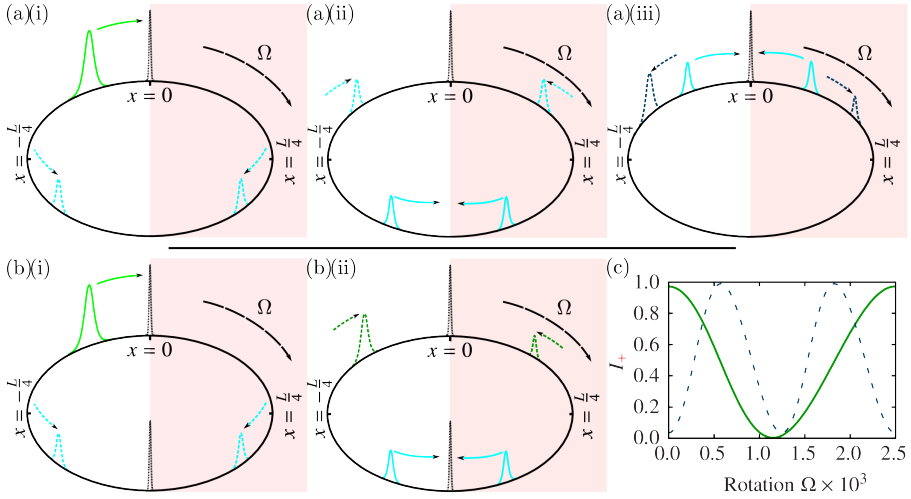

Figure 5.7: Diagram of soliton Sagnac-interferometry. (a) Stages of Sagnac interferometry with one barrier. (b) Sagnac interferometry with two barriers. (c) Interference curves for both the one barrier (green, dashed) and two barrier cases for varying rotational frequency Ω with $L = 40\pi$ and $v = 4$.

circumnavigates a different half of the ring, enclosing the area once. These cases are labelled by the quantity n_b, which is 1 for the first (single barrier) case and 2 for the second (two antipodal barriers) case. As such, the second barrier term is zero for $n_\mathrm{b} = 1$ (illustrated in Figs. 5.7(a) and 5.8(a)) and identical to the other barrier term, up to a spatial offset, for $n_\mathrm{b} = 2$ (illustrated in Figs. 5.7(b) and 5.8(b)). The number of barriers n_b is taken to be 1 or 2 only.

For periodic boundary conditions over the domain $-L/2 < x \leq L/2$ we set $\psi(x) = \psi(x + L)$. This system is comparable to a rotating toroidal trap geometry where L is the dimensionless form of the circumference. Γ can be written in terms of the circumference of the torus L and angular frequency of the rotation Ω. Note that all of these quantities are dimensionless, but we can also write Γ in terms of the dimensional quantities L_D and Ω_D, giving

$$\Gamma = \frac{\Omega L}{2\pi} \tag{5.8}$$

$$= \frac{\hbar}{g_{1\mathrm{D}} N} \frac{\Omega_\mathrm{D} L_\mathrm{D}}{2\pi}. \tag{5.9}$$

where N is the number of particles and $g_{1\mathrm{D}} = 2\hbar\omega_r|a_s|$ (as defined in Chapter 1).

We assume that the wave function has zero amplitude at the location of splitting potentials, and so we always take $\psi(0) = 0$. This allows for a discontinuous phase

in the presence of splitting potentials, and is exact in the $\sigma \to 0$ limit, where the Gaussian profile becomes a δ-function.

The soliton solution to Eq. (5.7) (in the absence of splitting potentials and periodic boundary conditions) is obtained by the Galilean invariance of the standard soliton profile [20]. We begin with the invariant solution

$$\tilde{\psi}(\tilde{x},t) = D\mathrm{sech}\left(D\left[\tilde{x} - Vt\right]\right)\exp\left\{iV\tilde{x} + i\left(D^2 - V^2\right)t/2\right\}, \tag{5.10}$$

where the tilde notation denotes the stationary frame of reference. A soliton moving with velocity v in a frame moving with velocity Γ is moving at velocity $V = v + \Gamma$ in the stationary frame, and so we obtain

$$\tilde{\psi}(\tilde{x},t) = D\mathrm{sech}\left(D\left(\tilde{x} - [v+\Gamma]t\right)\right)\exp\left\{i[v+\Gamma]\tilde{x} + i\left(D^2 - [v+\Gamma]^2\right)t/2\right\}. \tag{5.11}$$

Transferring to the moving frame, where $x = \tilde{x} - \Gamma t$, we obtain

$$\psi(x,t) = D\mathrm{sech}(D[x - vt])\exp\left\{i[v+\Gamma][x+\Gamma t] + i\left(D^2 - [v+\Gamma]^2\right)t/2\right\}. \tag{5.12}$$

This retrieves a result obtained by the analysis presented in Appendix A. A more general result, valid for periodic boundary conditions, is also presented in Appendix A [Eq. (A.60)], however we assume that $L \gg 1$ and so Eq. (5.12) can be taken as a valid solution to Eq. (5.7).

5.5.2 Process

We will now outline the process of soliton Sagnac-interferometry, which has three steps. This process is common to both the $n_\mathrm{b} = 1$ and $n_\mathrm{b} = 2$ configurations. The phase evolution of the system will later be analysed in full.

First, a ground state soliton is split into two secondary solitons of equal size at a narrow potential barrier (Fig. 5.7(a)(i) and (b)(i), time T_s in Fig. 5.8). An equal split is obtained by selecting the barrier's strength q for a given incident velocity and barrier width σ. As discussed previously (Sec. 3.4.6), this splitting event causes a phase difference to arise between the solitons.

In the second step these secondary solitons accumulate a further relative phase-difference. This phase difference is the quantity we wish to measure and is gained as a result of the differing path lengths travelled by counter propagating waves in a moving frame (Fig. 5.7(a)(ii) and (b)(i)-(ii), time $T_\mathrm{s} < t < T_\mathrm{c}$ in Fig. 5.8). This

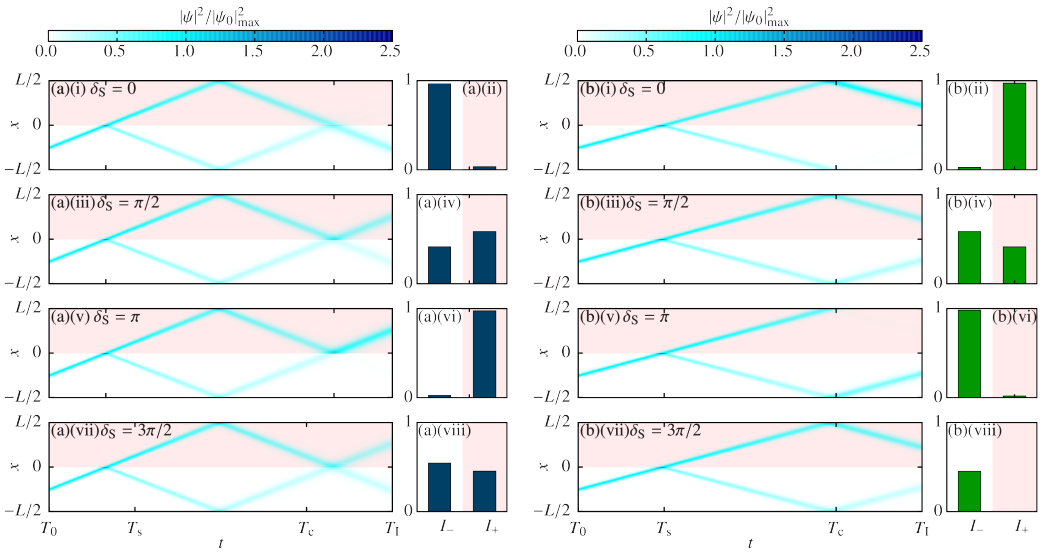

Figure 5.8: Overview of a Sagnac interferometry. (a) The one barrier case. (b) The two barrier case. For both cases the velocity was $v = 4$

phase shift will be denoted as δ_S and is dependent on the frequency of rotation and path length travelled by the solitons.

In the third step the two solitons are made to collide at a narrow barrier (Fig. 5.7(a)(iii) and (b)(ii), time T_c in Fig. 5.8). After this final barrier collision the wavefunction integrals on either side of the barrier [Eq. (5.3)] allow us to determine the magnitude of δ_S [48, 49]. Again, I_+ is the positive domain population and I_- is the negative domain population.

5.5.3 Analysis of phase evolution

The three steps outlined above each introduce phase dynamics to the system. In this section we will describe these dynamics more fully in order to determine how the Sagnac effect arises in GPE soliton interferometry.

After the initial split at time T_s the soliton in the positive domain has peak phase $\phi_+(t)$, while that in the negative domain has peak phase $\phi_-(t)$. Here we wish to determine the phase difference between the two solitons before they collide with one-another at a barrier at time T_c. This is denoted as

$$\Delta = (-1)^{n_b}(\phi_+(T_c) - \phi_-(T_c)). \tag{5.13}$$

The prefactor $(-1)^{n_b}$ changes the sign of the phase difference to account for the fact that the solitons will approach the collisional barrier from different directions

depending on the number of barriers. For all values of n_b we have $T_s = L/4v$. For $n_b = 1$ the solitons created by the splitting event must both fully circumnavigate the periodic domain before colliding at a barrier, while for $n_b = 2$ the solitons must only travel half the x-domain, and so $T_c = T_s + L/n_b v$.

The first step, in which the initial soliton is split on the narrow barrier, creates our two solitons of equal amplitude. In the case of a δ-function barrier this split causes the transmitted soliton to be phase shifted by $\pi/2$ ahead of the reflected soliton, as determined analytically in Section 3.4.6 [49]. We will use this figure as an estimate of the phase difference accumulated by splitting on a Gaussian barrier, as justified in Section 3.3.2 [48]. A discussion of phase shifts accumulated by finite width barriers is available in Ref. [169]. We select a Gaussian profile for the barrier as this is standard for typical experimental setups [34]. As such we take

$$\phi_+(T_s) = \phi_-(T_s) + \pi/2 \tag{5.14}$$

The evolution of the phase at the peak of an individual soliton is obtained by taking the imaginary part of the exponent of Eq. (5.12) and setting $x = vt$, giving

$$\phi_s(t; v) = \left(D^2 + [\Gamma + v]^2\right) t/2 \tag{5.15}$$

up to an arbitrary initial offset. We can use this equation with Eq. (5.14) to write

$$\begin{aligned} \phi_-(t) &= \phi_s(t - T_s; -v) \\ &= \left(D^2 + [\Gamma - v]^2\right) \frac{(t - T_s)}{2} \end{aligned} \tag{5.16}$$

$$\begin{aligned} \phi_+(t) &= \phi_s(t - T_s; v) + \frac{\pi}{2} \\ &= \left(D^2 + [\Gamma + v]^2\right) \frac{(t - T_s)}{2} + \frac{\pi}{2}. \end{aligned} \tag{5.17}$$

We can now write Δ as

$$\begin{aligned} \Delta &= (-1)^{n_b} \left\{ \phi_s(T_c - T_s; v) + \frac{\pi}{2} - \phi_s(T_c - T_s; -v) \right\} \\ &= (-1)^{n_b} \left\{ \left([\Gamma + v]^2 - [\Gamma - v]^2 \right) \frac{(T_c - T_s)}{2} + \frac{\pi}{2} \right\} \\ &= (-1)^{n_b} \left\{ (4\Gamma v) \frac{L}{2 n_b v} + \frac{\pi}{2} \right\} \\ &= (-1)^{n_b} \left\{ \frac{2\Gamma L}{n_b} + \frac{\pi}{2} \right\} \end{aligned} \tag{5.18}$$

It is also true that in the absence of the second barrier ($n_b = 1$) the solitons will collide with one another at the point antipodal to the splitting barrier situated at $x = 0$. As this antipodal collision occurs in the absence of any axial potentials or barriers the solitons remain topologically stable and are unaffected beyond asymptotic shifts to position and phase (Chapter 2) [20, 167]. These asymptotic shifts are given by the two soliton case of Eq. (2.40),

$$D_j \delta x_j + i\delta\phi_j = (-1)^k \ln\left[\frac{D_j + D_k + i(v_j - v_k)}{D_j - D_k + i(v_j - v_k)}\right], \tag{5.19}$$

where $j, k = \{1, 2\}$ and $j \neq k$. The quantities δx_j and $\delta\phi_j$ are the asymptotic position and phase shifts associated with the jth soliton, while v_j and D_j describe that soliton's velocity and normalisation. Taking the soliton which is transmitted through the barrier at time T_s to be associated with $j, k = 1$ we obtain the correct sign for our asymptotic shifts.

In our case, by noting that $D_1 = D_2 = 1/4$ we can determine the relative phase shift which arises as a result of this collision:

$$\begin{aligned}
\phi_C &= \delta\phi_2 - \delta\phi_1, \\
&= -\operatorname{Im}\left(\ln\left[\frac{1 + 2i\left[(v) - (-v)\right]}{2i\left[(v) - (-v)\right]}\right] + \ln\left[\frac{1 + 2i\left[(-v) - (v)\right]}{2i\left[(-v) - (v)\right]}\right]\right), \\
&= \operatorname{Im}\left(\ln\left[\frac{16v^2}{16v^2 + 1}\right]\right), \\
&= 0
\end{aligned} \tag{5.20}$$

As such, ϕ_C does not need to be included in the calculation of Δ.

Similarly, we can consider the positions shifts δx_j

$$\begin{aligned}
D_j \delta x_j &= (-1)^k \operatorname{Re}\left(\ln\left[\frac{1 + (-1)^k i4v]}{(-1)^k i4v}\right]\right) \\
&= (-1)^k \operatorname{Re}\left(\ln\left[1 - i\frac{(-1)^k}{4v}\right]\right) \\
&= \frac{(-1)^k}{2} \ln\left[1 + \frac{1}{16v^2}\right] \qquad (5.21) \\
&= -D_k \delta x_k. \qquad (5.22)
\end{aligned}$$

Both results pertaining to the asymptotic position and phase shifts use the standard complex logarithmic identity $\ln(z) = 1/2 \ln(|z|^2) + i \arg(z)$

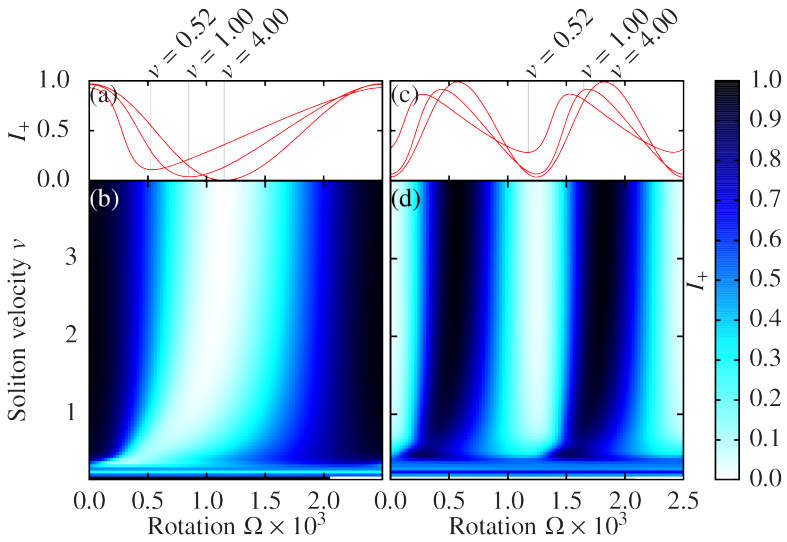

Figure 5.9: Numerically calculated transmission rates after the second collision, I_+, for two Sagnac interferometry geometries. Color-maps for the (b) $n_b = 2$ and (d) $n_b = 1$ cases show the $0.16 < v < 4$, $0 < \Omega \times 10^3 < 2.5$ parameter space. Panels (a) and (c) show specific curves of constant v for these scenarios respectively and highlight how the different interrogation times result in a different Sagnac phase accumulation. The phase difference is varied by varying Ω with $L = 40\pi$.

Equation (5.21) shows us that $\delta x_j \to 0$ quickly as $v \to \infty$, while Eq. (5.22) shows us that whatever the size of the asymptotic position shift, the solitons are always shifted by equal amounts in opposite directions, and so will always meet at the collisional barrier situated at $x = 0$.

These results [Eqs. (5.20), (5.21), and (5.22)] tell us that the antipodal collision in the absence of a barrier does not affect the outcome of Sagnac interferometry if we assume that the solitons' accelerations during the collision do not affect the Sagnac phase accumulation. The analysis supporting this assumption is beyond the scope of the current work but can be verified numerically.

We can now determine $I_\pm$ by recalling previous results Chapter 4, namely Eqs. (4.13) and (4.14) [48]. Following the same procedure outlined in Section 5.2 [substituting Eq. (5.18) into Eq. (4.13)] we obtain

$$I_\pm = \frac{1 \pm (-1)^{n_b} \cos(\delta_S - \epsilon)}{2}, \tag{5.23}$$

where $\epsilon \to 0$ as $v \to \infty$ and is sufficiently small for $v \gtrsim 2$; and δ_S is the Sagnac

phase we wish to measure and is given by

$$\begin{aligned}\delta_{\mathrm{S}} &= \frac{2\Gamma L}{n_{\mathrm{b}}} \\ &= \frac{\Omega L^2}{\pi n_{\mathrm{b}}} \\ &= \frac{m}{\hbar}\frac{\Omega_{\mathrm{D}} L_{\mathrm{D}}^2}{\pi n_{\mathrm{b}}}.\end{aligned} \tag{5.24}$$

5.5.4 Numerical verification

Results of numerical simulations are shown in Fig. 5.9(a–b). We see that for very high velocities, $v \approx 4$, the interference follows our prediction [Eq. (5.23)] closely, with very small skews arising from nonlinear effects during the final barrier collision, showing that $\epsilon \approx 0$ in this regime. The $n_{\mathrm{b}} = 1$ (c–d) and $n_{\mathrm{b}} = 2$ (a–b) have similar structures, however for $n_{\mathrm{b}} = 1$ the phase varies twice as quickly. This is consistent with our predictions. The similarity of the structures supports the assumption that accelerations during barrier free collisions do not affect the Sagnac effect phase accumulation.

As we reduce the velocity, and the necessary assumption of high initial kinetic energy breaks down, our numerics show that our results no longer hold, and so we conclude that Sagnac interferometry is not practicable in the $v \lesssim 1$ regime. This is consistent with previous work by the authors [49] which delimited this regime as the high-to-low energy transitional regime. Furthermore, the results shown here are comparable to those obtained for the Mach–Zehnder configuration [Fig. 5.2].

Chapter 6: Conclusions

In this thesis we have covered the three major components of the theory of soliton interferometry.

First we developed the theory of soliton splitting on Gaussian barriers, and compared this to the ideal case of the δ-function barrier. We found that for sufficiently narrow barriers the behaviour was comparable between the two barrier structures but for finite width barriers there was an upper limit to the allowed incident velocity, above which classical transmission dominated. We then probed different energetic regimes in the classical system, and found that at low energies the classical approach became highly sensitive to uncertainty in the initial condition consistent with quantum mechanical fluctuations. This low energy regime failure of classical results is primarily caused by disallowed soliton splitting events, extremely discontinuous transmission curves, and bound states. We also provided analysis to determine the phase difference between the outgoing solitons after the split.

Secondly we presented a general and detailed analysis of the collision of two fast-moving bright solitons at a narrow potential barrier. We have developed an analytic treatment of this problem, based on the assumption of a δ-function potential and short collision times. Our numerical simulations of the same problem revealed that this analytic treatment is quantitatively accurate in the limit of narrow barriers and fast solitons. At realistic soliton speeds and barrier widths, however, our numerical results differ from the analytic prediction; we have quantified this in terms of the phase-skew ϵ which tends to zero as the incident velocity increases. Our analytic treatment also provides an estimate of the regimes in which the outgoing waves contain solitons.

Finally we have shown analytic results describing soliton interferometry in the ideal classical case, specifically the cases of a Mach–Zehnder configuration and a Sagnac configuration. We have extended the Mach–Zehnder results to the harmonically trapped system, which is currently more experimentally relevant than the toroidal case [34] and presents a better defined situation when considering quantum fluctuations of the COM. This has allowed us to investigate and delimit the energetic regimes in which quantum fluctuations in the initial COM position and momentum cause the classical dynamics to break down.

The breakdown of the classical model in the low energy regime complicates the early evolution of the interferometric system and compromises the dynamics. As we approach the low energy regime quantum effects mix these phenomena into the dynamics of the system where classically they would be absent. This causes greatly enhanced sensitivity to quantum effects in both the splitting transmission and the interferometry transmission when close to the low energy regime. This sensitivity appears at marginally higher kinetic energies in the presence of harmonic trapping, but the difference is relatively slight for the weak trapping considered.

We conclude that whether or not the mean-field limit is truly achieved, soliton interferometry is not a viable process in the extremely, or even transitionally, low kinetic energy regime. However, for a suitably high initial kinetic energy we see good results for particle numbers upwards of the low hundreds (beyond which our numerical algorithm struggles to resolve fluctuations, also indicating that the classical model is robust in this regime), and so conclude that soliton interferometry is viable given a suitably high-energy and effectively classical regime.

Appendix A: Travelling wave solutions to the translational focusing NLSE

In this appendix we provide a more meticulous derivation of travelling wave solutions in the translational NLSE. We begin with the NLSE with a negative (focusing) nonlinearity.

$$iu_t = -\frac{u_{xx}}{2} - u|u|^2 \tag{A.1}$$

If we now change our spatial coordinate to one moving to the right at speed γ, i.e. $x \to x - \gamma t$, we obtain

$$iu_t = -\frac{u_{xx}}{2} + i\gamma u_x - u|u|^2 \tag{A.2}$$

We now consider all calculations within this moving frame, and so if we consider a solitary wave moving to the right at speed c in this frame we are, in fact, considering a wave moving at speed $c - \gamma$. Note that for $\gamma = 0$ we retrieve results valid in the stationary frame, as outlined in Chapter 2.

We now seek travelling wave solutions under the *ansatz* suggested in Ref. [159],

$$u = re^{i(\theta+\mu t)}. \tag{A.3}$$

We set r and θ to be functions of the variable $\xi = x - ct$, while μ is a constant chemical potential. We also assert that r and θ are real (preventing exponential growth or decal in the full solution, which would be incompatible with our requirement of a stabe profile) and note that $|r|^2$ must be ≥ 0 for a meaningful solution. For clarity we will consider each derivative individually:

$$u_t = -cr'e + ire(-c\theta' + \mu) \tag{A.4}$$

$$u_x = r'e + ir\theta'e \tag{A.5}$$

$$u_{xx} = r''e + ir'\theta'e + ir'\theta'e - r(\theta')^2e + ir\theta''e \tag{A.6}$$

$$|u|^2u = r^3e \tag{A.7}$$

where the prime denotes a partial derivative and e denotes the exponential term

$\exp i(\theta + \mu t)$ and is reduced for brevity. Now, going term by term we obtain

$$iu_t = cr\theta' e - \mu re - icr' e \tag{A.8}$$

$$-\frac{u_{xx}}{2} = -\frac{r'' e}{2} - ir'\theta' e + \frac{r(\theta')^2 e}{2} - \frac{ir\theta'' e}{2} \tag{A.9}$$

$$i\gamma u_x = i\gamma r' e - \gamma r\theta' e \tag{A.10}$$

$$-|u|^2 u = -r^3 e \tag{A.11}$$

or, dropping the global factor of e,

$$cr\theta' - \mu r - icr' = -\frac{r''}{2} - ir'\theta' + \frac{r(\theta')^2}{2} - i\frac{r\theta''}{2} + i\gamma r' - \gamma r\theta' - r^3. \tag{A.12}$$

This equation can now be split into real and imaginary parts:

$$\text{Im(A.12)} \qquad -cr' = -r'\theta' - \frac{r\theta''}{2} + \gamma r', \tag{A.13}$$

$$\text{Re(A.12)} \qquad cr\theta' - \mu r = -\frac{r''}{2} + \frac{r(\theta')^2}{2} - \gamma r\theta' - r^3. \tag{A.14}$$

Beginning with the imaginary part, rearranging Eq. (A.13) and multiplying by r gives us

$$rr'\theta' + \frac{r^2\theta''}{2} = (c + \gamma)rr', \tag{A.15}$$

which integrates to give us

$$\theta' = (c + \gamma) + \frac{A}{r^2}, \tag{A.16}$$

where A is a real constant of integration.

Now, taking the real part we rearrange Eq. (A.14) to get

$$(c + \gamma)r\theta' - \mu r + \frac{r''}{2} - \frac{r(\theta')^2}{2} + r^3 = 0. \tag{A.17}$$

Substituting Eq. (A.34) into this equation and setting $\beta = c + \gamma$ we obtain

$$\beta r\left(\frac{A}{r^2} + \beta\right) - \mu r + \frac{r''}{2} - \frac{r}{2}\left(\frac{A}{r^2} + \beta\right)^2 + r^3 = 0. \tag{A.18}$$

Simplifying, multiplying by r' and setting

$$\alpha = 2\mu - \beta^2 \tag{A.19}$$

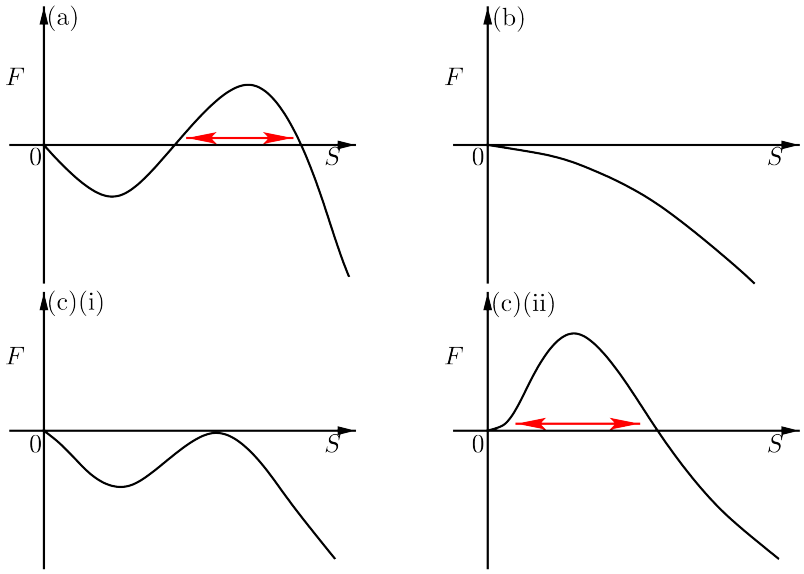

Figure A.1: Reproduced from Chapter 2. Here we see that the polynomial $F(S)$ can satisfy one of three cases: (a) three single roots, (b) one triple root and (c) one double root and one single root.

gives us

$$-\frac{\alpha r r'}{2}+\frac{r' r''}{2}-\frac{A^2 r'}{2r^3}+r' r^3=0. \tag{A.20}$$

This integrates immediately and, after multiplication by $4r^2$, becomes

$$-\frac{\alpha r^2}{4}+\frac{(r')^2}{4}+\frac{A^2}{4r^2}+\frac{r^4}{4}=B. \tag{A.21}$$

We now re-write $r(\xi)$ in terms of the density $S(\xi)=r^2$, with $(rr')^2=(S')^2/4$, and rearrange to give

$$(S')^2=4\left(-S^3+\alpha S^2+4BS-A^2\right). \tag{A.22}$$

When $S=0$ we see that $S'=i2A$. As we have stated that S is a real function we conclude that $A=0$, and so

$$(S')^2=4\left(-S^3+\alpha S^2+4BS\right). \tag{A.23}$$

$$\equiv 4G(S) \tag{A.24}$$

Furthermore, if we consider the asymptotic behaviour as $S\to\infty$ we can determine the structure of G to follow one of four forms (see Fig. A.1, reproduced from Chapter 2).

From the requirement that S be real (and so S' is real, meaning $G > 0$) we can discard Fig. A.1(b) and (c)(i). This leaves us with Fig. A.1(a) and (b)(ii). In order to better understand these two cases we must discuss exactly how S depends on ξ. This is achieved by solving Eq. (A.24) in the region of specific roots of G. In the two remaining cases these roots are either single or double.

Single roots: In the region of a single root $S_1 = S(\xi_1)$ we can Taylor expand G about S_1 to obtain

$$(S')^2 = 4\left[(S - S_1)\,G'(S_1) + O\left([S - S_1]^2\right)\right]. \tag{A.25}$$

Here the O notation signifies "terms of the order of". This equation can be integrated to give the solution

$$S = S_1 + (\xi - \xi_1)^2\,G'(S_1) + O\left([\xi - \xi_1]^3\right) \tag{A.26}$$

in the region of S_1. As such, a single zero in G indicates a feature where $S(\xi_1)$ is extremal. This means that as we monotonically vary ξ, S increases/decreases (depending on the sign of $G'[S_1]$) towards S_1, becomes S_1 for $\xi = \xi_1$, and then decreases/increases away from S_1 as we continue to vary ξ.

Double roots: our Taylor expansion now yields

$$(S')^2 = 4\left[(S - S_1)^2\,G''(S_1) + O\left([S - S_1]^3\right)\right]. \tag{A.27}$$

Again, this can be integrated immediately with solutions of the form [159]

$$S - S_1 \propto \exp\left[\pm\{G''(S_1)\}^{1/2}\,\xi\right] \qquad \text{as } \mp\xi \to \infty \tag{A.28}$$

for bounded solutions. As such, we see that a double zero in G indicates a feature where $S(\xi_1)$ is an asymptotic value for large ξ.

Considering these behaviours in the context of the remaining parts of Fig. A.1, panels (a) and (c)(ii), we see that: (a) contains a solution which continually oscillates between the two single roots of G, S_1 and S_2; while (c)(ii) contains a solution which asymptotes from 0 at $\xi \to -\infty$ to $S = S_1$ and then back to 0 for $\xi \to \infty$. While the case of a)'s periodic surface waves is a valid solution to the NLSE, it does not have a finite norm for unbounded ξ. We will now focus on the case of (c)(ii), our solitary translating wave.

In this scenario, setting $r, r' \to 0$ as $\xi \to \pm\infty$ in (A.24), which is true for a solitary wave profile, we determine that $B = 0$. Note that this result only holds true for $(S')^2/S \to 0$ as $\xi \to \pm\infty$ which we will justify later. Equation (A.24) now has the form

$$(S')^2 = 4\left(-S^2(S-\alpha)\right) \tag{A.29}$$

This can be rearranged to the integral

$$\int \frac{dS}{2S\,(\alpha - S)^{1/2}} = \int d\xi. \tag{A.30}$$

This integral is solved by the substitution $S = \alpha \mathrm{sech}^2(\eta)$, where η is a function of ξ, giving

$$\int \frac{-2\alpha \mathrm{sech}^2(\eta)\tanh(\eta)}{2\alpha^{3/2}\mathrm{sech}^2(\eta)\left(1-\mathrm{sech}^2(\eta)\right)^{1/2}} d\eta = \int d\xi, \tag{A.31}$$

which simplifies to

$$\int -\alpha^{-1/2} d\eta = \int d\xi, \tag{A.32}$$

determining $\eta = -\alpha^{1/2}(\xi - \xi_0)$, where ξ_0 arises as a constant of integration but is simply an initial offset. Noting that sech is symmetric about zero and requiring $r(\xi) \geq 0$, this gives us

$$r(\xi) = \alpha^{1/2}\mathrm{sech}(\alpha^{1/2}[\xi - \xi_0]). \tag{A.33}$$

Note that this solution also satisfies $(S')^2/S \to 0$ as $\xi \to \pm\infty$, justifying our previous selection.

If we now recall Eq. (A.34) and apply the $A = 0$ condition. This equation for the phase now immediately integrates to give

$$\theta(\xi) = \beta\xi, \tag{A.34}$$

and so, via Eq. (A.19), we obtain

$$u(\xi) = \alpha^{1/2}\mathrm{sech}(\alpha^{1/2}[\xi - \xi_0]) \exp\left[i\beta\xi + i\left(\alpha + \beta^2\right)t/2\right]. \tag{A.35}$$

Finally, we might impose the normalisation

$$\int |u|^2 d\xi = 2D \tag{A.36}$$

which is consistent with the N-particle GPE for $N = 2D$. This determines $\alpha = D^2$

and gives us

$$u(x,t;c,\gamma) = D\text{sech}(D[x-ct]) \times \exp\left\{i[c+\gamma][x-ct] + i\left(D^2 + [c+\gamma]^2\right)t/2\right\} \quad \text{(A.37)}$$

which is equivalent to

$$u(x,t;c,\gamma) = D\text{sech}(D[x-ct]) \times \exp\left\{i[c+\gamma][x+\gamma t] + i\left(D^2 - [c+\gamma]^2\right)t/2\right\}. \quad \text{(A.38)}$$

For $\gamma = 0$ this reduces to

$$u_{\mathrm{G}}(x,t) = D\text{sech}(D[x-ct])\exp\left\{icx + i\left(D^2 - c^2\right)t/2\right\}, \quad \text{(A.39)}$$

which is exactly the standard J. P. Gordon soliton solution [20].

We can retrieve Eq. (A.37) from the more general case were we have three roots at $0, S_1$ and S_2 where $S_1 < S_2$ and S_1 may or may not be zero. This covers both cases (a) and (c)(ii) of Fig. A.1. From Eq. (2.33) we can see that

$$\int_S^{S_2} \frac{d\tilde{S}}{2\left\{G(\tilde{S})\right\}^{1/2}} = \pm\int_{\xi}^{\xi_2} d\tilde{\xi}, \quad \text{(A.40)}$$

where tildes denote dummy integration variables. From the structure of G in Eq. (A.24) we can write

$$G(S) = -S(S-S_1)(S-S_2), \quad \text{(A.41)}$$

and in the region between S_1 and S_2 we can write

$$S = S_2 - (S_2 - S_1)\sin^2(\zeta) \quad \text{(A.42)}$$

$$= S_2\left(1 - m\sin^2(\zeta)\right) \quad \text{(A.43)}$$

where ζ is a parameter which varies S between S_1 and S_2 (and will prove to be another a dummy integration variable) and

$$m = \frac{S_2 - S_1}{S_2}. \quad \text{(A.44)}$$

Substituting equations (A.41) and (A.42) into integral (A.40) we obtain

$$\pm S_2^{1/2}(\xi_2 - \xi) = \int_0^{\zeta} \frac{d\tilde{\zeta}}{\left(1 - m\sin^2(\tilde{\zeta})\right)}. \tag{A.45}$$

This integral is solved in terms of Jacobi elliptic functions [188]. We use dn$[x|m]$, which is a function of x and has parameter m, and gives

$$\mathrm{dn}[S_2^{1/2}\xi|m] = \sqrt{1 - m\sin^2(\zeta)} \tag{A.46}$$

as a solution to Eq. (A.45), noting that ξ_2 is an arbitrary offset and dn is symmetric about its argument. Substituting this into Eq. (A.43) we obtain

$$S(\xi) = S_2 \mathrm{dn}^2\left[S_2^{1/2}\xi\middle|m\right], \tag{A.47}$$

The dn function describes a bulk condensate with surface waves. The period of these waves can be described in terms of the complete elliptic integral of the first kind, and is 2K(m). As such the domain $0 \leq \xi \leq 2nK(m)/S_2^{1/2}$ will contain n surface waves (i.e. n peaks), and we can integrate over this region to obtain

$$\int_0^{2nK(m)/S_2^{1/2}} S(\xi)d\xi = S_2^{-1/2} \int_0^{2n\mathrm{K}(m)} S(\xi)d\hat{\xi} \tag{A.48}$$

$$= S_2^{1/2} \int_0^{2n\mathrm{K}(m)} \mathrm{dn}^2[\hat{\xi}|m]d\hat{\xi} \tag{A.49}$$

$$= 2S_2^{1/2} nE(m). \tag{A.50}$$

Here we used a change of variable $\hat{\xi} = S_2^{1/2}\xi$ and refer the reader to Abramowitz and Stegun [188] for results pertaining to the integrals of squared Jacobi elliptic functions. The result is expressed in terms of the complete elliptic integral of the second kind $E(m)$, also described in Ref. [188].

Again asserting that the number of particles in the region considered is $2D$, we determine S_2 to be

$$S_2 = \left(\frac{D}{nE(m)}\right)^2, \tag{A.51}$$

now expressed in terms of m and n alone. This fully determines the amplitude of $u(\xi)$, and so we now move on to the phase. As before, $A = 0$ and so Eq. (A.34) still applies. This leaves us to determine the chemical potential in terms of m and n. To achieve this we must first determine our roots S_1 and S_2 in terms of μ and β, and so we consider Eq. (A.24). Setting $S' = 0$ for our roots, and discarding the trivial

$S = 0$ solution, we obtain

$$S^2 - \alpha S - 4B = 0 \tag{A.52}$$

which has roots

$$S_\pm = \frac{\alpha \pm \sqrt{\alpha + 16B}}{2} \tag{A.53}$$

As α and B are real, recalling that $S_2 > S_1$ we see that the positive (negative) sign corresponds to S_2 (S_1). Taking the sum of the roots we obtain

$$\begin{aligned} S_1 + S_2 &= \alpha \\ &= 2\mu - \beta^2 \end{aligned} \tag{A.54}$$

by Eq. (A.19), and so

$$\mu = \frac{(S_1 + S_2) + \beta^2}{2} \tag{A.55}$$

Rearranging Eq. (A.44) and combining Eq. (A.51) we see

$$S_1 = (1 - m)\left(\frac{D}{nE(m)}\right)^2, \tag{A.56}$$

and so

$$\mu = \frac{\left[p(m,n)D^2 + (c+\gamma)^2\right]}{2}, \tag{A.57}$$

where we define $p(m,n)$ as

$$p(m,n) = \frac{2-m}{[nE(m)]^2}. \tag{A.58}$$

Combining these results, we can construct our general n-travelling-wave solution

$$\begin{aligned} u(x,t;m,n,c,\gamma) = &\frac{D}{nE(m)}\mathrm{dn}\left(\frac{D}{nE(m)}[x-ct]\right) \\ &\times \exp\left\{i[c+\gamma][x-ct] + i\left(p(m,n)D^2 + [c+\gamma]^2\right)t/2\right\}. \end{aligned} \tag{A.59}$$

which is equivalent to

$$\begin{aligned} u(x,t;m,n,c,\gamma) = &\frac{D}{nE(m)}\mathrm{dn}\left(\frac{D}{nE(m)}[x-ct]\right) \\ &\times \exp\left\{i[c+\gamma][x+\gamma t] + i\left(p(m,n)D^2 - [c+\gamma]^2\right)t/2\right\}. \end{aligned} \tag{A.60}$$

As we send $S_1 \to 0$ we see that $m \to 1$. In this limit we note that $K(m) \to \infty$

(complex infinity) and $E(1) = 1$. The period of $dn[x|m]$ is $2K(m)$ and so in the $S_1 \to 0$ limit the period becomes infinite and only a single travelling wave exists on the real line. This can also be seen from the fact that $\mathrm{dn}[x|1] = \mathrm{sech}(x)$. With only a single travelling wave we have $n = 1$ and so for $S_1 = 0$ we have $p(1, 1) = 1$; the bulk condensate disappears and Eq. (A.60) retrieves Eq. (A.38). This is as we would expect. Similarly, for $\gamma = 0$ Eq. (A.60) is equivalent to work presented by Carr *et al.* in Ref. [189] (although here we have adopted a different method of normalisation).

Appendix B: Notes on the numerical method

Many of the results presented in this thesis were numerical in nature. Here we will briefly outline the technique used in the most computationally demanding method (the split-step pseudo-spectral GPE solver) and describe an aspect of this numerical technique (the treatment of the δ-function barrier) the numerical implementation of which was not discussed elsewhere (although see also relevant theoretical results in Ref. [190]).

Here we choose to decompose the wave function $\psi(x,t)$ into a plane wave (Fourier) basis[1]. From a mathematical point of view we are representing our wave function in momentum space as a Fourier series

$$\psi(x,t) = \sum_{k=-\infty}^{\infty} c_k(t) e^{2\pi i k x/L} \tag{B.1}$$

where the complex amplitudes $c_k(t)$ are given by

$$c_k(t) = \frac{1}{L}\int_{-L/2}^{L/2} \psi(x,t) e^{-2\pi i k x/L} dx \tag{B.2}$$

over the finite $-L/2 < x \leq L/2$ domain. This implicitly requires periodic boundary conditions. In terms of the numerical algorithm, we discretise our spatial grid to N regularly spaced points and restrict our plane wave basis to N modes, truncating the Fourier series. This is a simpler example of Gaussian quadrature, which generally requires a more complex selection of the spatial grid as prescribed by the basis. The basis also generally requires specific weight functions for orthonormality. For plane waves the grid spacing is merely regular intervals and the weight function is 1. As such, the definitive FFTW library [191] computes

$$c_k(t) = a_\mathrm{f} \sum_{n=0}^{N-1} \psi_n(t) e^{2\pi i n k/N} \tag{B.3}$$

$$= a_\mathrm{f} \sum_{n=0}^{N-1} \psi_n(t) e^{2\pi i n x_k/L} \tag{B.4}$$

[1] A more general analysis for arbitrary bases is available in Appendix B of Ref [59].

for the forward transform and

$$\psi_k(t) = a_\mathrm{b} \sum_{n=0}^{N-1} c_n(t) e^{-2\pi i n k/N} \tag{B.5}$$

$$= a_\mathrm{b} \sum_{n=0}^{N-1} c_n(t) e^{-2\pi i n x_k/L} \tag{B.6}$$

for the backward transform, where $\psi_k(t) = \psi(x_k, t)$ and $x_k = kL/N$. Note that the norm-preserving rescaling prefactors a_f and a_b are not contained within the FFTW algorithms and must be applied manually. This is because in the absence of an exact physical interpretation the transform normalisation is somewhat arbitrary. Applying both the forward and backward transforms effectively multiplies the wave function by N and so we require that $a_\mathrm{f} a_\mathrm{b} = 1/N$

This choice of grid replaces the conversion from a discrete spatial basis to a truncated momentum basis by multiplication by the matrix A which satisfies

$$\boldsymbol{c}(t) = A\boldsymbol{\psi}(t). \tag{B.7}$$

Similarly, the reverse transform matrix B satisfies

$$\boldsymbol{\psi}(t) = B\boldsymbol{c}(t). \tag{B.8}$$

Comparing equations Eqs. (B.7) and (B.8) with Eqs. (B.4) and (B.6), we see that the matrix elements are

$$A_{jk} = a_\mathrm{f} e^{2\pi i j x_k/L} \tag{B.9}$$

$$B_{jk} = a_\mathrm{b} e^{-2\pi i j x_k/L}. \tag{B.10}$$

Considering

$$(AB)_{jk} = a_\mathrm{f} a_\mathrm{b} \sum_{n=0}^{N-1} e^{2\pi i (j-k) x_n/L} \tag{B.11}$$

$$= \delta_{jk}, \tag{B.12}$$

where the last step can be determined from the orthogonality of the plane wave basis, we see that $B = A^{-1}$.

We now consider the dynamical equation (the GPE)

$$i\frac{\partial\psi}{\partial t} = \left\{-\frac{1}{2}\frac{\partial^2}{\partial x^2} + q\delta(x - x_0) - |\psi|^2\right\}\psi \tag{B.13}$$

describing an untrapped system with a δ-function barrier at x_0. This equation can be split into linear and nonlinear operators

$$i\frac{\partial\psi}{\partial t} = \{\mathcal{R}(x) + \mathcal{N}[\psi(x,t)]\}\,\psi \tag{B.14}$$

where the operators are

$$\mathcal{R}(x) = -\frac{1}{2}\frac{\partial^2}{\partial x^2} + q\delta(x - x_0) \tag{B.15}$$

$$\mathcal{N}[\psi(x,t)] = -|\psi|^2. \tag{B.16}$$

We can write the approximate solution to this equation in the discrete basis as

$$\boldsymbol{\psi}(t+\delta t) = e^{-i\mathcal{N}[\boldsymbol{\psi}(t)]\delta t/2}e^{-i\mathcal{R}\delta t}e^{-i\mathcal{N}[\boldsymbol{\psi}(t)]\delta t/2}\boldsymbol{\psi}(t) \tag{B.17}$$

where $\mathcal{R}$ and $\mathcal{N}$ are now matrix operators. Splitting the nonlinear operation in this way incorporates some of the nonlinearity into the linear operation and retains accuracy down to the order of δt^3 [192]. Note that the terms in the exponential operators are held constant over the time-step.

The benefit of the plane wave basis comes in the calculation of the matrix elements of the linear operator $\mathcal{R}$. The numerical calculation of derivative terms is often somewhat involved, but the application of Fourier transforms via the FFTW library simplifies this process drastically. Resolving $\mathcal{R}$ into the plane wave basis we obtain the linear Fourier space matrix operator R which has matrix elements

$$\begin{aligned}
R_{jk} &= \frac{1}{L}\int_{-L/2}^{L/2} e^{2\pi i jx/L}\mathcal{R}(x)e^{-2\pi ikx/L}dx \\
&= \frac{1}{L}\int_{-L/2}^{L/2} e^{2\pi i jx/L}\left[-\frac{1}{2}\frac{\partial^2}{\partial x^2} + q\delta(x - c_0)\right]e^{-2\pi ikx/L}dx \\
&= \frac{1}{2L}\left(\frac{2\pi k}{L}\right)^2\int_{-L/2}^{L/2} e^{2\pi i(j-k)x/L}dx + \frac{q}{L}e^{2\pi i(j-k)x_0/L} \\
&= \frac{\delta_{jk}}{2}\left(\frac{2\pi k}{L}\right)^2 + \frac{q}{L}e^{2\pi i(j-k)x_0/L}
\end{aligned} \tag{B.18}$$

These matrix elements are far simpler to calculate than the alternative derivative

calculations in the spatial basis, and can be utilised between forward and backward Fourier transforms, giving

$$\mathcal{R} = A^{-1}RA \tag{B.19}$$

Finally, the exponentiation of our operators is achieved via diagonalisation. $\mathcal{N}$ is already diagonal, but $\mathcal{R}$ is not due to the presence of the δ-function barrier. However, by re-writing R as $L = M^{-1}DM$, where D is diagonal, we can write

$$e^{-i\mathcal{R}\delta t} = A^{-1}M^{-1}e^{-iD\delta t}MA \tag{B.20}$$

where the functional operation on the diagonal matrix is defined as

$$f[D]_{jj} = f[D_{jj}] \tag{B.21}$$

and all off-diagonal elements are zero. We also point out that in the code the multiplications by A and A^{-1} are replaced by forward and backward executions of the FFTW routine.

The diagonalisation of R can be somewhat computationally intensive, and generally requires the use of advanced linear algebra packages. For the Hermitian matrix L this was accomplished by the "ZHEEV" subroutine found in the LAPACK library. Happily, this diagonalisation must only be carried out once (and the subsequent exponential operator determined) before being used at every time-step in the same form.

References

[1] F. Dalfovo, S. Giorgini, L. P. Pitaevskii, and S. Stringari, *Theory of Bose-Einstein condensation in trapped gases*, Rev. Mod. Phys. **71**, 463 (1999).

[2] A. Einstein, *Quantentheorie des einatomigen idealen Gases*, Sitzungsberichte der Preussichen Akademie der Wissenschaften Physikalisch-mathematische Klasse, p. 261 (1924).

[3] A. Einstein, *Quantentheorie des einatomigen idealen Gases. Zweite Abhandlung.*, Sitzungsberichte der Preussichen Akademie der Wissenschaften Physikalisch-mathematische Klasse, p. 3 (1925).

[4] D. Schumayer and B. Apagyi, *Relation between optical and atomic solitons*, Phys. Rev. A **65**, 053614 (2002).

[5] N. P. Proukakis, N. G. Parker, D. J. Frantzeskakis, and C. S. Adams, *Analogies between dark solitons in atomic bose–einstein condensates and optical systems*, J. Opt. B: Quantum and Semiclass. Opt. **6**, S380 (2004).

[6] K. B. Davis, M. O. Mewes, M. R. Andrews, N. J. van Druten, D. S. Durfee, D. M. Kurn, and W. Ketterle, *Bose-Einstein Condensation in a Gas of Sodium Atoms*, Phys. Rev. Lett. **75**, 3969 (1995).

[7] M. H. Anderson, J. R. Ensher, M. R. Matthews, C. E. Wieman, and E. A. Cornell, *Observation of Bose-Einstein Condensation in a Dilute Atomic Vapor*, Science **269**, 198 (1995).

[8] L. Khaykovich, F. Schreck, G. Ferrari, T. Bourdel, J. Cubizolles, L. D. Carr, Y. Castin, and C. Salomon, *Formation of a Matter-Wave Bright Soliton*, Science **296**, 1290 (2002).

[9] K. E. Strecker, G. B. Partridge, A. G. Truscott, and R. G. Hulet, *Formation and propagation of matter-wave soliton trains*, Nature **417**, 150 (2002).

[10] S. L. Cornish, S. T. Thompson, and C. E. Wieman, *Formation of Bright Matter-Wave Solitons during the Collapse of Attractive Bose-Einstein Condensates*, Phys. Rev. Lett. **96**, 170401 (2006).

[11] P. Medley, M. A. Minar, N. C. Cizek, D. Berryrieser, and M. A. Kasevich, *Evaporative production of bright atomic solitons*, Phys. Rev. Lett. **112**, 060401 (2014).

[12] S. A. Morgan, R. J. Ballagh, and K. Burnett, *Solitary-wave solutions to nonlinear Schrödinger equations* , Phys. Rev. A **55**, 4338 (1997).

[13] N. G. Parker, A. M. Martin, C. S. Adams, and S. L. Cornish, *Bright solitary waves of trapped atomic Bose-Einstein condensates*, Physica D **238**, 1456 (2009).

[14] T. P. Billam, S. L. Cornish, and S. A. Gardiner, *Realizing bright-matter-wave-soliton collisions with controlled relative phase*, Phys. Rev. A **83**, 041602(R) (2011).

[15] A. D. Martin, C. S. Adams, and S. A. Gardiner, *Bright Matter-Wave Soliton Collisions in a Harmonic Trap: Regular and Chaotic Dynamics*, Phys. Rev. Lett. **98**, 020402 (2007).

[16] A. D. Martin, C. S. Adams, and S. A. Gardiner, *Bright solitary-matter-wave collisions in a harmonic trap: Regimes of solitonlike behavior*, Phys. Rev. A **77**, 013620

(2008).

[17] D. Poletti, T. J. Alexander, E. A. Ostrovskaya, B. Li, and Y. S. Kivshar, *Dynamics of Matter-Wave Solitons in a Ratchet Potential*, Phys. Rev. Lett. **101**, 150403 (2008).

[18] V. Zakharov and A. Shabat, *Exact theory of two-dimensional self-focusing and one-dimensional self-modulation of waves in nonlinear media*, Zh. Eksp. Teor. Fiz. **61**, 118 (1971).

[19] J. Satsuma and N. Yajima, *Initial Value Problems of One-Dimensional Self-Modulation of Nonlinear Waves in Dispersive Media*, Prog. Theor. Phys. Suppl. **55**, 284 (1974).

[20] J. P. Gordon, *Interaction forces among solitons in optical fibers*, Opt. Lett. **8**, 596 (1983).

[21] H. A. Haus and W. S. Wong, *Solitons in optical communications*, Rev. Mod. Phys. **68**, 423 (1996).

[22] L. Helczynski, B. Hall, D. Anderson, M. Lisak, A. Berntson, and M. Desaix, *Cross phase modulation induced pulse splitting – the optical axe*, Physica Scripta **2000**, 81 (2000).

[23] D. N. Christodoulides and R. I. Joseph, *Discrete self-focusing in nonlinear arrays of coupled waveguides*, Opt. Lett. **13**, 794 (1988).

[24] O. Cohen, R. Uzdin, T. Carmon, J. W. Fleischer, M. Segev, and S. Odoulov, *Collisions between optical spatial solitons propagating in opposite directions*, Phys. Rev. Lett. **89**, 133901 (2002).

[25] T. P. Billam, S. A. Wrathmall, and S. A. Gardiner, *Variational determination of approximate bright matter-wave soliton solutions in anisotropic traps*, Phys. Rev. A **85**, 013627 (2012).

[26] S. L. Cornish, N. G. Parker, A. M. Martin, T. E. Judd, R. G. Scott, T. M. Fromhold, and C. S. Adams, *Quantum reflection of bright matter-wave solitons*, Physica D **238**, 1299 (2009).

[27] C. Weiss and Y. Castin, *Creation and Detection of a Mesoscopic Gas in a Nonlocal Quantum Superposition*, Phys. Rev. Lett. **102**, 010403 (2009).

[28] A. I. Streltsov, O. E. Alon, and L. S. Cederbaum, *Scattering of an attractive Bose-Einstein condensate from a barrier: Formation of quantum superposition states*, Phys. Rev. A **80**, 043616 (2009).

[29] U. Al Khawaja and H. T. C. Stoof, *Formation of matter-wave soliton molecules*, New J. Phys. **13**, 085003 (2011).

[30] A. D. Martin and J. Ruostekoski, *Quantum dynamics of atomic bright solitons under splitting and recollision, and implications for interferometry*, New Journal of Physics **14**, 043040 (2012).

[31] A. D. Cronin, J. Schmiedmayer, and D. E. Pritchard, *Optics and interferometry with atoms and molecules*, Rev. Mod. Phys. **81**, 1051 (2009).

[32] T. L. Gustavson, P. Bouyer, and M. A. Kasevich, *Precision Rotation Measurements with an Atom Interferometer Gyroscope*, Phys. Rev. Lett. **78**, 2046 (1997).

[33] A. Peters, K. Y. Chung, and S. Chu, *Measurement of gravitational acceleration by dropping atoms*, Nature **400**, 849 (1999).

[34] A. L. Marchant, T. P. Billam, T. P. Wiles, M. M. H. Yu, S. A. Gardiner, and S. L. Cornish, *Controlled formation and reflection of a bright solitary matter-wave*, Nat. Commun. **4**, 1865 (2013).

[35] G. D. McDonald, C. C. N. Kuhn, K. S. Hardman, S. Bennetts, P. J. Everitt, P. A. Altin, J. E. Debs, J. D. Close, and P. R. Nicholas, *A bright solitonic matter-wave interferometer* (2014), arXiv:/1403.3485.

[36] Y. S. Kivshar and B. A. Malomed, *Dynamics of solitons in nearly integrable systems*, Rev. Mod. Phys. **61**, 763 (1989).

[37] T. Ernst and J. Brand, *Resonant trapping in the transport of a matter-wave soliton through a quantum well*, Phys. Rev. A **81**, 033614 (2010).

[38] C. Lee and J. Brand, *Enhanced quantum reflection of matter-wave solitons*, Europhys. Lett. **73**, 321 (2006).

[39] X. D. Cao and B. A. Malomed, *Soliton-defect collisions in the nonlinear Schrödinger equation*, Phys. Lett. A **206**, 177 (1995).

[40] J. Holmer, J. Marzuola, and M. Zworski, *Fast Soliton Scattering by Delta Impurities*, Comm. Math. Phys. **274**, 187 (2007).

[41] J. Holmer, J. Marzuola, and M. Zworski, *Soliton Splitting by External Delta Potentials*, J. Nonlin. Sci. **17**, 349 (2007).

[42] W. Królikowski and Y. S. Kivshar, *Soliton-based optical switching in waveguide arrays*, J. Opt. Soc. Am. B **13**, 876 (1996).

[43] A. Fratalocchi and G. Assanto, *Governing soliton splitting in one-dimensional lattices*, Phys. Rev. E **73**, 046603 (2006).

[44] V. V. Konotop, D. Cai, M. Salerno, A. R. Bishop, and N. Grønbech-Jensen, *Interaction of a soliton with point impurities in an inhomogeneous, discrete nonlinear schrödinger system*, Phys. Rev. E **53**, 6476 (1996).

[45] J. Cuevas, P. G. Kevrekidis, B. A. Malomed, P. Dyke, and R. G. Hulet, *Interactions of solitons with a gaussian barrier: splitting and recombination in quasi-one-dimensional and three-dimensional settings*, New J. Phys. **15**, 063006 (2013).

[46] R. G. Hulet, *NLQUGAS: Nonlinear phenomena in degenerate quantum gases : Ourense (Spain), 12-16 April 2010 : conference abstracts* (José Ramón Salgueiro, 2010).

[47] P. B. Blakie, A. S. Bradley, M. J. Davis, R. J. Ballagh, and C. W. Gardiner, *Dynamics and statistical mechanics of ultra-cold Bose gases using c-field techniques*, Adv. Phys. **57**, 363 (2008).

[48] J. L. Helm, T. P. Billam, and S. A. Gardiner, *Bright matter-wave soliton collisions at narrow barriers*, Phys. Rev. A **85**, 053621 (2012).

[49] J. L. Helm, S. J. Rooney, C. Weiss, and S. A. Gardiner, *Splitting bright matter-wave solitons on narrow potential barriers: Quantum to classical transition and applications to interferometry*, Phys. Rev. A **89**, 033610 (2014).

[50] J. L. Helm, S. L. Cornis, and S. A. Gardiner, *Sagnac paper*, Phys. Rev.

[51] L. Kelvin, *On an absolute thermometric scale*, Mathematical and Physical Papers **1**, 100 (1882).

[52] P. Kapitza, *Viscosity of Liquid Helium below the λ-Point*, Nature **141**, 74 (1938).

[53] J. F. Allen and A. D. Misener, *Flow of Liquid Helium II*, Nature **141**, 75 (1938).

[54] Bose, *Plancks Gesetz und Lichtquantenhypothese*, Zeitschrift für Physik **26**, 178 (1924).

[55] W. Pauli, *The Connection Between Spin and Statistics*, Phys. Rev. **58**, 716 (1940).

[56] F. London, *The λ-Phenomenon of Liquid Helium and the Bose-Einstein Degeneracy*, Nature **141**, 643 (1938).

[57] L. Tisza, *Transport Phenomena in Helium II*, Nature **141**, 913 (1938).

[58] C. J. Foot, *Laser trapping and cooling of atoms*, Contemp. Phys. **32**, 369 (1991).

[59] T. P. Billam, *Bright solitary waves and non-equilibrium dynamics in atomic Bose-Einstein condensates*, Ph.D. thesis, University of Durham (2012).

[60] C. C. Bradley, C. A. Sackett, J. J. Tollett, and R. G. Hulet, *Evidence of Bose-Einstein Condensation in an Atomic Gas with Attractive Interactions*, Phys. Rev. Lett. **75**, 1687 (1995).

[61] G. Roati, M. Zaccanti, C. D'Errico, J. Catani, M. Modugno, A. Simoni, M. Inguscio, and G. Modugno, ^{39}K *Bose-Einstein Condensate with Tunable Interactions*, Phys. Rev. Lett. **99**, 010403 (2007).

[62] G. Modugno, G. Ferrari, G. Roati, R. J. Brecha, A. Simoni, and M. Inguscio, *Bose-Einstein Condensation of Potassium Atoms by Sympathetic Cooling*, Science **294**, 1320 (2001).

[63] S. L. Cornish, N. R. Claussen, J. L. Roberts, E. A. Cornell, and C. E. Wieman, *Stable* 85*Rb Bose-Einstein Condensates with Widely Tunable Interactions*, Phys. Rev. Lett. **85**, 1795 (2000).

[64] T. Weber, J. Herbig, M. Mark, H.-C. Nägerl, and R. Grimm, *Bose-Einstein Condensation of Cesium*, Science **299**, 232 (2003).

[65] D. G. Fried, T. C. Killian, L. Willmann, D. Landhuis, S. C. Moss, D. Kleppner, and T. J. Greytak, *Bose-Einstein Condensation of Atomic Hydrogen*, Phys. Rev. Lett. **81**, 3811 (1998).

[66] S. Kraft, F. Vogt, O. Appel, F. Riehle, and U. Sterr, *Bose-Einstein Condensation of Alkaline Earth Atoms:* ^{40}Ca, Phys. Rev. Lett. **103**, 130401 (2009).

[67] S. Stellmer, M. K. Tey, B. Huang, R. Grimm, and F. Schreck, *Bose-Einstein Condensation of Strontium*, Phys. Rev. Lett. **103**, 200401 (2009).

[68] Y. N. M. de Escobar, P. G. Mickelson, M. Yan, B. J. DeSalvo, S. B. Nagel, and T. C. Killian, *Bose-Einstein Condensation of* ^{84}Sr, Phys. Rev. Lett. **103**, 200402 (2009).

[69] S. Stellmer, M. K. Tey, R. Grimm, and F. Schreck, *Bose-Einstein condensation of* ^{86}Sr, Phys. Rev. A **82**, 041602 (2010).

[70] P. G. Mickelson, Y. N. Martinez de Escobar, M. Yan, B. J. DeSalvo, and T. C. Killian, *Bose-Einstein condensation of* ^{88}Sr *through sympathetic cooling with* ^{87}Sr, Phys. Rev. A **81**, 051601 (2010).

[71] G.-B. Jo, J.-H. Choi, C. A. Christensen, Y.-R. Lee, T. A. Pasquini, W. Ketterle, and D. E. Pritchard, *Matter-wave interferometry with phase fluctuating bose-einstein condensates*, Phys. Rev. Lett. **99**, 240406 (2007).

[72] T. Fukuhara, S. Sugawa, and Y. Takahashi, *Bose-Einstein condensation of an ytterbium isotope*, Phys. Rev. A **76**, 051604 (2007).

[73] T. Fukuhara, S. Sugawa, Y. Takasu, and Y. Takahashi, *All-optical formation of quantum degenerate mixtures*, Phys. Rev. A **79**, 021601 (2009).

[74] S. Sugawa, R. Yamazaki, S. Taie, and Y. Takahashi, *Bose-Einstein condensate in gases of rare atomic species*, Phys. Rev. A **84**, 011610 (2011).

[75] F. Pereira Dos Santos, J. Léonard, J. Wang, C. J. Barrelet, F. Perales, E. Rasel, C. S. Unnikrishnan, M. Leduc, and C. Cohen-Tannoudji, *Bose-Einstein Condensation of Metastable Helium*, Phys. Rev. Lett. **86**, 3459 (2001).

[76] A. Robert, O. Sirjean, A. Browaeys, J. Poupard, S. Nowak, D. Boiron, C. I. Westbrook, and A. Aspect, *A Bose-Einstein Condensate of Metastable Atoms*, Science

292, 461 (2001).

[77] M. Lu, N. Q. Burdick, S. H. Youn, and B. L. Lev, *Strongly Dipolar Bose-Einstein Condensate of Dysprosium*, Phys. Rev. Lett. **107**, 190401 (2011).

[78] A. Griesmaier, J. Werner, S. Hensler, J. Stuhler, and T. Pfau, *Bose-Einstein Condensation of Chromium*, Phys. Rev. Lett. **94**, 160401 (2005).

[79] E. Timmermans, P. Tommasini, M. Hussein, and A. Kerman, *Feshbach resonances in atomic Bose-Einstein condensates*, Phys. Rep. **315**, 199 (1999).

[80] C. Chin, R. Grimm, P. Julienne, and E. Tiesinga, *Feshbach resonances in ultracold gases*, Rev. Mod. Phys. **82**, 1225 (2010).

[81] C. Pethick and H. Smith, *Bose-Einstein condensation in dilute gases* (Cambridge University Press, Cambridge, 2002).

[82] N. P. Proukakis and B. Jackson, *Finite-temperature models of Bose-Einstein condensation*, J. Phys. B **41**, 203002 (2008).

[83] D. M. Ceperley, *Path integrals in the theory of condensed helium*, Rev. Mod. Phys. **67**, 279 (1995).

[84] O. Penrose and L. Onsager, *Bose-Einstein Condensation and Liquid Helium*, Phys. Rev. **104**, 576 (1956).

[85] D. Griffiths, *Introduction to Quantum Mechanics* (Prentice Hall, New York, 2005).

[86] L. Pitaevskii and S. Stringari, *Bose-Einstein Condensation* (Clarendon Press, Oxford, 2003).

[87] R. P. Feynman, *Statistical Mechanics: A set of lectures* (Addison-Wesley, New York, 1972).

[88] J. F. Annett, *Superconductivity, Superfluids, and Condensates* (Oxford University Press, Oxford, 2004).

[89] J. A. Dunningham and K. Burnett, *Sub-shot-noise-limited measurements with Bose-Einstein condensates*, Phys. Rev. A **70**, 033601 (2004).

[90] J. J. Cooper, D. W. Hallwood, and J. A. Dunningham, *Entanglement-enhanced atomic gyroscope*, Phys. Rev. A **81**, 043624 (2010).

[91] M. R. Andrews, C. G. Townsend, H.-J. Miesner, D. S. Durfee, D. M. Kurn, and W. Ketterle, *Observation of Interference Between Two Bose Condensates*, Science **275**, 637 (1997).

[92] B. Gertjerenken, T. P. Billam, L. Khaykovich, and C. Weiss, *Scattering bright solitons: Quantum versus mean-field behavior*, Phys. Rev. A **86**, 033608 (2012).

[93] Y. Shin, M. Saba, T. A. Pasquini, W. Ketterle, D. E. Pritchard, and A. E. Leanhardt, *Atom Interferometry with Bose-Einstein Condensates in a Double-Well Potential*, Phys. Rev. Lett. **92**, 050405 (2004).

[94] M. Fattori, C. D'Errico, G. Roati, M. Zaccanti, M. Jona-Lasinio, M. Modugno, M. Inguscio, and G. Modugno, *Atom Interferometry with a Weakly Interacting Bose-Einstein Condensate*, Phys. Rev. Lett. **100**, 080405 (2008).

[95] Y.-J. Wang, D. Z. Anderson, V. M. Bright, E. A. Cornell, Q. Diot, T. Kishimoto, M. Prentiss, R. A. Saravanan, S. R. Segal, and S. Wu, *Atom Michelson Interferometer on a Chip Using a Bose-Einstein Condensate*, Phys. Rev. Lett. **94**, 090405 (2005).

[96] A. Fetter and J. Walecka, *Quantum theory of many-particle systems* (Dover, New York, 1971).

[97] R. P. Smith, R. L. D. Campbell, N. Tammuz, and Z. Hadzibabic, *Effects of Interactions on the Critical Temperature of a Trapped Bose Gas*, Phys. Rev. Lett. **106**,

250403 (2011).

[98] M. J. Davis and P. B. Blakie, *Critical Temperature of a Trapped Bose Gas: Comparison of Theory and Experiment*, Phys. Rev. Lett. **96**, 060404 (2006).

[99] F. Gerbier, J. H. Thywissen, S. Richard, M. Hugbart, P. Bouyer, and A. Aspect, *Critical temperature of a trapped, weakly interacting bose gas*, Phys. Rev. Lett. **92**, 030405 (2004).

[100] N. Tammuz, R. P. Smith, R. L. D. Campbell, S. Beattie, S. Moulder, J. Dalibard, and Z. Hadzibabic, *Can a Bose Gas Be Saturated?*, Phys. Rev. Lett. **106**, 230401 (2011).

[101] W. Mullin, *Bose-Einstein condensation in a harmonic potential*, J. Low Temp. Phys. **106**, 615 (1997).

[102] S. Giorgini, L. P. Pitaevskii, and S. Stringari, *Condensate fraction and critical temperature of a trapped interacting Bose gas*, Phys. Rev. A **54**, R4633 (1996).

[103] R. P. Smith, N. Tammuz, R. L. D. Campbell, M. Holzmann, and Z. Hadzibabic, *Condensed Fraction of an Atomic Bose Gas Induced by Critical Correlations*, Phys. Rev. Lett. **107**, 190403 (2011).

[104] A. L. Fetter, *Nonuniform states of an imperfect bose gas*, Annals of Physics **70**, 67 – 101 (1972), ISSN 0003-4916.

[105] A. J. Leggett, *Bose-Einstein condensation in the alkali gases: Some fundamental concepts*, Rev. Mod. Phys. **73**, 307 (2001).

[106] V. Yukalov, *Bose-Einstein condensation and gauge symmetry breaking*, Las. Phys. Lett. **4**, 632 (2007).

[107] A. Griffin, T. Nikuni, and E. Zaremba, *Bose-Condensed Gases at Finite Temperatures* (Cambridge University Press, Cambridge, 2009).

[108] K. Huang, *Statistical Mechanics*, 2nd ed. (John Wiley & Sons, 1987).

[109] E. Gross, *Structure of a quantized vortex in boson systems*, Il Nuovo Cimento (1955-1965) **20**, 454 (1961).

[110] L. P. Pitaevskii, *Vortex lines in an imperfect bose gas*, Soviet Physics JETP-USSR **13** (1961).

[111] R. J. Dodd, M. Edwards, C. W. Clark, and K. Burnett, *Collective excitations of Bose-Einstein-condensed gases at finite temperatures*, Phys. Rev. A **57**, R32 (1998).

[112] D. A. W. Hutchinson, R. J. Dodd, and K. Burnett, *Gapless Finite- T Theory of Collective Modes of a Trapped Gas*, Phys. Rev. Lett. **81**, 2198 (1998).

[113] M. Edwards, P. A. Ruprecht, K. Burnett, R. J. Dodd, and C. W. Clark, *Collective excitations of atomic bose-einstein condensates*, Phys. Rev. Lett. **77**, 1671 (1996).

[114] J. P. Blaizot and G. Ripka, *Quantum Theory of Finite Systems* (The MIT Press, Cambridge, Massachusetts, 1986).

[115] D. A. W. Hutchinson, E. Zaremba, and A. Griffin, *Finite Temperature Excitations of a Trapped Bose Gas*, Phys. Rev. Lett. **78**, 1842 (1997).

[116] N. P. Proukakis, K. Burnett, and H. T. C. Stoof, *Microscopic treatment of binary interactions in the nonequilibrium dynamics of partially bose-condensed trapped gases*, Phys. Rev. A **57**, 1230 (1998).

[117] S. A. Morgan, *A gapless theory of Bose-Einstein condensation in dilute gases at finite temperature*, J. Phys. B **33**, 3847 (2000).

[118] S. A. Morgan, *A Gapless Theory of Bose-Einstein Condensation in Dilute Gases at Finite Temperature*, Ph.D. thesis, University of Oxford (1999).

[119] N. P. Proukakis, *Self-consistent quantum kinetics of condensate and non-condensate*

via a coupled equation of motion formalism, J. Phys. B **34**, 4737 (2001).

[120] *Generalized mean fields for trapped atomic bose-einstein condensates*, J. Res. Natl Inst. Stand. Technol **101**, 457.

[121] E. Zaremba, T. Nikuni, and A. Griffin, *Dynamics of trapped bose gases at finite temperatures*, J. Low Temp. Phys. **116**, 277 (1999).

[122] S. Giorgini, *Damping in dilute bose gases: A mean-field approach*, Phys. Rev. A **57**, 2949 (1998).

[123] S. Giorgini, *Collisionless dynamics of dilute bose gases: Role of quantum and thermal fluctuations*, Phys. Rev. A **61**, 063615 (2000).

[124] M. Rusch and K. Burnett, *Mean-field theory for excitations of trapped bose condensates at finite temperatures*, Phys. Rev. A **59**, 3851 (1999).

[125] N. N. Bogoliubov, J. Phys. USSR **11**, 23 (1947).

[126] C. W. Gardiner, *Particle-number-conserving Bogoliubov method which demonstrates the validity of the time-dependent Gross-Pitaevskii equation for a highly condensed Bose gas*, Phys. Rev. A **56**, 1414 (1997).

[127] Y. Castin and R. Dum, *Low-temperature Bose-Einstein condensates in time-dependent traps: Beyond the $U(1)$ symmetry-breaking approach*, Phys. Rev. A **57**, 3008 (1998).

[128] Y. Castin and R. Dum, *Instability and Depletion of an Excited Bose-Einstein Condensate in a Trap*, Phys. Rev. Lett. **79**, 3553 (1997).

[129] S. A. Gardiner and S. A. Morgan, *Number-conserving approach to a minimal self-consistent treatment of condensate and noncondensate dynamics in a degenerate Bose gas*, Phys. Rev. A **75**, 043621 (2007).

[130] S. A. Morgan, M. Rusch, D. A. W. Hutchinson, and K. Burnett, *Quantitative Test of Thermal Field Theory for Bose-Einstein Condensates*, Phys. Rev. Lett. **91**, 250403 (2003).

[131] S. A. Morgan, *Quantitative test of thermal field theory for Bose-Einstein condensates. II*, Phys. Rev. A **72**, 043609 (2005).

[132] S. A. Morgan, *Response of Bose-Einstein condensates to external perturbations at finite temperature*, Phys. Rev. A **69**, 023609 (2004).

[133] D. A. W. Hutchinson, K. Burnett, R. J. Dodd, S. A. Morgan, M. Rusch, E. Zaremba, N. P. Proukakis, M. Edwards, and C. W. Clark, *Gapless mean-field theory of Bose-Einstein condensates*, J. Phys. B **33**, 3825 (2000).

[134] E. A. Donley, N. R. Claussen, S. L. Cornish, J. L. Roberts, E. A. Cornell, and C. E. Wieman, *Dynamics of collapsing and exploding Bose–Einstein condensates*, Nature **412**, 295 (2001).

[135] Y. Kagan, G. V. Shlyapnikov, and J. T. M. Walraven, *Bose-Einstein Condensation in Trapped Atomic Gases*, Phys. Rev. Lett. **76**, 2670 (1996).

[136] C. C. Bradley, C. A. Sackett, and R. G. Hulet, *Bose-Einstein Condensation of Lithium: Observation of Limited Condensate Number*, Phys. Rev. Lett. **78**, 985 (1997).

[137] J. L. Roberts, N. R. Claussen, S. L. Cornish, and C. E. Wieman, *Magnetic Field Dependence of Ultracold Inelastic Collisions near a Feshbach Resonance*, Phys. Rev. Lett. **85**, 728 (2000).

[138] J. M. Gerton, D. Strekalov, I. Prodan, and R. G. Hulet, *Direct observation of growth and collapse of a Bose-Einstein condensate with attractive interactions*, Nature **408**,

692 (2000).

[139] P. A. Ruprecht, M. J. Holland, K. Burnett, and M. Edwards, *Time-dependent solution of the nonlinear Schrödinger equation for Bose-condensed trapped neutral atoms*, Phys. Rev. A **51**, 4704 (1995).

[140] R. J. Dodd, M. Edwards, C. J. Williams, C. W. Clark, M. J. Holland, P. A. Ruprecht, and K. Burnett, *Role of attractive interactions on Bose-Einstein condensation*, Phys. Rev. A **54**, 661 (1996).

[141] M. Houbiers and H. T. C. Stoof, *Stability of Bose condensed atomic* ^{7}Li, Phys. Rev. A **54**, 5055 (1996).

[142] C. Huepe, S. Métens, G. Dewel, P. Borckmans, and M. E. Brachet, *Decay Rates in Attractive Bose-Einstein Condensates*, Phys. Rev. Lett. **82**, 1616 (1999).

[143] N. Akhmediev, M. P. Das, and A. V. Vagov, *Bose-Einstein condensation of atoms with attractive interaction*, Int. J. Mod. Phys. B **13**, 625 (1999).

[144] L. Bergé, T. J. Alexander, and Y. S. Kivshar, *Stability criterion for attractive Bose-Einstein condensates*, Phys. Rev. A **62**, 023607 (2000).

[145] A. Gammal, T. Frederico, and L. Tomio, *Critical number of atoms for attractive Bose-Einstein condensates with cylindrically symmetrical traps*, Phys. Rev. A **64**, 055602 (2001).

[146] L. Salasnich, A. Parola, and L. Reatto, *Condensate bright solitons under transverse confinement*, Phys. Rev. A **66**, 043603 (2002).

[147] L. Salasnich, A. Parola, and L. Reatto, *Effective wave equations for the dynamics of cigar-shaped and disk-shaped Bose condensates*, Phys. Rev. A **65**, 043614 (2002).

[148] A. Gammal, L. Tomio, and T. Frederico, *Critical numbers of attractive Bose-Einstein condensed atoms in asymmetric traps*, Phys. Rev. A **66**, 043619 (2002).

[149] C. M. Savage, N. P. Robins, and J. J. Hope, *Bose-Einstein condensate collapse: A comparison between theory and experiment*, Phys. Rev. A **67**, 014304 (2003).

[150] V. I. Yukalov and E. P. Yukalova, *Optimal trap shape for a Bose gas with attractive interactions*, Phys. Rev. A **72**, 063611 (2005).

[151] N. G. Parker, S. L. Cornish, C. S. Adams, and A. M. Martin, *Bright solitary waves and trapped solutions in Bose-Einstein condensates with attractive interactions*, J. Phys. B **40**, 3127 (2007).

[152] V. M. Pérez-García, H. Michinel, J. I. Cirac, M. Lewenstein, and P. Zoller, *Dynamics of Bose-Einstein condensates: Variational solutions of the Gross-Pitaevskii equations*, Phys. Rev. A **56**, 1424 (1997).

[153] D. I. H. Holdaway, C. Weiss, and S. A. Gardiner, *Quantum theory of bright matter-wave solitons in harmonic confinement*, Phys. Rev. A **85**, 053618 (2012).

[154] L. Salasnich, A. Parola, and L. Reatto, *Modulational Instability and Complex Dynamics of Confined Matter-Wave Solitons*, Phys. Rev. Lett. **91**, 080405 (2003).

[155] L. Salasnich, B. A. Malomed, and F. Toigo, *Matter-wave vortices in cigar-shaped and toroidal waveguides*, Phys. Rev. A **76**, 063614 (2007).

[156] V. M. Pérez-García, H. Michinel, and H. Herrero, *Bose-Einstein solitons in highly asymmetric traps*, Phys. Rev. A **57**, 3837 (1998).

[157] V. M. Pérez-García, H. Michinel, J. I. Cirac, M. Lewenstein, and P. Zoller, *Low Energy Excitations of a Bose-Einstein Condensate: A Time-Dependent Variational Analysis*, Phys. Rev. Lett. **77**, 5320 (1996).

[158] U. Al Khawaja, H. T. C. Stoof, R. G. Hulet, K. E. Strecker, and G. B. Partridge,

Bright Soliton Trains of Trapped Bose-Einstein Condensates, Phys. Rev. Lett. **89**, 200404 (2002).

[159] P. Drazin and R. Johnson, *Solitons: an introduction*, Cambridge texts in applied mathematics (Cambridge University Press, 1989).

[160] M. J. Ablowitz and H. Segur, *Solitons and the inverse scattering transform* (SIAM, Philadelphia, 1981).

[161] L. D. Fadeev and L. A. Takhtajan, *Hamiltonian Methods in the Theory of Solitons* (Springer-Verlag, Berlin, 1987).

[162] S. Farlow, *Partial Differential Equations for Scientists and Engineers* (Dover Publications, 1993).

[163] P. D. Lax, *The formation and decay of shock waves*, The American Mathematical Monthly **79**, 227 (1972).

[164] R. LeVeque, *Numerical Methods for Conservation Laws*, Lectures in Mathematics ETH Zürich, Department of Mathematics Research Institute of Mathematics (Springer, 1992).

[165] P. D. Lax, *Integrals of nonlinear equations of evolution and solitary waves*, Communications on Pure and Applied Mathematics **21**, 467 (1968).

[166] E. Brigham, *The fast Fourier transform*, Prentice-Hall signal processing series (Prentice-Hall, 1974).

[167] V. Zakharov and A. Shabat, *Exact theory of two-dimensional self-focusing and one-dimensional self-modulation of waves in nonlinear media*, Sov. Phys. JETP **34**, 62 (1972).

[168] C. S. Gardner, J. M. Greene, M. D. Kruskal, and R. M. Miura, *Method for solving the Korteweg-deVries equation*, Phys. Rev. Lett. **19**, 1095–1097 (1967).

[169] J. Polo and V. Ahufinger, *Soliton-based matter-wave interferometer*, Phys. Rev. A **88**, 053628 (2013).

[170] C.-H. Wang, T.-M. Hong, R.-K. Lee, and D.-W. Wang, *Particle-wave duality in quantum tunneling of a bright soliton*, Opt. Express **20**, 22675 (2012).

[171] S. Damgaard Hansen, N. Nygaard, and K. Mølmer, *Scattering of matter wave solitons on localized potentials*, ArXiv e-prints(2012), arXiv:1210.1681.

[172] M. Minmar, *Macroscopic Wave Dynamics of Bright Solitons*, Ph.D. thesis, Stanford University (2012).

[173] A. Ramanathan, K. C. Wright, S. R. Muniz, M. Zelan, W. T. Hill, C. J. Lobb, K. Helmerson, W. D. Phillips, and G. K. Campbell, *Superflow in a toroidal bose-einstein condensate: An atom circuit with a tunable weak link*, Phys. Rev. Lett. **106**, 130401 (2011).

[174] B. Gertjerenken, T. P. Billam, C. L. Blackley, C. R. Le Sueur, L. Khaykovich, S. L. Cornish, and C. Weiss, *Generating mesoscopic bell states via collisions of distinguishable quantum bright solitons*, Phys. Rev. Lett. **111**, 100406 (2013).

[175] E. H. Lieb and W. Liniger, *Exact Analysis of an Interacting Bose Gas. I. The General Solution and the Ground State*, Phys. Rev. **130**, 1605 (1963).

[176] S. O. Rice, *Mathematical analysis of random noise*, AT&T Tech. J **24**, 46 (1945).

[177] B. J. Dąbrowska-Wüster, S. Wüster, and M. J. Davis, *Dynamical formation and interaction of bright solitary waves and solitons in the collapse of Bose-Einstein condensates with attractive interactions*, New J. Phys. **11**, 053017 (2009).

[178] D. D. Wackerly, W. M. III, and R. L. Scheaffer, *Mathematical Statistics with Appli-*

cations, sixth edition ed. (Duxbury Advanced Series, 2002).

[179] E. Hecht, *Optics (4th Edition)*, 4th ed. (Addison Wesley, 2001).

[180] A. Sacchetti, *Spectral splitting method for nonlinear Schrödinger equations with singular potential*, J. Comp. Phys. **227**, 1483 (2007).

[181] S. Gupta, K. W. Murch, K. L. Moore, T. P. Purdy, and D. M. Stamper-Kurn, *Bose-einstein condensation in a circular waveguide*, Phys. Rev. Lett. **95**, 143201 (2005).

[182] J. A. Sauer, M. D. Barrett, and M. S. Chapman, *Storage ring for neutral atoms*, Phys. Rev. Lett. **87**, 270401 (2001).

[183] G. M. Kavoulakis, *Bose-einstein condensates with attractive interactions on a ring*, Phys. Rev. A **67**, 011601 (2003).

[184] A. Parola, L. Salasnich, R. Rota, and L. Reatto, *Quantum phases of attractive matter waves in a toroidal trap*, Phys. Rev. A **72**, 063612 (2005).

[185] L. Salasnich, A. Parola, and L. Reatto, *Thermodynamics of solitonic matter waves in a toroidal trap*, Phys. Rev. A **74**, 031603 (2006).

[186] L. Salasnich, B. A. Malomed, and F. Toigo, *Matter-wave vortices in cigar-shaped and toroidal waveguides*, Phys. Rev. A **76**, 063614 (2007).

[187] F. Riehle, T. Kisters, A. Witte, J. Helmcke, and C. J. Bordé, *Optical ramsey spectroscopy in a rotating frame: Sagnac effect in a matter-wave interferometer*, Phys. Rev. Lett. **67** (1991), doi: \bibinfo{doi}{10.1103/PhysRevLett.67.177}.

[188] M. Abramowitz and I. A. Stegun, *Handbook of Mathematical Functions with Formulas, Graphs, and Mathematical Tables*, ninth dover printing, tenth gpo printing ed. (Dover, New York, 1964).

[189] L. D. Carr, C. W. Clark, and W. P. Reinhardt, *Stationary solutions of the one-dimensional nonlinear Schrödinger equation. II. Case of attractive nonlinearity*, Phys. Rev. A **62**, 063611 (2000).

[190] A. Sacchetti, *Spectral splitting method for nonlinear schrödinger equations with singular potential*, J. Comp. Phys **227**, 1483–1499 (2007), ISSN 0021-9991.

[191] M. Frigo and S. G. Johnson, *The Design and Implementation of FFTW3*, Proc. IEEE **93**, 216 (2005).

[192] J. Javanainen and J. Ruostekoski, *Symbolic calculation in development of algorithms: split-step methods for the gross–pitaevskii equation*, J. Phys. A **39**, L179 (2006).